



SAPIENZA
UNIVERSITÀ DI ROMA

Department of Physics ‘G. Marconi’
PhD in Accelerator Physics

THESIS FOR THE DEGREE OF DOCTOR OF PHILOSOPHY

New high intensity & brightness muon beams for experiments at the intensity frontier



Thesis advisor

Prof. Angela Papa

Thesis co-advisor

Prof. Aldo Sady Antognini

Candidate

Bastiano Vitali

1949877

Academic Year 2023-2024 (XXXVI cycle)

Contents

missing, started, review, correct, done	1
1 Introduction	1
1.1 Outline of this thesis	1
1.2 Particle physics at Paul Scherrer Institute	1
1.3 Bite-size theory	2
1.3.1 Standard Model at low energies	2
1.3.2 Beyond Standard Model at low-energy	4
1.3.3 Muon	5
1.3.4 Muon decay	6
1.3.5 Electric Dipole Moment	7
1.4 Experimental status	8
1.4.1 CLFV experiments	8
1.4.2 EDM experiments	14
1.5 The beams at PSI	19
1.5.1 High-Intensity Proton Accelerator facility	19
1.5.2 Meson production	22
1.5.3 Neutron production	25
1.5.4 High-Intensity Muon Beams	26
1.6 Proton Ionization Facility	29
Bibliography for the introduction	30
I muEDM	35
2 muEDM	36
2.1 Electric Dipole Moment	36
2.1.1 Symmetry violation	37
2.1.2 Current limits on EDM	37
2.1.3 The <i>frozen spin</i> technique	37
2.2 The muEDM experiment	38
2.3 The precursor	38
2.3.1 Superconducting injection channel	38
2.3.2 Entrance detector	39
2.3.3 Muon tracking	39
2.3.4 Kicker	39
2.3.5 Electrodes	40
2.3.6 Positron tracking	40
2.4 Systematics	40
2.5 Schedule	40
2.6 Conclusions	40

Bibliography on muEDM	40
3 muEDM entrance detector	43
3.1 Short intro to scintillators	43
3.1.1 Plastic scintillators	43
3.1.2 Scintillation process	44
3.1.3 Scintillating Fibers	45
3.2 GEANT4 simulations	45
3.2.1 GEANT4	45
3.2.2 Entrance system	46
3.2.3 Telescope and entrance detector	50
3.3 Beamtime 2021	50
3.3.1 Description of the multiple scattering	50
3.3.2 Data taking	51
3.3.3 Data analysis	51
3.3.4 Model evaluation and conclusions	54
3.4 Beamtime 2022: Telescope and entrance detector	54
3.4.1 Construction	54
3.4.2 Data taking	56
3.4.3 Data analysis	56
3.5 Beamtime 2023: Multi readout entrance	56
3.5.1 Data taking	56
3.5.2 Data analysis	56
Bibliography on muEDM entrance detector	56
4 muEDM positron tracker	58
4.1 Tracking e^+ in muEDM	58
4.1.1 The g-2 anomaly	58
4.1.2 The EDM	58
4.1.3 Design in the 2022 proposal	58
4.2 CHeT or CyFi	58
4.2.1 Resolutions of crossed fibers ribbons	59
4.2.2 Angle choices for the layers	60
4.2.3 GEANT4 simulation	62
4.2.4 From γs to waveforms	63
4.2.5 From hits to c-hits	64
4.3 Prototype/Beamtime	64
4.4 Conclusions	64
II muCool	65
5 muCool	66
5.1 The working principle	66
5.2 Simulations	66
5.2.1 Cooling	66
5.2.2 Extraction	66
5.2.3 Re-acceleration	66
5.3 Validation	66
5.4 Conclusion	66
6 muCool upgrade	67

6.1	New target	67
6.2	Cryogenic system	67
6.3	High Voltage system	67
6.4	Conclusion	67
III	MEG II	68
7	MEG II and the Cockcroft–Walton	69
7.1	MEG II	69
7.2	The liquid XEnon Calorimeter	70
7.2.1	Xe scintillation	71
7.2.2	Photon detection	71
7.2.3	Calibration	72
7.2.4	Reconstruction and performance	73
7.3	Spectrometer	74
7.3.1	COBRA	74
7.3.2	Cylindrical Drift CHamber (CDCH)	74
7.3.3	pixelated Timing Counter (pTC)	77
7.4	Trigger and DAQ	77
7.5	Beam and target	77
7.5.1	$\pi E5$	79
7.5.2	Simulations	79
7.5.3	MEG II target	82
7.6	Cockcroft–Walton	83
7.6.1	Description of the machine	83
7.6.2	Usage	86
7.6.3	CW issues and maintenance	87
7.7	Conclusions	90
Bibliography on MEG II	90	
8	Liquid Hydrogen target	94
8.1	Charge EXchange reaction	94
8.2	BGO	94
8.3	LH ₂ target working principle	95
8.3.1	Operation and control	97
8.4	2021	97
8.4.1	Data taking	97
8.4.2	Data analysis	98
8.5	2022	98
8.5.1	Upgrades	98
8.5.2	Data taking	98
8.5.3	Data analysis	98
8.6	2023	98
8.6.1	Upgrades	98
8.6.2	Data taking	99
8.6.3	Data analysis	99
8.7	Conclusions	99
Bibliography on LH₂	99	
9	Search for X17	101

9.1	ATOMKI and the X17 ‘anomaly’	101
9.2	X17 in MEG II	101
9.2.1	MC simulations	101
9.2.2	Magnetic field choice	101
9.2.3	Target	102
9.3	Data acquisition	102
9.3.1	Beam tuning	102
9.3.2	Asymmetry	104
9.3.3	Normalization	104
9.4	Data analysis	104
9.4.1	Pair reconstruction	104
9.4.2	Asymmetry	104
9.4.3	Feldman-Cousin	104
9.5	Results and conclusions	105
	Bibliography on X17	105
A	Fibers with G4TessellatedSolid	107
B	Kalman filter	110
B.1	The problem	110
B.2	The solution	110
B.3	Implementation	111
B.4	Example: a 2D linear fit	112
B.4.1	Adding multiple scattering	114
	Acknowledgement	116

Chapter 1

Introduction

Here we will provide an overview of the following chapters as well as define the theoretical and experimental background for this work. The first section will be dedicated to the outline of this thesis, to aid the readers. A somewhat shallow review of the particle physics searches at PSI will follow, with some in-depth dive into the subjects that are close to the core of this thesis. This will be complemented by the description of the different facilities at PSI, with a final section dedicated to the Proton Ionization Facility.

This whole chapter relies heavily on references [1] [2] and partially on [3].

1.1 Outline of this thesis

The structure of this Thesis might differ slightly from the norm. While most of my colleagues dedicated their work to a singular subject, like a particular detector or theory, my effort during the course of this Ph.D. has been spread on a quite large angle. At first glance, this work might seem the result of three separate projects, namely MEG, MuEDM, and muCool. In fact, the spirit in which this Thesis has been developed is orthogonal to the chapters themselves: the overall progress of muonic particle physics experiments. Given the nature of the different tasks I worked on, I included *a lot* of introductory material to guide the reader through the different sections.

- Introduction: theory, PSI facilities and key experiments
- muCool (?)
- muEDM: introduction, entrance detector, tracker
- MEG: introduction and CW, Liquid Hydrogen target, X17 search

1.2 Particle physics at Paul Scherrer Institute

Belonging to ETH domain and formed in 1988 as a national laboratory, the Paul Scherrer Institute (PSI) is the largest federal research institute in Switzerland. PSI hosts the world's most powerful proton accelerators, with an average power of 1.4 MW and a beam current of over 2 mA. On top of the proton facility, in the last 10 years, a neutron spallation target has been added for ultracold neutrons production. PSI is renowned for its extensive research across a wide range of scientific disciplines. With its world-class facilities and expertise, PSI plays a pivotal role in advancing our understanding of fundamental particles and their interactions, solidifying its position as a key player in the field of particle physics on a global scale. Everything discussed in this thesis is a

product of the fertile environment at this Institute and the active collaborations with universities and institutions, such as INFN, around the world.

1.3 Bite-size theory

The aim of this section is to define the framework in which (part) of particle physics research is moving. In particular, we will be focusing on the aspects which are relevant to the three experiments core of this thesis. The searches Beyond Standard Model (BSM) proceed in two main directions: *intensity frontier* is used to describe the test of contributions that are too small to be experimentally accessible observing large numbers of events; *precision frontier* is used when improving the accuracy of a specific parameter to test the agreement with the Standard Model (SM). Searches for charged lepton flavour violation (cLFV) or neutron permanent Electric Dipole Moment (EDM) are examples of the former type while precision Quantum ElectroDynamics (QED) tests with muonium are of the latter.

1.3.1 Standard Model at low energies

In the low energy regime QED and Quantum ChromoDynamics (QCD) are essentially ‘frozen’, and the SM reduces to the standard Lagrangian

$$\mathcal{L}_{QED+QCD} = \sum_f \bar{f}(i\cancel{D} - m_f)f - \frac{1}{4}F_{\alpha\beta}F^{\alpha\beta} - \frac{1}{4}G_{\alpha\beta}G^{\alpha\beta} \quad (1.1)$$

where F and G are the electromagnetic and gluonic field-strength tensors. The sum here is on fermions of mass m_f , charge eQ_f , and color $g_s t_f^a$. For a lepton, this would mean $Q_\ell = -1$ and $t_\ell^a = 0$ while for a quark $Q_q = 2/3$ or $-1/3$ and $t_q^a = \lambda^a/2$, with λ Gell-Mann matrices. To compute the matrix element between two lepton states we find:

$$\langle \ell(p_2) | J_{em}^a | \ell(p_1) \rangle = \bar{u}(p_2, m_\ell) \left(F_1^{(\ell)}(q^2) \gamma^a + F_2^{(\ell)}(q^2) \frac{i\sigma^{\alpha\beta} q_\beta}{2m_\ell} \right) u(p_1, m_\ell) \quad (1.2)$$

Here u and \bar{u} are the spinors and the two states are with momenta p_1 and $p_2 = p_1 + q$ while $F_1^{(\ell)}$ and $F_2^{(\ell)}$ are related respectively to the electric charge and the anomalous magnetic moment (AMM). In particular, for the AMM we find

$$F_2^{(\ell)}(0) = a_\ell = \frac{(g-2)_\ell}{2} \quad (1.3)$$

Even when considering non point-like particles, like nucleons $N \in \{p, n\}$ the form used in 1.2 holds and we find:

$$\langle N(p_2) | J_{em}^a | N(p_1) \rangle = \bar{u}(p_2, m_N) \left(F_1^{(N)}(Q^2) \gamma^a + F_2^{(N)}(Q^2) \frac{i\sigma^{\alpha\beta} q_\beta}{2m_N} \right) u(p_1, m_N) \quad (1.4)$$

Here $Q^2 \equiv -q^2$ and, while 1.3 holds, $F_2^{(N)}$ depends on strong dynamics. In the case of nucleons, it is often useful to introduce the *electric* and *magnetic form factors*

$$G_E^{(N)}(Q^2) \equiv F_1^{(N)}(Q^2) - \frac{Q^2}{4m_N^2} F_2^{(N)}(Q^2); \quad G_M^{(N)}(Q^2) \equiv F_1^{(N)}(Q^2) + F_2^{(N)}(Q^2)$$

It is of particular interest that, in the limit for small Q^2 , the form factors can be understood as Fourier transform of extended classical ‘charge’ distributions $\rho_i(r)$

$$F_i(Q^2) = \int d^3r e^{-iq \cdot r} \rho_i(r) = \int d^3r \rho_i(r) + \frac{1}{6} Q^2 \int d^3r r^2 \rho_i(r) + \dots$$

From this, we can write the general expression for the second moment of the charge distribution or EDM. This relation is used for example when determining the charge and magnetic radii of the proton.

$$r_i^2 \equiv \frac{1}{N} \int d^3r r^2 \rho_i(r) = -6 \frac{1}{N} \left. \frac{dF_i(Q^2)}{dQ^2} \right|_{Q^2=0}; \quad N = \begin{cases} 1 & \text{if } F_i(0) = 0, \\ F_i(0) & \text{else.} \end{cases} \quad (1.5)$$

When introducing the weak interaction we arrange fermions in *left-handed doublets* and *right-handed singlets*. We then define the *charged weak current* J_{cc}^α , a similar *neutral weak current* J_{cn}^α and we find

$$\mathcal{L}_{EW} = e A_\alpha J_{em}^\alpha + \frac{g}{\sqrt{2}} (W_\alpha^\pm J_{cc}^\alpha + h.c.) + g_Z Z_\alpha J_{nc}^\alpha; \quad J_{cc}^\alpha = \sum_\ell \bar{\nu}_\ell \gamma^\alpha P_L \ell + \sum_{ij} V_{ij} \bar{u}_i \gamma^\alpha P_L d_j \quad (1.6)$$

where $g = e/\sin\vartheta_W$, $g_Z = e/\cos\vartheta_W$ are the $SU(2)_L$ coupling expressed through the Weinberg mixing angle ϑ_W . Only the left-handed fermions are coupled (through $P_L \equiv (1 - \gamma_5)/2$) and, in the sum over the quark, the Cabibbo–Kobayashi–Maskawa (CKM) matrix V_{ij} describes the flavor-changing effect. When dealing with masses much smaller than m_W and m_Z the result is the ‘effective’ Fermi theory current-current interaction

$$\mathcal{L}_{4F} = -\frac{4G_F}{\sqrt{2}} \left(J_{cc}^\alpha (J_{cc}^\alpha)^\dagger + J_{nc}^\alpha (J_{nc}^\alpha)^\dagger \right) \quad (1.7)$$

In this equation $4G_F/\sqrt{2} = g^2/(2m_W^2)$ and using the definitions for $J_{nc/cc}^\alpha$ we end up with the vector contact interactions. In this framework photons and gluons are the only gauge bosons and the gauge symmetry of the SM $SU(3)_c \times SU(2)_L \times U(1)_Y$ is reduced to QCD and QED: $SU(3)_c \times U(1)_{em}$. We can write a 6-dimension vector operator which links 4 fermions in a generic form

$$[O_f^{XY}]_{ijkl} = (\bar{\psi}_i \gamma^\alpha P_X \psi_j)(\bar{\psi}_k \gamma_\alpha P_Y \psi_l) \quad (1.8)$$

where $X, Y \in L, R$ and i, j, k, l are generation indices. There are many such operators because ψ could be leptons or quarks but the integration of the W and Z generates only a subset (i.g. we have no cLFV operator due to accidental symmetries). In a similar fashion, an operator will be a 6-dimension scalar when removing the γ matrices or a 5-dimension dipole operator including

photons and gluons:

$$[O_{f\gamma}^D]_{ij} = (\bar{\psi}_i \sigma_{\alpha\beta} P_R \psi_j) F^{\alpha\beta}; \quad [O_{qG}^D]_{ij} = (\bar{\psi}_i \sigma_{\alpha\beta} G^{\alpha\beta} P_R \psi_j) \quad (1.9)$$

1.3.2 Beyond Standard Model at low-energy

There is no shortage of BSM models and one way of (roughly) classifying them would be by the masses and coupling strengths of the particles they introduce. Light BSM particles have small couplings to SM particles, which would explain the small contribution to physical observables. Prominent examples are dark photons, axions and Axion-Like Particles (ALPs). Axions in particular were proposed as a solution to the small value of the Charge and Parity (CP) violating QCD ϑ parameter. When discussing Heavy BSM particles we can follow the process of ‘integration’ shown for W and Z in this section, in an Effective Field Theory (EFT) approach. As long as the BSM physics respects QED and QCD gauge symmetry and involves ‘large’ mass scale Λ ($m_b < \lambda < m_W$), it can be integrated out. This way we add higher-dimensional operators to the SM Lagrangian, obtaining a Low-energy Effective Field Theory (LEFT)

$$\mathcal{L}_{LEFT} = \mathcal{L}_{QED+QCD} + \frac{1}{\Lambda} \sum_i C_i^{(5)} O_i^{(5)} + \frac{1}{\Lambda^2} \sum_i C_i^{(6)} O_i^{(6)} + \dots \quad (1.10)$$

To parameterize low-energy observables and measuring (or constraining) associated parameters is not an easy task: a prime example would be the Michel decay (which we will discuss in the following sections), generalized in terms of scalar vector and tensor contact interactions or the similar effort for the cLFV $\mu \rightarrow e\gamma$ and $\mu \rightarrow eee$ with lepton-flavor-violating contact interactions. If the BSM physics appears at a scale larger than m_W , we first have to develop a Standard Model Effective Field Theory (SMEFT). The details on how this is achieved are outside our purpose but, including all the different gauge fields, Higgs doublet, left-handed doublets, and right-handed singlet (respecting the $SU(3)_c \times SU(2)_L \times U(1)_Y$ gauge symmetry) we find

$$\mathcal{L}_{SMEFT} = \mathcal{L}_{SM} + \frac{1}{\Lambda} (C^{(5)} O^{(5)} + \text{h.c.}) + \frac{1}{\Lambda^2} \sum_i C_i^{(6)} O_i^{(6)} + \dots \quad (1.11)$$

We can now re-evaluate the matrix in 1.2 element using 1.11 instead of 1.1. We will leave the details of the calculation under the hood but the result we get is the following

$$\begin{aligned} \langle f(p_2) | J_{em}^\alpha | f(p_1) \rangle = \bar{u}(p_2, m_f) & \left(F_1^{(f)}(q^2) \gamma^\alpha + \left(F_2^{(f)}(q^2) - i\gamma_5 F_3^{(f)}(q^2) \right) \frac{i\sigma^{\alpha\beta} q_\beta}{2m_f} + \right. \\ & \left. F_4^{(f)}(q^2) \frac{1}{m_f^2} (q^2 \gamma^\alpha - 2m_f q^\alpha) \gamma_5 \right) u(p_1, m_f) \end{aligned} \quad (1.12)$$

It is of interest that the CP-violating F_3 form factor is linked to the EDM of the lepton d_f

$$d_f = \frac{eF_3^{(f)}(0)}{2m_f} \quad (1.13)$$

In the SM, d_f receives contributions from quarks at 3-loops and leptons at 4-loops (induced by CP-violation in the CKM). When considering protons and neutrons there is an additional contribution from the CP violating QCD ϑ parameter (found to be extremely low constraining the neutron EDM). For completeness sake, J_{cc}^α give rise to matrix elements between different $SU(2)$ doublets, like (ν_ℓ, ℓ) or (p, n) . This leads to muon and beta decay or quasi-elastic scattering $\ell p \rightarrow \nu_\ell n$.

1.3.3 Muon

The muon is the lepton with the intermediate mass of $m_\mu \approx 105.66$ MeV and it is unstable. The dominant process is the Michel decay $\mu \rightarrow e\nu\bar{\nu}$ which translates to a lifetime of $\tau \approx 2.2 \mu s$. We already hinted at the fact that this decay is mediated by the charged current J_{cc}^α through $\langle \nu_\mu | J_{cc}^\alpha | \mu \rangle \langle e | (J_{cc})_\alpha^\dagger | \nu_e \rangle$ which in EFT corresponds to $(\bar{\nu}_\mu \gamma^\alpha P_L \mu)(\bar{e} \gamma_\alpha P_L \nu_e)$. The resulting EFT Lagrangian is

$$\mathcal{L}_{Fermi} = -\frac{4G_F}{\sqrt{2}}(\bar{\nu}_\mu \gamma^\alpha P_L \mu)(\bar{e} \gamma_\alpha P_L \nu_e) + \text{h.h} + \mathcal{L}_{QED+QCD} \quad (1.14)$$

When evaluating the lifetime we get an equation that contains, in Δq , all corrections induced by our Lagrangian: electron mass effect, higher order QED correction, and hadronic corrections.

$$\frac{1}{\tau_\mu} \equiv \Gamma_\mu = \Gamma_0(1 + \Delta q) = \frac{G_F^2 m_\mu^5}{192\pi^3}(1 + \Delta q) \quad (1.15)$$

Unfortunately, QCD corrections are non-perturbative for $q^2 \sim m_\mu^2$ and are the leading theoretical uncertainty. These corrections are known at NNLO. Precision measurement of the muon lifetime is key for consistency checks of the SM. In fact G_F can be related to m_W and m_Z

$$\frac{4G_F}{\sqrt{2}} = \frac{g^2}{2m_W^2}(1 + \Delta r) = \frac{2\pi}{\sin^2 \vartheta_W m_W^2}(\Delta r) \quad (1.16)$$

Here Δr are the SM corrections and $\sin^2 \vartheta_W = 1 - m_W^2/m_Z^2$.

On top of the Michel decay, we also have radiative and rare decays

$$\mu \rightarrow e\nu\bar{\nu}\gamma, \quad \mu \rightarrow e\nu\bar{\nu}e^+e^- \quad (1.17)$$

for which we have $B(\mu \rightarrow e\nu\bar{\nu}\gamma) \sim 1.3 \times 10^{-2}$ (for $E_\gamma > 10$ MeV) and $B(\mu \rightarrow e\nu\bar{\nu}ee) \sim 3.6 \times 10^{-5}$. At last, we arrive at the ‘golden’ channels for cLFV studies:

$$\mu \rightarrow e\gamma, \quad \mu \rightarrow eee, \quad \mu^- \stackrel{A}{Z}N \rightarrow e^- \stackrel{A}{Z}N \quad (1.18)$$

With non-vanishing neutrino masses, the branching ratios for these processes are expected to be below 10^{-50} . To extract constraints on BSM physics from the branching ratios we can mostly use standard perturbative methods with the Lagrangian 1.10. For the muon conversion, additional precautions are needed due to the nuclear matrix elements $\langle \stackrel{A}{Z}N | J | \stackrel{A}{Z}N \rangle$ as well as the study of the Decay In Orbit (DIO), electrons for which the energy spectrum was modified by the nuclear recoil.

The last two properties of interest of the muon are the AMM (eq. 1.3) and EDM (eq. 1.13). After the results of the G-2 experiment at Fermi National Accelerator Laboratory (FERMILAB),

there is some tension on the first between experimental results and theory. For the EDM the SM value is zero for practical purposes and a non-vanishing result would be a clear indication of BSM. We will further discuss the muon EDM.

1.3.4 Muon decay

When using a charge-changing Hamiltonian characterized by fields with define chirality [5], the general matrix element of the muon decay can be written as [7]

$$M = 4 \frac{G_F}{\sqrt{2}} \sum_{\substack{\gamma=S,V,T \\ \varepsilon,\mu=R,L}} g_{\varepsilon\mu}^{\gamma} \langle \bar{e}_{\varepsilon} | \Gamma^{\gamma} | (\nu_e)_n \rangle \langle (\bar{\nu}_{\mu})_m | \Gamma_{\gamma} | \mu_{\mu} \rangle \quad (1.19)$$

In this definition, we find: γ indicates a 4-scalar, 4-vector or 4-tensor; Γ Dirac (or Pauli) matrices; ε, μ indicate the chirality of the spinors; m, n the chirality of the neutrinos. This means that the physical interpretation of $g_{\varepsilon\mu}^{\gamma}$ is quite straightforward: $n_{\gamma}|g_{\varepsilon\mu}^{\gamma}|^2$ is the probabilit of a μ -handed muon decaying in a ε -handed electron by the interaction Γ^{γ} (n_{γ} are required for the correct normalization). In this picture, the SM corresponds to $g_{LL}^V = 1$ with all other couplings to 0. **Review chirality vs helicity**

Observables Neglecting radiative corrections, we find the differential decay probability: with reduced energy in $[x, x + dx]$; along \hat{x}_3 with an angle $[\vartheta, \vartheta + d\vartheta]$ with respect to the muon polarization \mathbf{P}_{μ} ; spin along $\hat{\zeta}$.

$$\frac{\partial^2 \Gamma}{\partial x \partial \cos \vartheta} = \frac{m_{\mu}}{4\pi^3} W_{e\mu}^4 G_F^2 \sqrt{x^2 - x_0^2} \cdot \{F_{IS}(x) \pm P_{\mu} \cos \vartheta F_{AS}(x)\} \cdot \{\hat{\zeta} \cdot \mathbf{P}_e(x, \vartheta)\} \quad (1.20)$$

Here, $W_{e\mu} = \max(E_e) = (m_{\mu}^2 + m_e^2)/2m_{\mu}$ is the maximum e^{\pm} energy and $x = E_e/W_{e\mu}$ is the reduced energy ($x_0 = m_e/W_{e\mu}$). This spectrum has both an isotropic (F_{IS}) and anisotropic part (F_{AS}). The electron polarization $\mathbf{P}_e(x, \vartheta)$ can be parametrized by *Michel parameters*, which are combinations of the coupling constants $g_{\varepsilon\mu}^{\gamma}$. If the neutrinos' and x_0 are neglected, 1.20 becomes

$$\frac{\partial^2 \Gamma}{\partial x \partial \cos \vartheta} \sim x^2 \left\{ 3(1-x) + \frac{2\rho}{3}(4x-3) + 3\eta x_0 \frac{(1-x)}{x} \pm P_{\mu} \xi \cos \vartheta \left[1 - x + \frac{2\delta}{3}(4x-3) \right] \right\} \quad (1.21)$$

Here ϑ is the angle between the electron momentum and the muon spin and $x \equiv 2E_e/m_{\mu}$. In the SM we get the following, in which we find the total rate used in 1.15. $\rho = \xi\delta = 3/4$, $\xi = 1$, $\eta = 0$

$$\frac{\partial^2 \Gamma}{\partial x \partial \cos \vartheta} = \frac{G_F^2 m_{\mu}^5}{192\pi^3} [3 - 2x \pm P_{\mu} \cos \vartheta (2x - 1)] x^2 \quad (1.22)$$

The way the $g_{\varepsilon\mu}^{\gamma}$ are connected to the nine decay parameters [3, 10], or the 10 intermediate quantities we can measure [3], is outside the purpose of this short review. The bottom line is that a 20-dimensional space of the complex $g_{\varepsilon\mu}^{\gamma}$ can be mapped to a 10-dimensional space. Unfortunately, many of these parameters are intertwined, and (generally) the precise measurement of individual parameters does not give conclusive information on the type of interaction. To avoid being too vague we will take an example from [2]. The rate S of the reaction $\nu_{\mu} e^- \rightarrow \mu^- \nu_e$, normalized to

the rate predicted by $V - A$ and assuming a negative helicity for ν_μ , has been found close to 1 [17]. S depends on five coupling constants $\{g_{LL}^v, g_{RL}^v, g_{LR}^s, g_{RR}^s\}$ but four of these parameters are found to be small, and in first approximation, we find [7]:

$$S = |g_{LL}^v|^2; \quad |g_{LL}^s| < 2\sqrt{1 - S} \quad (1.23)$$

1.3.5 Electric Dipole Moment

Similarly to how the permanent Magnetic Dipole Moment (MDM) μ represents the coupling between the spin of a quantum system and an external magnetic \mathbf{B} field, the EDM d represents the coupling between the spin of and an external electric field \mathbf{E} . The Hamiltonian describing the spin dynamics, indicating the Pauli matrices with σ , is then:

$$\hat{H} = -\mu\hat{\sigma} \cdot \mathbf{B} - d\hat{\sigma} \cdot \mathbf{E} \quad (1.24)$$

Given that $\hat{\sigma} \cdot \mathbf{E}$ is odd for time reversal, the existence of a non-zero EDM would violate CP symmetry. This is an interesting topic, with many implications, and key to many searches. In a magnetic field, the dynamic of a particle at rest is described by $ds/dt = \boldsymbol{\mu} \times \mathbf{b} = \omega_L \times \mathbf{s}$, where $\boldsymbol{\mu} = ge/(2m)\mathbf{s}$ is the MDM and $\omega_L = -2\mu B/\hbar$ the Larmor precession frequency. Similarly a hypothetical EDM $\mathbf{d} = \eta e/(2mc)\mathbf{s}$ results in a precession $\omega_d = -2d\mathbf{E}/\hbar$ in an electric field \mathbf{E} . When considering a moving particle in both fields it is useful to introduce the polarization vector $\Pi = \mathbf{s}/s$ and the Thomas precession Ω_0

$$\frac{d\Pi}{dt} = \Omega_0 \times \Pi, \quad \Omega_0 = -\frac{e}{m\gamma} \left[(1 + \gamma a)\mathbf{B} - \frac{a\gamma^2}{\gamma + 1}(\boldsymbol{\beta} \cdot \mathbf{B})\boldsymbol{\beta} - \gamma \left(a + \frac{1}{\gamma + 1} \right) \frac{\boldsymbol{\beta} \times \mathbf{E}}{c} \right] \quad (1.25)$$

[4][5] If there is no electrical field parallel to the momentum the acceleration is purely transverse so we get the following motion, with Ω_c the cyclotron frequency.

$$\frac{d\boldsymbol{\beta}}{dt} = \Omega_c \times \boldsymbol{\beta}, \quad \Omega_c = -\frac{e}{m\gamma} \left(\mathbf{B} - \frac{\gamma^2}{\gamma^2 - 1} \frac{\boldsymbol{\beta} \times \mathbf{E}}{c} \right) \quad (1.26)$$

The relative spin precession of a muon in a storage ring will be then given by (T-BMT [**miss-59**])

$$\begin{aligned} \boldsymbol{\Omega} = \boldsymbol{\Omega}_0 - \boldsymbol{\Omega}_c &= \underbrace{\frac{q}{m} \left[a\mathbf{B} - \frac{a\gamma}{\gamma + 1} (\boldsymbol{\beta} \cdot \mathbf{B})\boldsymbol{\beta} - \left(a + \frac{1}{1 - \gamma^2} \right) \frac{\boldsymbol{\beta} \times \mathbf{E}}{c} \right]}_{\text{Anomalous precession, } \omega_a = \omega_L - \omega_c} \\ &\quad + \underbrace{\frac{\eta q}{2m} \left[\boldsymbol{\beta} \times \mathbf{B} + \frac{\mathbf{E}}{c} - \frac{\gamma c}{\gamma + 1} (\boldsymbol{\beta} \cdot \mathbf{E})\boldsymbol{\beta} \right]}_{\text{Interaction of EDM and relativistic } \mathbf{E}, \omega_a} \end{aligned} \quad (1.27)$$

The second term describes the precession due to the EDM coupling to the relativistic \mathbf{E} , perpendicular to the \mathbf{B} in which the particle is moving. The simplification shown are the result of \mathbf{p} , \mathbf{B} and \mathbf{E} forming an orthogonal basis, hence the scalar products are null. In the case of the E821 experiment, the muon *magic* momentum was chosen, simplifying eq. 1.27 and making the anomaly

precession frequency independent from the electric fields needed for beam steering.

$$p_{magic} = \frac{m}{\sqrt{a}} = 3.09 \text{ GeV}/c, \quad \boldsymbol{\Omega} = \frac{q}{m} \left[a \boldsymbol{B} + \frac{\eta}{2} \left(\boldsymbol{\beta} \times \boldsymbol{B} + \frac{\boldsymbol{E}}{c} \right) \right] \quad (1.28)$$

In the presence of a muon EDM the plane would be tilted and a vertical precession ($\omega_e \perp \boldsymbol{B}$), shifted by $\pi/2$ to the horizontal anomalous precession, would become observable.

Paul Scherrer Institute (PSI) has been for decades at the frontier in the measurements of the neutron EDM. More on this will follow in this chapter when describing the existing limits on EDMs.

[6]

1.4 Experimental status

To give an exhaustive recap of the experimental development, both worldwide and at PSI, is a task we will not undertake. Here we will briefly discuss the key experiments in CLFV searches (MEG, Mu3e, Mu2e, COMET) and the nEDM experiment at PSI. This choice is driven by the experiment extensively discussed in the following chapters: muEDM; MEG II.

1.4.1 CLFV experiments

Process	Upper limit	reference
$\mu^+ \rightarrow e^+ \gamma$	4.2×10^{-13}	[7]
$\mu^+ \rightarrow e^+ e^+ e^-$	1.0×10^{-12}	[8]
$\mu^- \text{Ti} \rightarrow e^- \text{Ti}$	1.7×10^{-12}	[8]
$\mu^- \text{Au} \rightarrow e^- \text{Au}$	7×10^{-13}	[9]
$\mu^+ e^- \rightarrow \mu^- e^+$	8.3×10^{-11}	[10]
$\tau^\pm \rightarrow e^\pm \gamma$	3.3×10^{-8}	[11]
$\tau^\pm \rightarrow \mu^\pm \gamma$	4.4×10^{-8}	[11]
$\tau^- \rightarrow e^- e^- e^+$	2.7×10^{-8}	[12]
$\tau^- \rightarrow \mu^- \mu^- \mu^+$	2.1×10^{-8}	[12]
$\tau^- \rightarrow e^- \mu^- \mu^+$	2.7×10^{-8}	[12]
$\tau^- \rightarrow \mu^- e^- e^+$	1.8×10^{-8}	[12]
$\tau^- \rightarrow e^+ \mu^- \mu^-$	1.7×10^{-8}	[12]
$\tau^- \rightarrow \mu^- e^- e^-$	1.5×10^{-8}	[12]
$\pi^0 \rightarrow \mu e$	3.6×10^{-10}	[13]
$K_L^0 \rightarrow \mu e$	4.7×10^{-12}	[14]
$K^+ \rightarrow \pi^+ \mu^+ e^-$	1.3×10^{-11}	[15]
$K_L^0 \rightarrow \pi^0 \mu^+ e^-$	4.4×10^{-10}	[13]
$Z^0 \rightarrow \mu e$	7.5×10^{-7}	[16]
$Z^0 \rightarrow \tau e$	9.8×10^{-6}	[17]
$Z^0 \rightarrow \tau \mu$	1.2×10^{-6}	[17]

Fig. 1.1: Experimental upper limits for a variety of CLFV processes.

	$\mu^+ \rightarrow e^+ \gamma$	$\mu^+ \rightarrow e^+ e^- e^+$	$\mu^- N \rightarrow e^- N$
Background	Accidental	Radiative muon decay	Decay in orbit
Beam	Continuous	Continuous	Pulsed
Current limit	4.2×10^{-13} MEG [7]	1×10^{-12} SINDRUM [8]	7×10^{-13} SINDRUM II [18]
Planned/running	MEG II [19][20][21]	Mu3e [22][23][21]	Mu2e [24] [25] COMET [26][27][28][29]
Planned sensitivity	$\sim 6 \times 10^{-16}$	$\sim 10^{-16}$	$\sim \text{few} \times 10^{-17}$

Fig. 1.2: Overview of muon CLFV experiments

MEG

The MEG experiment [7] is designed based on two key concepts: the utilization of a liquid xenon detector (LXe) for photons detection, and the implementation of an anti-bottle magnetic field for positron tracking. Muons are stopped within a polyethylene target located at the magnet's center. The momentum of positrons is measured using a combination of drift chambers (DCH) and plastic scintillator timing counters (TC). Photon energy and direction, on the other hand, are determined in a liquid xenon volume containing over 800 photo-multiplier tubes. The measured quantities include electron and photon energies (E_e and E_γ), as well as relative positions (angles $\theta_{e\gamma}$, $\varphi_{e\gamma}$) and time $t_{e\gamma}$. Achieving resolutions that effectively separate background signals, such as radiative muon decays, necessitates an energy resolution of $\lesssim 1\%$ for both particles.

MEG's magnetic field is not uniform to avoid the accumulation of positrons emitted at low-pitch angles within the tracker. Instead, the magnetic field diminishes symmetrically from the center towards the periphery, pushing the particles away from the center. The specific field shape is chosen so that the track radius is proportional to the *absolute* momentum rather than the transverse momentum. This allows low-energy positrons to be discarded by positioning the detector at a sufficient distance from the magnet axis. The magnetic system of MEG, known as "COnstant Bending RAdius" (COBRA) magnets, possesses this distinctive feature.

The DCH spectrometer comprises 16 trapezoidal drift chambers filled with He-C₂H₆, arranged radially. The radial coordinate is determined using the timing data collected by the DCH and TC, while the z position is inferred from the induced charge on the zig-zag-shaped pads on the drift chamber sides. The momentum resolution for positrons is approximately 330 keV.

The choice of employing a liquid xenon scintillating detector for photon reconstruction is motivated by the aim to minimize passive material within the detector and achieve excellent time resolution. This choice provides a higher light yield and shorter decay time compared to other options, such as NaI crystals. The timing resolution for measuring photon interaction time is below 100 ps.

MEG successfully gathered 7.5×10^{14} stopped muons between 2008 and 2013 and, as previously mentioned, established the world's best limit on the branching ratio of $\mu^+ \rightarrow e^+ \gamma$ at 90% confidence level, with $\text{BR}(\mu^+ \rightarrow e^+ \gamma) < 4.2 \times 10^{-13}$ [7].

MEG II The upgraded MEG II experiment was proposed to reduce the contamination due to the accidental background that could not be further reduced in MEG [19] [20]. MEG II is currently running and a whole part (Part III) of this thesis will be dedicated to this experiment.

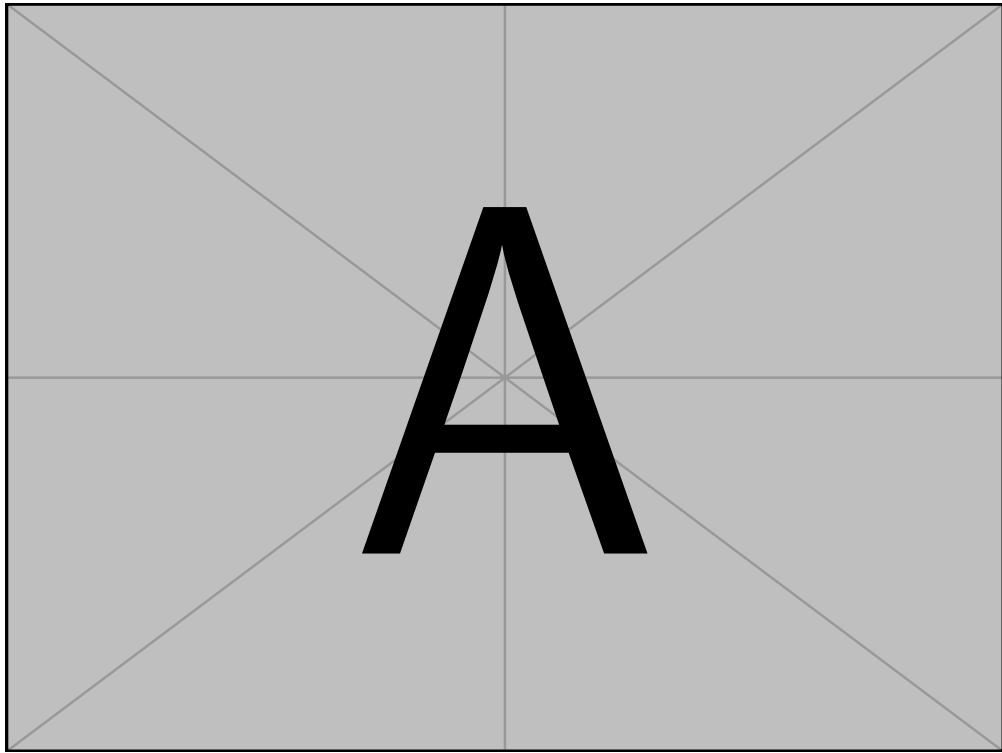


Fig. 1.1: Pictorial view of the MEG experiment [30][7].

Mu3e

The goal of the Mu3e experiment is to achieve a single-event sensitivity on the $\mu^+ \rightarrow e^+e^+e^-$ decay at the order of 10^{-16} [23]. This experiment will utilize the same muon beam as MEG II and employ a thin hollow double-cone Mylar target to stop muons. The detector will be a 2 m cylinder situated within a 1.5 T magnetic field and divided into 5 sections (Fig. 1.3). The central station will consist of two double layers of pixel detectors and a scintillating fiber tracker, while the other four stations will consist of two layers of pixel sensors and a scintillator hodoscope. A visual representation of the Mu3e apparatus can be seen in Fig. 1.2. To mitigate the impact of multiple Coulomb scattering, which poses limitations on precise track reconstruction, the tracker will utilize High Voltage Monolithic Active Pixel (HV-MAPS) technology, designed to partially cancel out the scattering effect within half of a turn. The estimated resolutions for time and vertex are $\sigma_t \approx 100$ ps and $\sigma_{xy} \approx 200$ μm , respectively, while the momentum resolution ranges from 100 to 400 keV for particles with momenta between 10 and 53 MeV/c [1]. The Mu3e experiment is planned in three phases [1], as depicted in Fig. 1.3:

- Phase Ia: Beam with an intensity of $\mathcal{O}(10^7)$ μ^+/s and installation of the tracker only.
- Phase Ib: Beam with an intensity of $\mathcal{O}(10^8)$ μ^+/s (currently the maximum at PSI) with the addition of scintillating fibers and two additional tracking stations.
- Phase II: Beam with an intensity of $\mathcal{O}(10^9)$ μ^+/s (requires a new beam-line) and inclusion of the remaining two stations to achieve the single-event sensitivity of 10^{-16} .

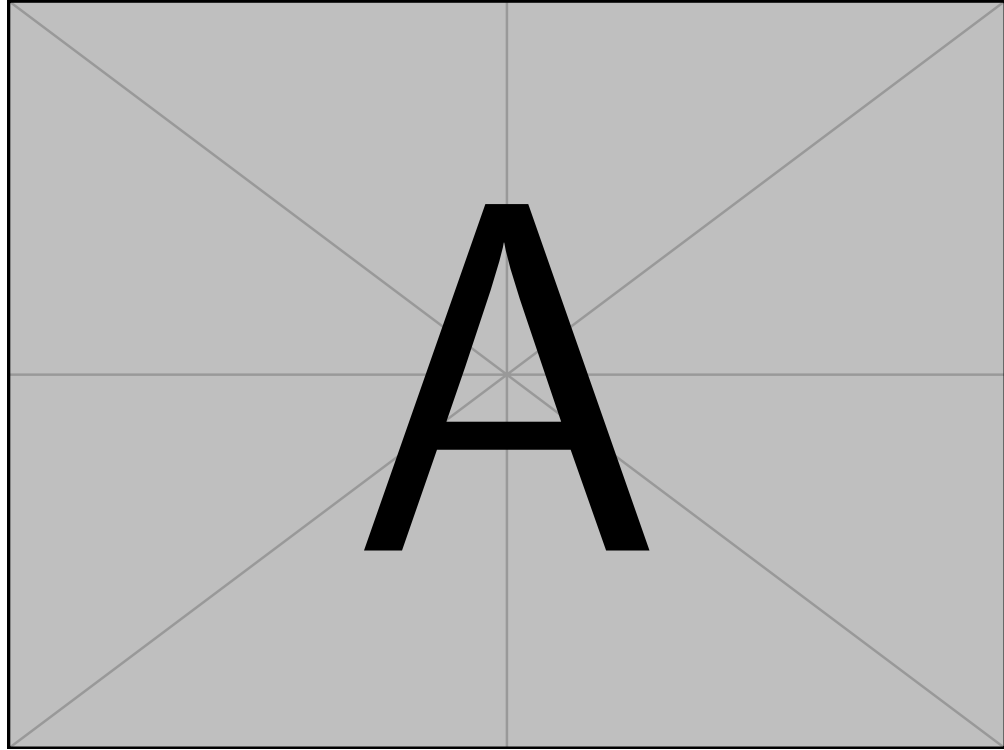


Fig. 1.2: Pictorial view of the Mu3e apparatus [21].

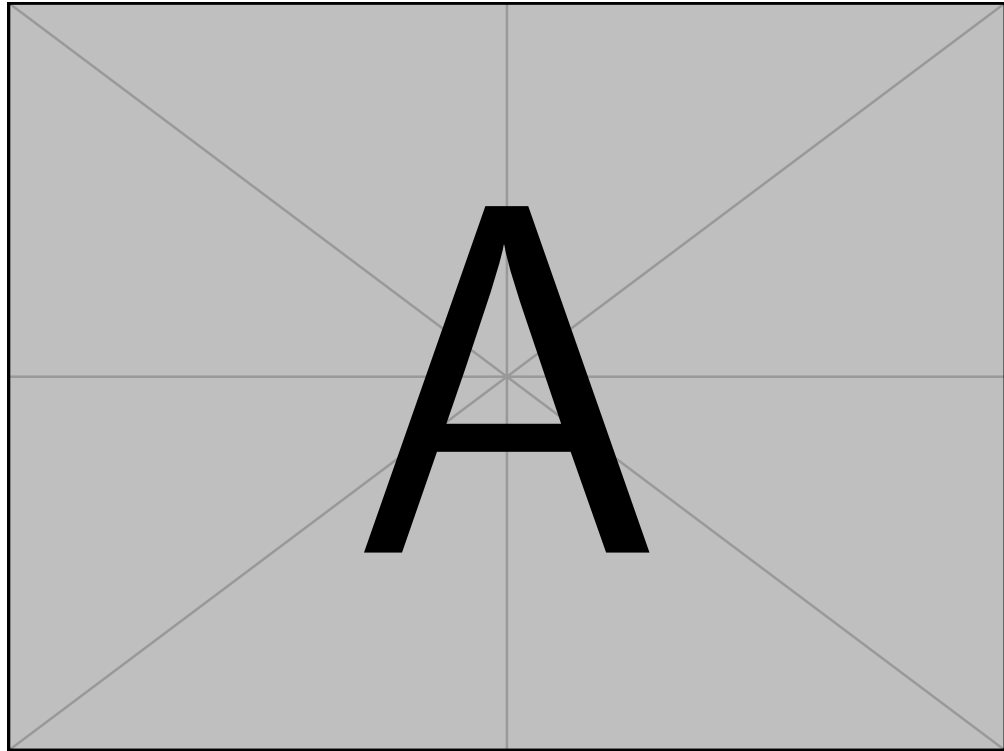


Fig. 1.3: A sketch view of the Mu3e apparatus [31] and the various phases.

Mu2e

Mu2e employs an 8 GeV, 25 kW pulsed proton beam with 100 ns wide bunches separated by 1.7 μ s. Figure ?? illustrates the experimental setup, which consists of three sections: the Production

Solenoid, Transport Solenoid, and Detector Solenoid. The magnetic field layout around the production target is graded to guide the particles into the transport section. Within this section, the gradient directs the particles towards the stopping target, while the S shape reduces background from neutral particles and enables charge sign selection using Eq. ?? and collimators. Generally, only negative muons with momenta below 100 MeV/c reach the stopping target. Downstream of the aluminum target, the straw tube tracker and crystal electromagnetic calorimeter are located. Both detectors feature a hollow-cylinder geometry, with the tracker consisting of crossed straw tubes grouped in 20 stations and the calorimeter composed of two identical disks made of CsI crystals read by SiPMs. With three years of data taking, Mu2e aims to achieve an expected sensitivity of $R_{\mu e} < 3 \times 10^{-17}$ [25].

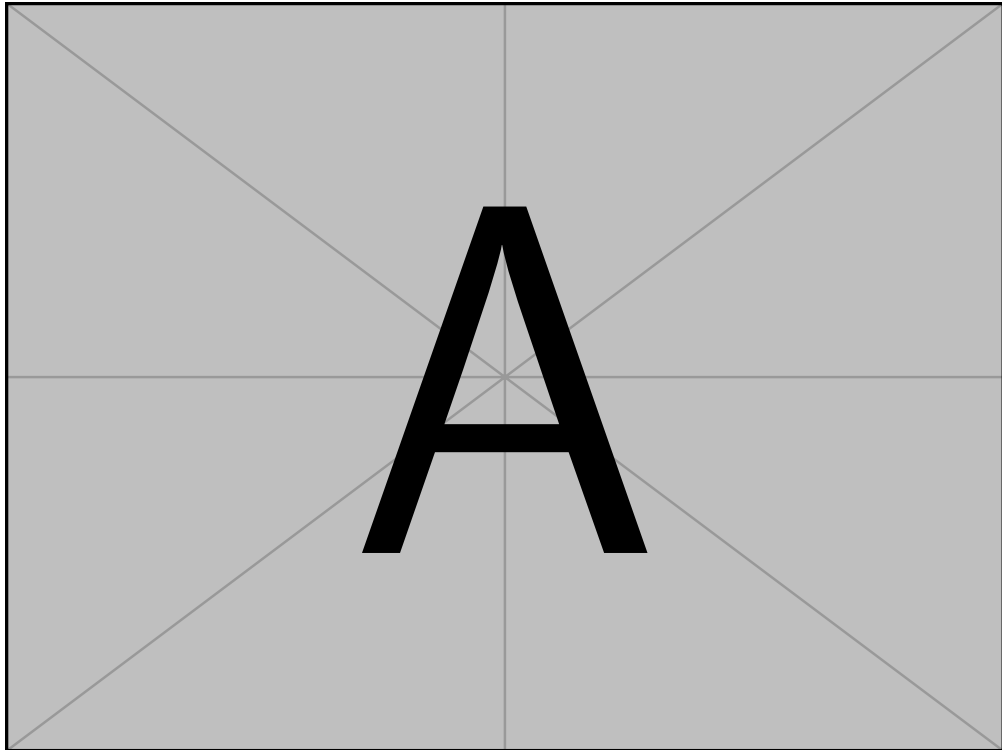


Fig. 1.4: Pictorial view of the muon beam-line of the Mu2e experiment [25].

Mu2e is a collaborative project involving international partners, including the Italian Institute of Nuclear Physics, responsible for constructing the electromagnetic calorimeter. The Mu2e Collaboration is also conducting preliminary investigations for the upgraded Mu2e II [32]. The proton beam intensity will be enhanced through the PIP-II upgrade [33], resulting in a higher rate of stopped muons on target, increasing from $10^{10} \mu^-/\text{s}$ (Mu2e) to $10^{11} \mu^-/\text{s}$. For the upgraded Mu2e II, new detector technologies are being explored. Simulation studies indicate that with three years of data acquisition, Mu2e II is expected to achieve a sensitivity of $R_{\mu e} < 3 \times 10^{-18}$.

COMET

The COherent Muon-to-Electron Transition (COMET) experiment is currently being constructed at the Japanese Proton Accelerator Research Center (J-PARC) [29]. While sharing similarities with Mu2e, such as the use of an 8 GeV, 56 kW pulsed proton beam with a bunch separation of $1.17 \mu\text{s}$, COMET differs in two main aspects, as illustrated in Fig. 1.5:

- The presence of a C-shaped transport solenoid, instead of an S-shaped one, enables a tighter selection of muon momentum, at the cost of reduced beam intensity (approximately 70)
- An additional curved solenoid after the stopping target eliminates most of the non-interesting electrons before they reach the tracker.

The development of COMET will occur in two phases: Phase-I and Phase-II (Fig. 1.5).

COMET Phase-I This initial phase aims to establish the experimental techniques, study background effects, and achieve an intermediate measurement at $R_{\mu e} \approx 7 \times 10^{-15}$. The proton power will be limited to 3.2 kW, and a single 90° bend will be employed. The main challenge lies in the short distance between the various elements, with a cylindrical drift chamber serving as the electron tracker. Scintillating hodoscopes will surround the tracker for triggering and timing purposes. The Technical Design Report (TDR) for COMET Phase I can be found in [29].

COMET Phase-II To accommodate the increased particle rate, COMET Phase-II will introduce a straw tube tracker and a crystal electromagnetic calorimeter utilizing LYSO crystals. The entire magnetic system will be expanded and refined. The two-step approach is driven by uncertainties in the understanding of the underlying physics processes. Firstly, the backward production by 8 GeV protons remains poorly known, despite results from the HARP experiment [34]. Additionally, data on muon nuclear capture in aluminum is still limited, although efforts from the Mu2e and COMET collaborations have led to the development of the AlCap experiment at PSI [35][36][37]. The AlCap collaboration aims to measure the rate and spectra of particles emitted during muon capture in aluminum to improve the physics models employed in Monte Carlo simulations.

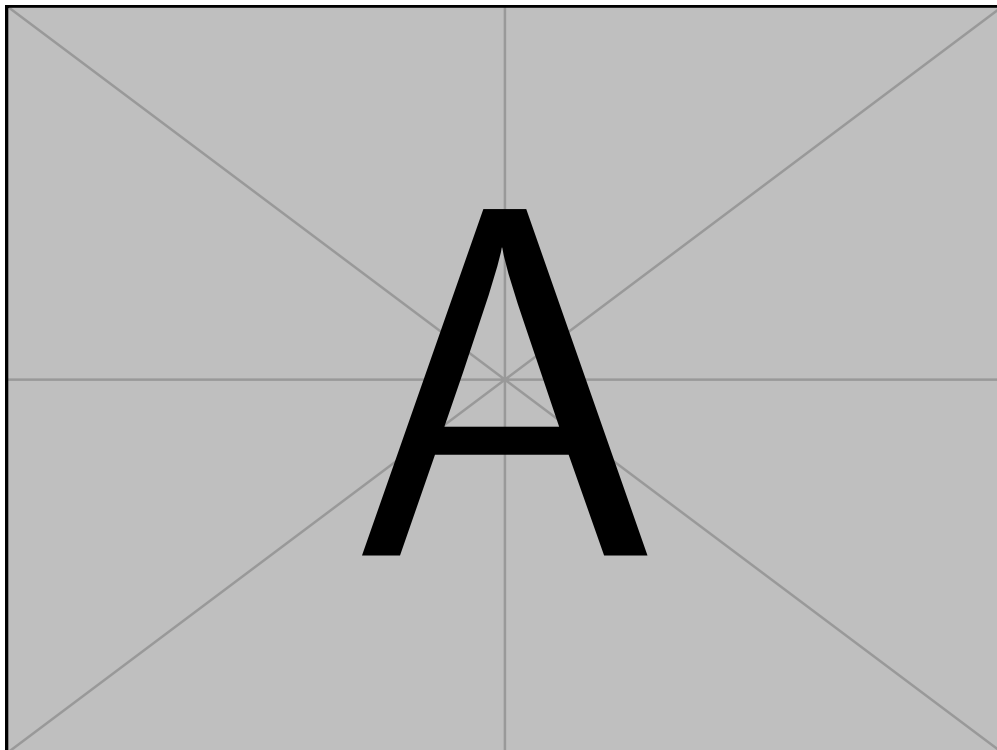


Fig. 1.5: Pictorial view of the COMET apparatus [29].

Experiment	Particle	EDM limit in ecm
nEDM [38]	n	0.18×10^{-25}
ACME [39]	e	1.1×10^{-29}
Indirect [40]	μ	$0.19 \times 10^{-19*}$
g-2 [41]	μ	1.8×10^{-19}

Fig. 1.3: Sumary of the current limits on the EDM for neutron electron and muon.

1.4.2 EDM experiments

In the last decades, the interest towards EDM measurements and limits played an important part in testing old and new theories. A summary of (some of) the current limits is in Tab. 1.3. This subsection is a rundown of the experiments setting these limits.

Neutron: nEDM

The current upper limit on the neutron EDM comes from the apparatus built by the RAL/Sussex/ILL collaboration [38] using the PSI UCN source (see 1.5.3): the measured result of $d_n = (0 \pm 1.1_{stat} \pm 0.2_{sys}) \times 10^{-26}$ ecm translates to an upper limit of $|d_n| < 1.8 \times 10^{-26}$ ecm (90% CL). The method used was to determine the change in Larmor precession frequency of neutrons ($f_n = \frac{1}{\pi\hbar} |\mu_n \mathbf{B}_0 + d_n \mathbf{E}|$) using the spectrometer sketched in Fig. 1.6. This frequency is correlated to the change in polarity of the electric field. Each cycle of measurement consisted in:

- Polarizing UCNs with a 5 T solenoid, selecting the initial state with a spin flipper
- Confining them in the precession chamber to the equilibrium density of ~ 2 UCN/cm³
- A small quantity of polarized ¹⁹⁹Hg vapor was injected as comagnetometer
- Different low-frequency pulses were used to tip Hg or UCNs spins by $\pi/2$
- The detection system counts both spin-up (\uparrow) and down (\downarrow) states
- For each cycle i, the asymmetry is evaluated: $A = (N_\uparrow - N_\downarrow)/(N_\uparrow + N_\downarrow)$.

An interesting detail is that, to compensate for residual magnetic-field fluctuations and drifts, the frequency ratio $R = f_n/f_{Hg}$ was used.

n2EDM Any significant improvement on the limit requires a completely new setup. With this aim the n2EDM was developed [42]. This measurement will (again) rely on the estimation of the precession frequency f_n of polarized ultracold neutrons in weak B and strong E fields:

$$d_n = \frac{\pi\hbar}{2|E|}(f_{n,\uparrow\downarrow} - f_{n,\uparrow\uparrow})$$

Key aspects are the size and quality of the cylindrical storage chambers and the precision of the magnetometry, which will rely on mercury and cesium. A sketch of the concept design is in Fig. 1.7 and the whole design in Fig. 1.8. Other sizable improvements, here not discussed, will be the further optimization of the production and transport of the UCN from the source as well as the improved magnetic shielding.

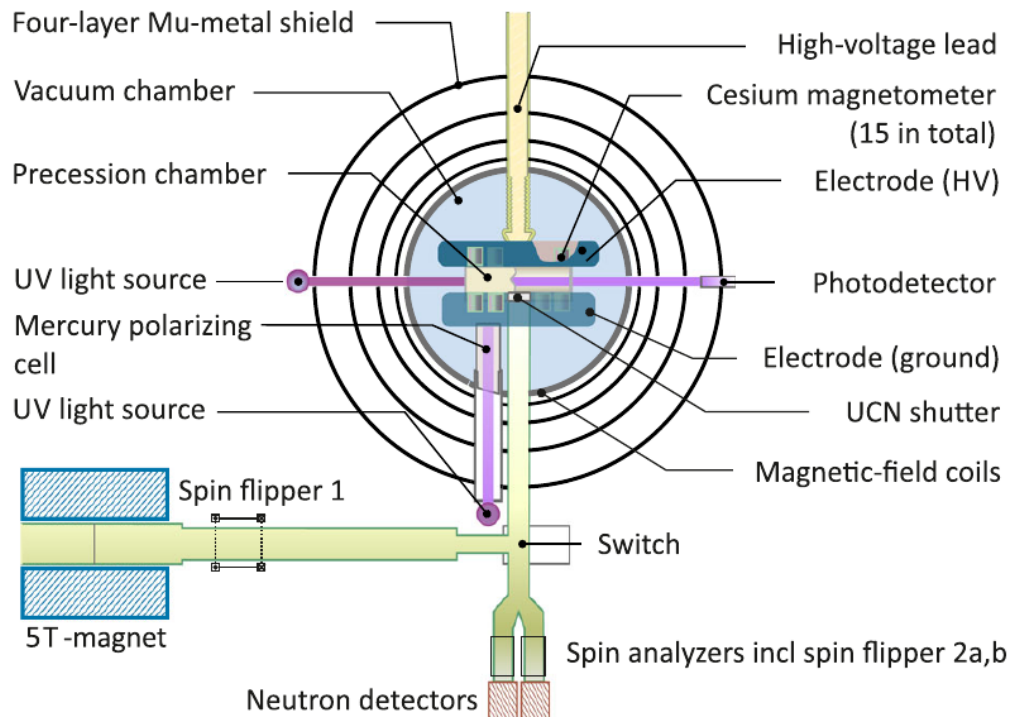


Fig. 1.6

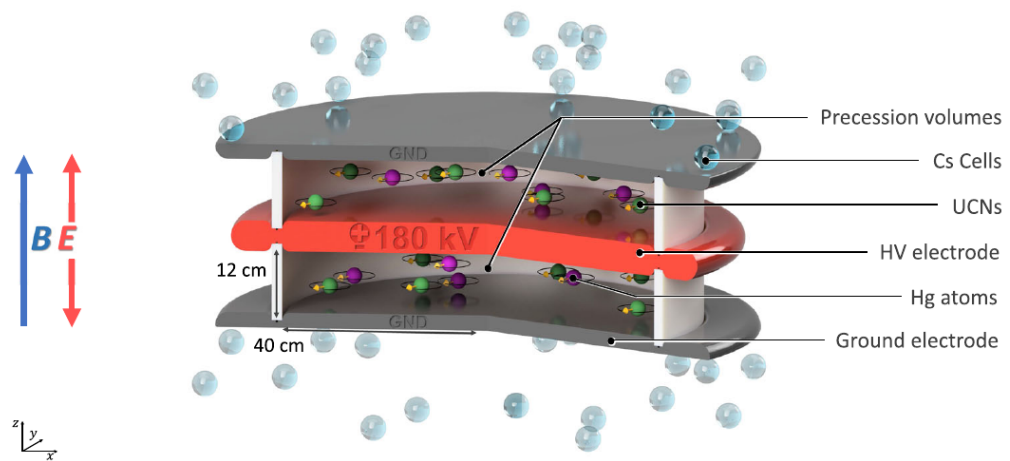


Fig. 1.7

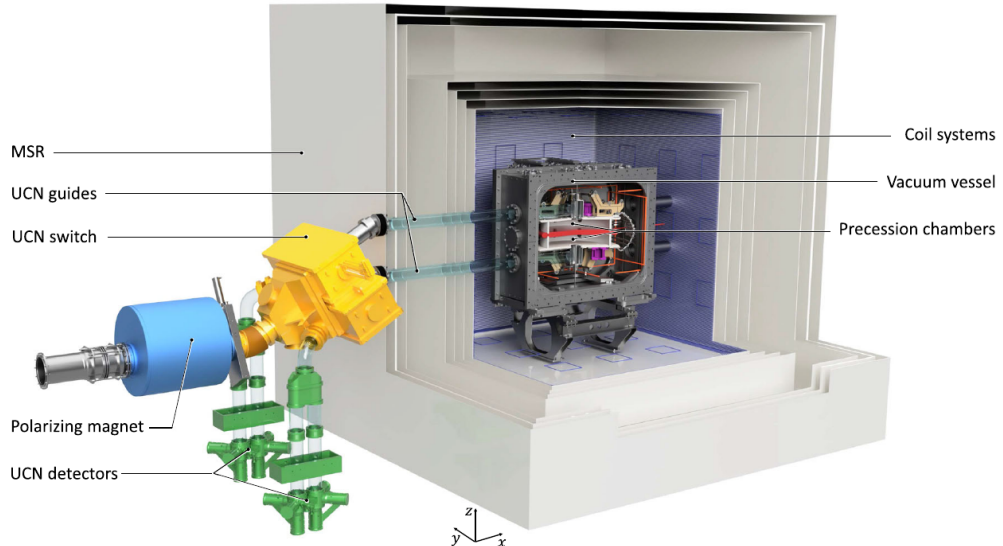


Fig. 1.8

Electron

The conventional way to measure EDM is the separated oscillatory fields method: when a particle is subjected to an electric field parallel to a weak magnetic field the EDM interaction changes the Larmor frequency [43]. An alternative approach is to use solid-state techniques: in the presence of a strong magnetic field the EDM of valence electrons in a paramagnetic insulator would generate a small magnetization. Even though the effect is negligible for singular electrons, the cumulative effect can be detected using sensitive magnetometry. Using this method the limit $d_e < 6.05 \times 10^{-25} \text{ e} \cdot \text{cm}$ was obtained in $\text{Eu}_{0.5}\text{Ba}_{0.5}\text{TiO}_3$ [44]. Not long after, a different limit was set with the same technique in Gadolinium Gallium Garnet (GGG, $\text{Gd}_3\text{Ga}_5\text{O}_{12}$): $d_e = -5.57 \pm 7.89 \pm 0.12 \times 10^{-25} \text{ e} \cdot \text{cm}$ [45]. The choice of material is driven by:

- A strong magnetic response, generated by the high density of Gd^{3+} ions ($\sim 10^{-22} \text{ cm}^{-3}$), each with 7 unpaired electrons in $4f$ shell
- High dielectric strength (10 MV/cm) and electrical resistivity

ACME The current limit on eEDM was actually set by the ACME collaboration [39] using a different method: measuring the spin precession in a superposition of quantum states. As illustrated in Fig. 1.9, the measuring principle is the following:

- A collimated beam of ThO enters a E, B fields region
- A combination of lasers creates a spin state aligned with \hat{x}
- The spin precesses in the E, B fields
- The final spin alignment is readout by a laser: the resulting fluorescence depends on the angle between the laser linear polarization and the spin direction

The key aspect is that the precession frequency is linked to the states of the system and is modified by the presence of d_e . The results obtained is $d_e = (4.3 \pm 3.1 \pm 2.6) \times 10^{-30} \text{ e} \cdot \text{cm}$. Applying the Feldman–Cousins prescription this value translates to the limit $|d_e| < 1.1 \times 10^{-29} \text{ e} \cdot \text{cm}$.

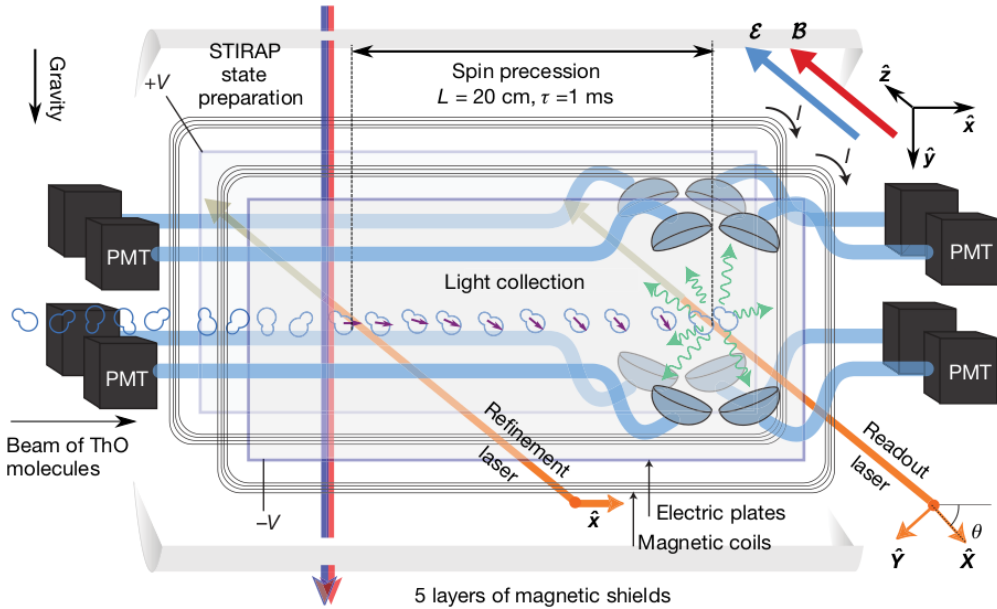


Fig. 1.9

Muon

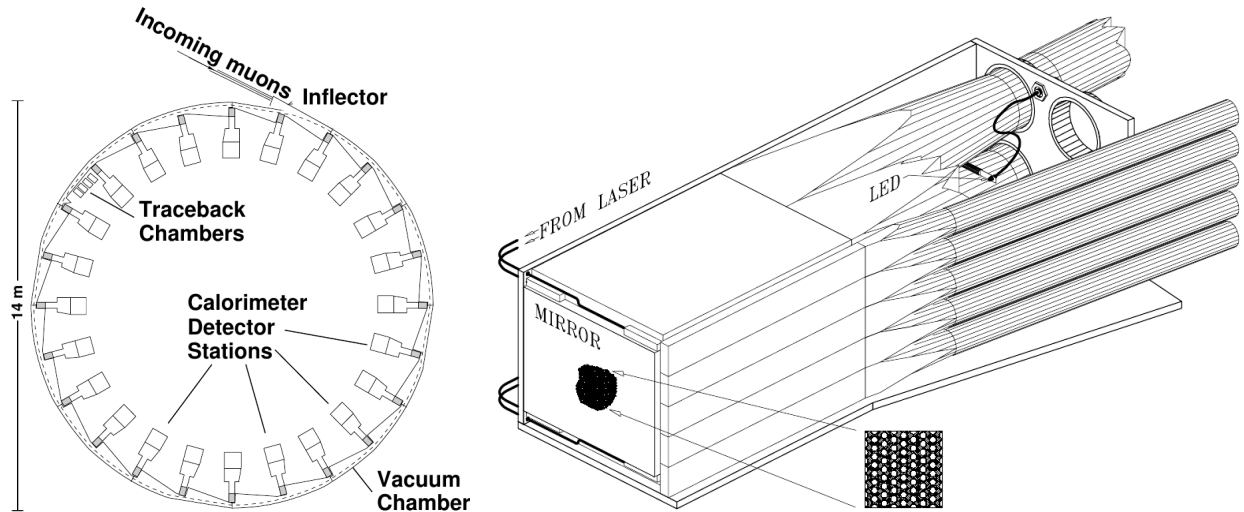
We now come to the muon, to which most of this thesis is dedicated. The d_μ search at PSI is going to be discussed in detail in the following chapters but we will here review the current limits. These are the references for the direct [41] and indirect [40] limits, where all the missing details can be found.

Muon g-2 In 2018 the $g-2$ collaboration performed three independent searches for d_μ . All results were compatible with a null value and a combined upper limit was set: $|d_\mu| < 1.9 \times 10^{-19} \text{ e} \cdot \text{cm}$ [41]. We will here skip the details but we will outline the methods used and the results (all 95% CL). Three additional detectors were added to the BNL experiment to measure the EDM measuring the positrons coming from the muon decay. In Fig. 1.10a a sketch of the $g-2$ ring and the different detectors.

- Front Scintillator Detectors (FSD): stacks of five horizontal scintillators to measure oscillation of the average vertical position. A sketch of such a detector is in Fig. 1.10b. The analysis of the data collected in 2000 yielded: $|d_{\mu^+}| < 2.9 \times 10^{-19} \text{ ecm}$
- Position-Sensitive Detectors (PSD): a version of FSD that is segmented both horizontally and vertically. $|d_{\mu^-}| < 1.5 \times 10^{-19} \text{ ecm}$
- Traceback Wire Chamber (TWC): series of eight, three-layer drift tube planes in front of one of the calorimeters (a sketch is shown in Fig. 1.11). these are used to track the positrons back to the storage volume. The analysis conducted on the 1999-2000 data with this detector yielded: $|d_{\mu^+}| < 3.2 \times 10^{-19} \text{ ecm}$

Indirect limit Given the rise in interest for EDM measurements an effort was undertaken to assess the indirect constraints imposed on d_μ by the EDM measurements performed with heavy atoms and molecules [40]. This was done by evaluating the d_μ - induced *Shift moment*¹ of the ^{199}Hg

¹As pointed out in [46], this is the operator inducing the atomic EDM.



(a) Layout of the g-2 storage ring with the de-
(b) Sketch of the Front Scintillation Detectors (FSD). The Position-
tector stations and the Traceback Chambers. Sensitive Detector (PSD) is not shown but is set in front of the FSD.

Fig. 1.10: Sketches of the g-2 storage ring and the detector used to measure the muon EDM.

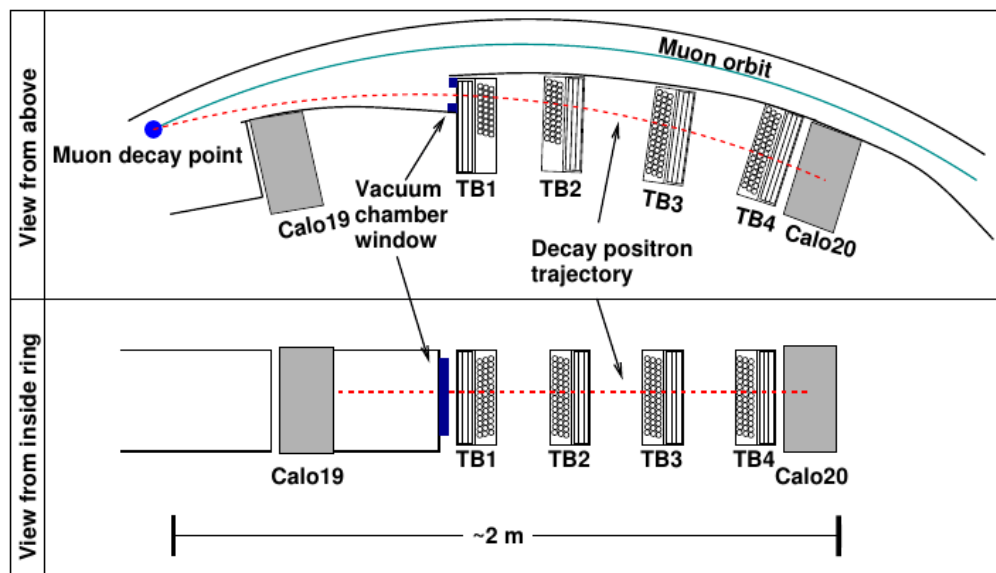


Fig. 1.11: The Traceback Wire Chamber is the most complex detector added for the EDM measurement. It consists of eight three-layer drift tube planes to propagate the positron track back to the decay point.

nucleus, and a specific CP-odd operator for ThO. The results, $d_\mu(^{199}\text{Hg}) < 6.4 \times 10^{-20} \text{ e} \cdot \text{cm}$ and $d_\mu(\text{ThO}) < 1.9 \times 10^{-20} \text{ e} \cdot \text{cm}$, are more stringent than the current measured limit but are *indirect*. This means that an assumption on lepton universality is done when considering this limit.

1.5 The beams at PSI

1.5.1 High-Intensity Proton Accelerator facility

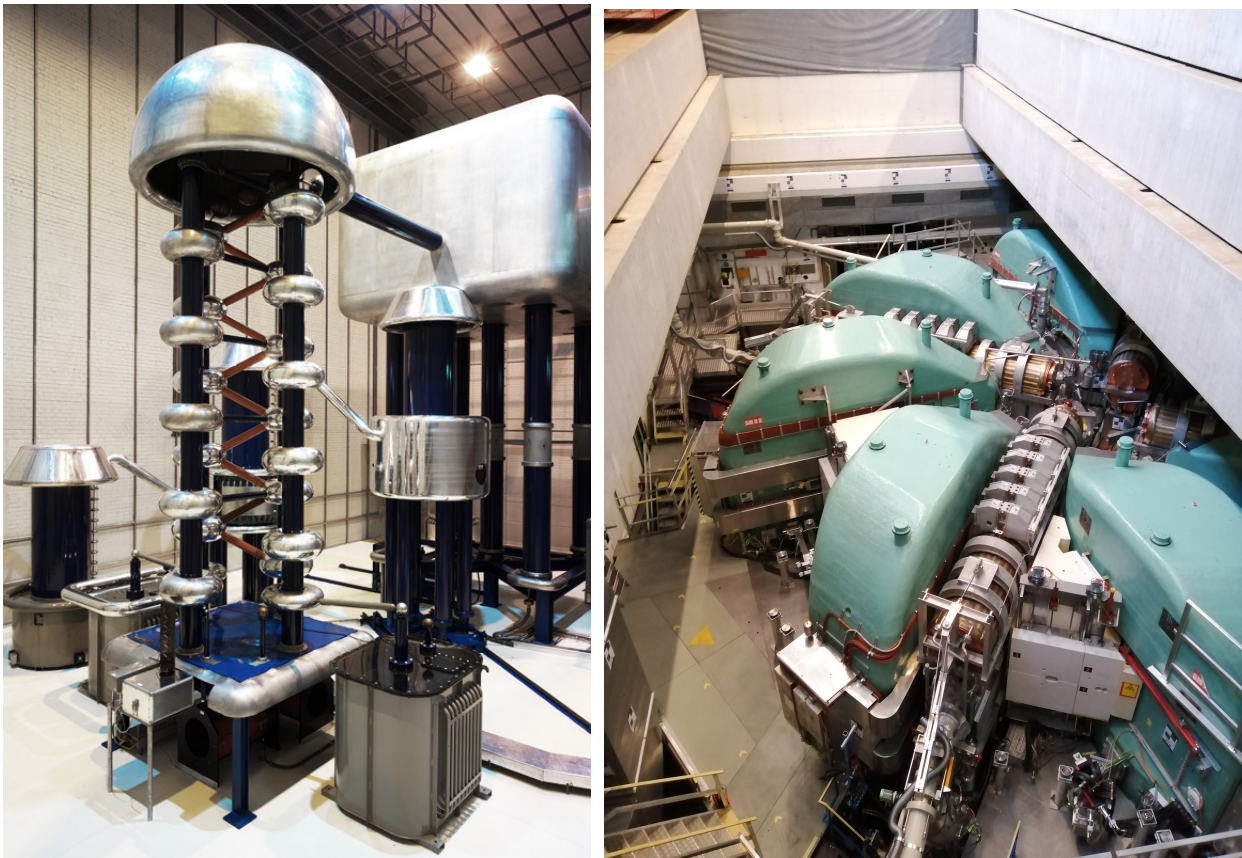
The proposal for the accelerator facility at PSI was completed in 1963. The objective was to develop a proton beam of tens of microAmpere and energy above 450 MeV to produce π/μ . The main accelerator is a cyclotron designed to accelerate the beam from 72 MeV to 590 MeV. The first pre-accelerator, Injector I cyclotron, was developed to accelerate protons and light ions up to 72 MeV and 180 μA . The performances steadily improved up to 180 μA but the beam losses at the extraction from the Injector I were the bottleneck. The Ring cyclotron was deemed to have the potential to surpass 2 mA. For this reason, in 1978, the proposal of using two pre-accelerators was approved: a 860 keV Cockcroft-Walton (CW) followed by a new Injector II cyclotron.

Since 2010 the chain is the following:

- Protons are produced by an electron cyclotron resonance source with a 60 kV extraction
- Two solenoids focus the protons onto a collimator: here $^2\text{H}^+$ and $^3\text{H}^+$ ions are stopped
- Protons are then accelerated in three stages
 - From 60 keV to 870 keV by the CW DC linear accelerator, shown in Fig. 1.12a
 - The beamline connecting the CW to the Injector II is equipped with a bunching system to match the acceptance of Injector II
 - Injector II accelerates the pre-bunched beam up to 72 MeV. An electrostatic beam splitter can redirect a fraction of the beam extracted beam (up to 100 μA) to produce radioisotopes
 - The beam is sent to the Ring cyclotron, shown in Fig. 1.12b. Eight magnets keep the particles on the spiral path and four cavities accelerate the beam up to 590 MeV
- After the acceleration the beam is extracted and sent to the meson production targets
- The surviving $\sim 65\%$ of the beam is sent to the spallation source SINQ (or to a beam dump)

Injector II The Injector II cyclotron is designed for high-current operation (1 mA and above) with minimal extraction losses. It achieves high extraction efficiency through a combination of factors: high accelerating voltage, large radius, large gap magnets, and low energy spread. To counter space charge forces, a high vertical betatron tune² is employed. Injector II is a low-field separate sector machine with four wedge sectors, accommodating two high-voltage double-gap resonators and two single-gap flat-top resonators. Its 870 keV injection energy allows for beam collimation and halo cleanup, being below the Coulomb threshold. The "vortex motion" is an interesting phenomenon caused by space charge in isochronous cyclotrons [47]. For long initial bunches, self-sustaining round sub-bunches are generated, while for short and compact bunches, the vortex effect stabilizes the bunch [48] [49]. The PSI operation crew discovered the usefulness of self-focusing, achieving high extracted currents with low losses by operating in an accelerating

²Refers to the number of vertical or horizontal oscillations that a particle undergoes per turn in a cyclotron, indicating the level of vertical or horizontal focusing.



(a) CW feeding the Injector II

(b) Picture of the Ring cyclotron.

Fig. 1.12: Picture of two of the stages of the HIPA facility: the Cockcroft-Walton bringing the proton up to 870 keV and the Ring cyclotron accelerating them up to 590 MeV.

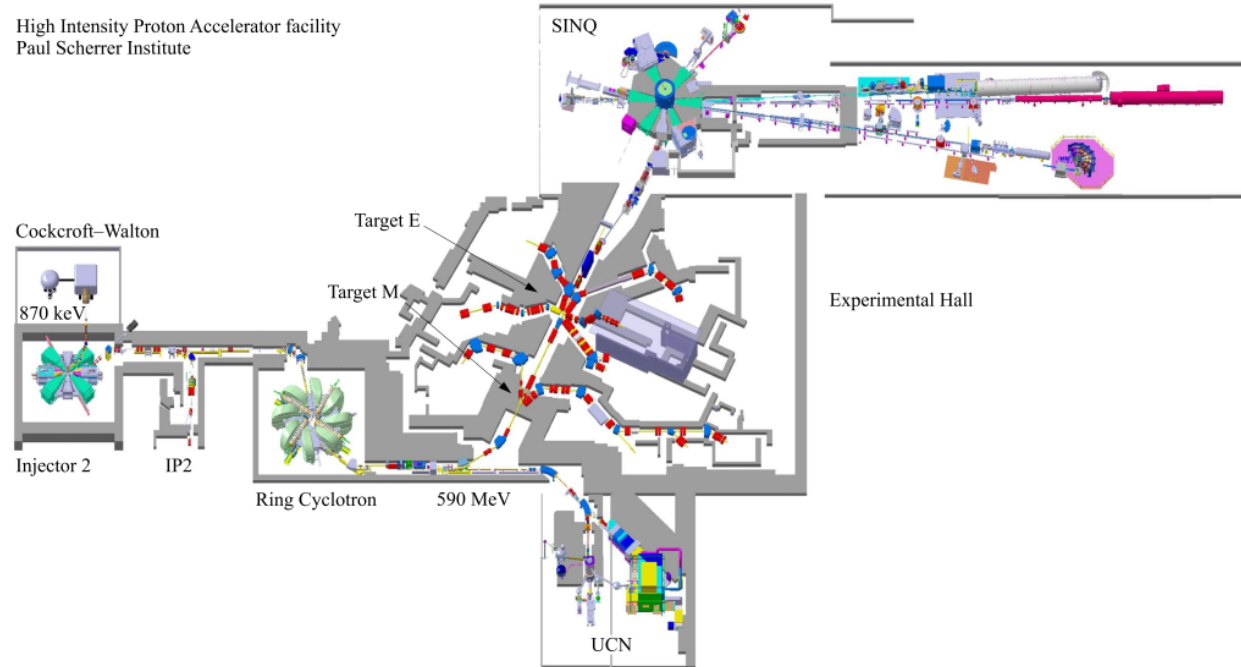


Fig. 1.13: High Intensity Proton Accelerator (HIPA) facility at PSI

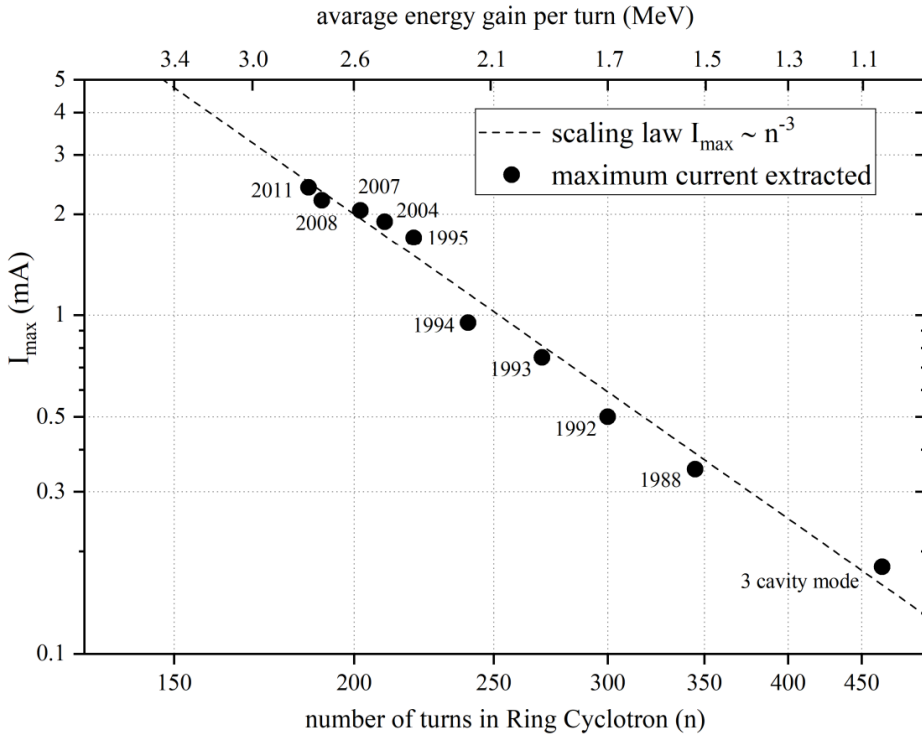


Fig. 1.14: In 1981, Werner Joho introduced Joho’s N3-Law, an analysis of high-intensity issues in cyclotrons [50]. This law states that the current limit dominated by losses scales inversely with the third power of the number of turns in the cyclotron: $I_{max} \propto N^{-3}$. Remarkably, this formula accurately predicted the performance of the PSI Ring cyclotron for the subsequent two decades.

mode without the need for the flat-top system. In an ongoing upgrade program, Injector II will replace the flat-top resonators with two 50MHz high-voltage resonators. This upgrade aims to reduce extraction losses and enable higher beam currents. Notably, Injector II is the only known production cyclotron worldwide that harnesses the vortex effect.

Ring cyclotron Over time, the Ring cyclotron’s performance was improved, particularly its extraction efficiency. Initially, a well-centered beam was required to pass the Walkinshaw resonance³ without significant loss. However, by December 1976, an extraction efficiency of 99.9% was achieved with a peak intensity of 112 µA. Ten years later, Injector II alone achieved a beam current of 1mA, and in combination with the Ring cyclotron, reached 310 µA. To increase the intensity, the Ring underwent an RF system upgrade, while a bunching system was implemented in the injection line. The upgrades allowed for a reduction in Ring turns, resulting in a production current of 2.2 mA and a beam power of 1.3 MW, in line with Joho’s N^3 -Law (see Fig. 1.14). Further upgrades, including the replacement of the 150MHz flattop cavity, are expected to enable a beam current of 3 mA and power of SI1.8MW for both Injector II and the Ring cyclotron.

Performances

HIPA operates at a beam power of up to 1.42 MW. The maximum beam power (1.42 MW) is limited by the activation and damage of the accelerator components while the maximum beam

³The Walkinshaw resonance is a phenomenon in cyclotrons where beams experience a resonance with the machine’s magnetic field modulation. Proper alignment and adjustments are necessary to prevent significant beam loss.

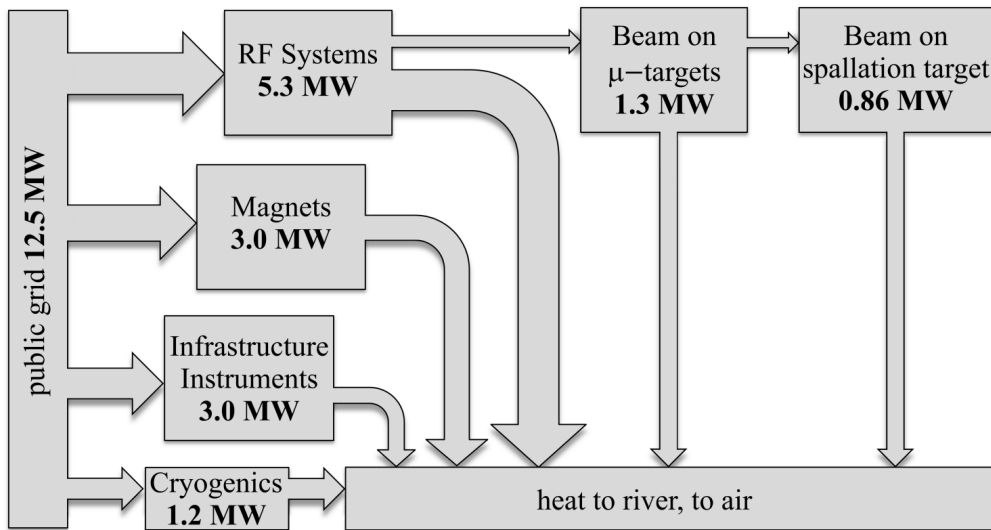


Fig. 1.15: Detail of the power usage of the HIPA facility.

current authorized is 2.4 mA. The increase of the beam power in the period between 1974 to 2020 is shown in Fig. 1.16. The history of the delivered charge to the meson production targets and SINQ is shown in Fig. 1.17. A major limiting factor is the scattering of halo particles in the extraction septum. There are two key elements for low-loss beam extraction: the generation of beam tails must be suppressed as best as possible and the turn separation at the extraction septum must be maximized. In this way, the density of halo particles at the position of the extraction septum is minimized. The beam is operated 24/7 around 200 days a year. Every three weeks of operation two days of maintenance are scheduled. The details of the different particle production are discussed in the following subsections.

Power The experiments at HIPA require high-intensity particle beams for precise measurements, which consume significant electrical power. Upgrades aim to achieve higher particle flux and brightness, necessitating even greater power. Considering the global energy consumption challenges, improving HIPA's energy efficiency is crucial. Fig. 1.15 displays the power consumption breakdown of the proton facility. During routine operation at a beam current of 2.2 mA, 1.3 MW, the overall power consumption is approximately 12.5 MW leading to an efficiency of 11%. For the bare accelerator, the figure is 18%. The RF-to-beam power conversion accounts for the majority of this consumption, around 5.4 MW. It scales linearly with beam power, while the power consumption of magnets and auxiliary systems remains independent of the beam power. It can be shown that the efficiency can increase with higher current and the aim is >20% with 3 mA.

1.5.2 Meson production

As we saw in 1.5.1, High Intensity Proton Accelerator (HIPA) delivers a continuous 2.4 mA 590 MeV proton beam. To have a high pion/muon yield a low Z material is the best choice for the Meson Production Targets: graphite has been used since 1990's. The whole system (target, collimators, beam dumps, ...) has to be cooled and, due to nuclear reactions, is highly radioactive. Pions are produced by the interaction with nucleons in the target (threshold at 280 MeV in the center-of-mass frame) and muons are then produced by pion decay. When π are stopped at ~ 1

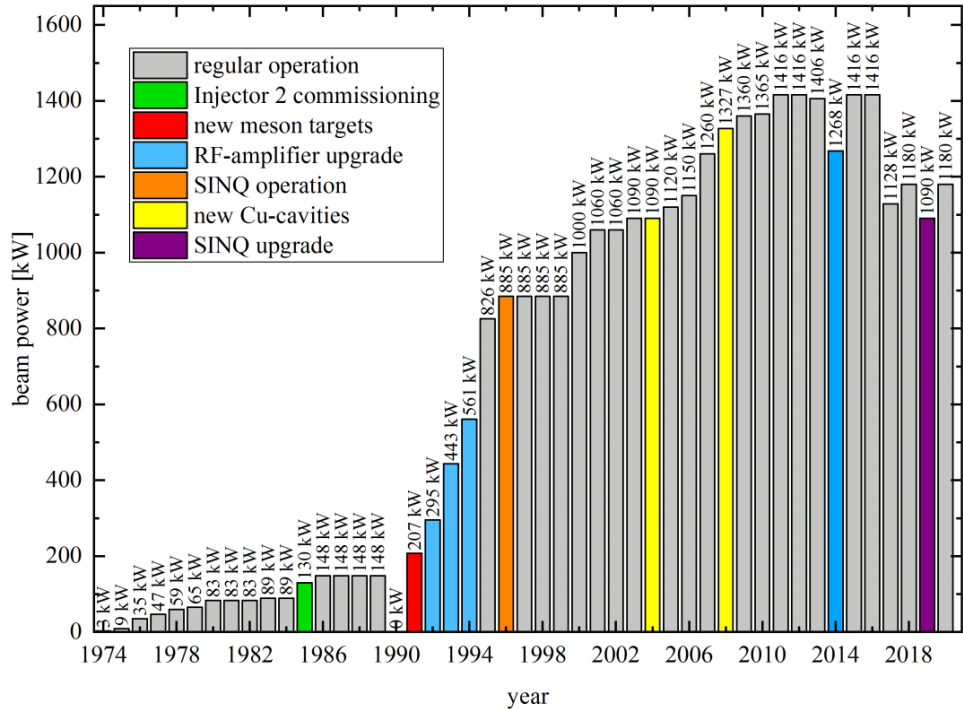


Fig. 1.16: History of the power of the HIPA proton beam.

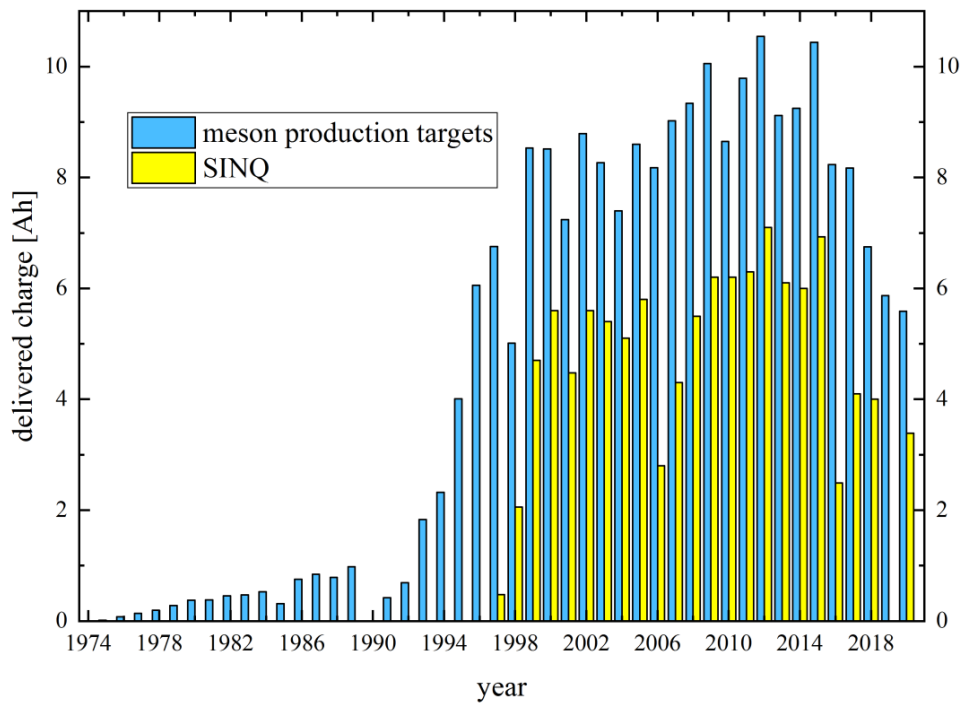


Fig. 1.17: History of the charge delivered by the HIPA beam on the meson production targets and SINQ.

Target	User facility	Particles	Momenta (MeV/c)	Rate ($s^{-1}mA^{-1}$)
M (5 mm)	$\pi M1$	$e/\pi/\mu/p$	10-450	2×10^8
	$\pi M3.1-3$	μ	10-40	3×10^6
E (4/6 cm)	$\pi E1$	$\pi/\mu/p$	10-450	1×10^9
	$\pi E3$	μ	10-40	3×10^7
	$\pi E5$	π/μ	10-120	5×10^8
	$\pi E1$	μ	60-120	6×10^7
	$\pi E4$	μ	10-40	4×10^8

Fig. 1.4: Particle types available at the meson facilities. The rate in particles per second per 1 mA of proton

mm from the surface of the target, μ^+ can escape and are called *surface muons*. These muons have energies below 4.1 MeV ($p = 29.8$ MeV) and are $\approx 100\%$ polarized. Muons created by in-flight decay have higher energies and are cooled *cloud muons*. Both positive and negative muons are possible but the negative charge is suppressed by a factor ~ 3 . There are two targets: M feeds two beamlines (PiM1 and PiM3; E feeds 5 beamlines (PiE1, MuE1, MuE4, PiE3, PiE5). The detail of the facilities are summarized in Tab. 1.4. The targets are graphite wheels which rotate to distribute the heat due to the impinging beam. The material is polycrystalline graphite made of small crystallites of $\sim 20\text{ }\mu\text{m}$ irregularly arranged.

E Target The target is inserted vertically into the beamline and held by a horizontal rotating shaft. The graphite and the hub are connected by six spokes. While operated at 2 mA, the temperature of this 40 mm/60 mm target is ~ 1700 K. Water-cooled copper shields are mounted on the rear of the target. To reduce the deformations the graphite rim is made of 12 segments. Variations of the beam positions are crucial and to improve the sensitivity the graphite wheel was modified: small grooves were applied on both sides. This modulates the beam transmission. At the end of 2019 a new target wheel was tested, having a small angle for the impinging beam. This *slanted target* keeps the effective thickness creating a larger active surface and two different spots for IN-/OUT of the beam. The net effect is an increase $\sim 50\%$ in the surface muons. As the bearings degrade from heat and radiation they have to be replaced after a few months of operation. The procedure for the maintenance of the target here will not be discussed.

M Target This target is smaller in thickness and the bearings are far from the beam thus the demands are less challenging. The rim of the target is 2 cm wide and 2 mm thick. With an impinging angle of 30 deg the effective thickness is 5.2 mm inducing a beam loss of 1.6%. The target operates at 1100 K and is cooled by conduction. For the upcoming High Intensity Muon Beam (HIMB) the aim is to increase the muon rate by a factor up to 100. For this purpose studies for an upgrade of the M target station, with a slanted target design, are ongoing. A similar slanted target was already tested in the E target station, yielding a $\sim 50\%$ increase in surface muon rate.

Collimators and Beam dump Just like target E, Collimators and beam dump are inserted vertically and shielded. Both are made of oxygen-free copper: improve thermal conductivity; avoid hydrogen embrittlement⁴; for brazing of the steel tubes onto the copper body. To avoid any signif-

⁴Hydrogen can be produced by the spallation reaction of the protons with copper. This hydrogen can bond with oxygen creating water molecules that can produce cracks in the copper.

icant change in the material, the copper is kept below 400 K using water-cooling. The collimator system as well as the beam dump have to stand more than 100 kW per component. The water flows in stainless steel pipes are wound outside and brazed on the cylindrical body. This is done to avoid direct contact of the proton beam with the water, which would create corrosion-inducing ions. The main body is made of six slices brazed together. The shape and manufacture of these sections were optimized using computational fluid dynamics in order to reduce the energy deposit and thermal stress. An aperture, made of 4 slits of 100 μm Nikel foils, is mounted in front of the devices. Here free electrons from ionization are collected and used for beam position and size monitoring. Aside from a water leak problem, likely due to thermal stress, no visible signs of radiation damage are observed since installation.

1.5.3 Neutron production

SINQ

The first spallation neutron source built at PSI was SINQ, which has dedicated neutron scattering instruments and was used as a polarized cold-neutron beam line for fundamental neutron physics. After passing through the meson production target the proton energy is degraded to 570/565 MeV. The beam is bent downwards and then up vertically onto the spallation target. The thermal neutron flux scales with the beam current and is $\sim 1.5 \times 10^{14} \text{ cm}^{-2}\text{s}^{-1}$ near the target. This beamline was used for many measurements conducted in preparation for the UCN source and many parameters of UCN production (and loss) were here determined.

UltraCold Neutrons

Neutrons below 4 mK are called UltraCold. This corresponds to energy below 300 neV, which is comparable with the gravitational potential of a neutron at a few meters height and also the neutron optical potential: material bottles can hence contain UCNs. The design of the UCN source, shown in Fig. 1.18, was presented in 2000 to push the sensitivity of the nEDM search.

Source setup The HIPA 590 MeV proton beam is deflected by a magnetic kicker and sent in the spallation source. Each spallation reaction with the lead atoms leads to an average of 8 neutrons, which are then thermalized in heavy water. The main moderator is made of solid deuterium at 5 K. The UCN produced exit the moderator's vessel through a thin aluminum lid in a vertical guide and their energy is lost to gravity. From here the UCN are delivered via long neutron guides: two at the bottom and one at the top of the vessel. The 30 liters of solid D₂ is the core of the whole system and takes several days to achieve a good ice quality. UCN intensity reflects the quality of the achieved solid deuterium, as shown in Fig. 1.19 exemplifying a typical UCN intensity behavior during such a slow freezing process.

Performance A key parameter in the performance of a UCN source is the number of particles delivered. The exponential decay measured at the lower ports reflects the emptying time of the central storage vessel. Measuring in the higher port a faster exponential is found, demonstrating that the UCNs with energies high enough to reach that port are quickly drained. Several studies to understand all aspects of the UCN source have been conducted since its inauguration, as well

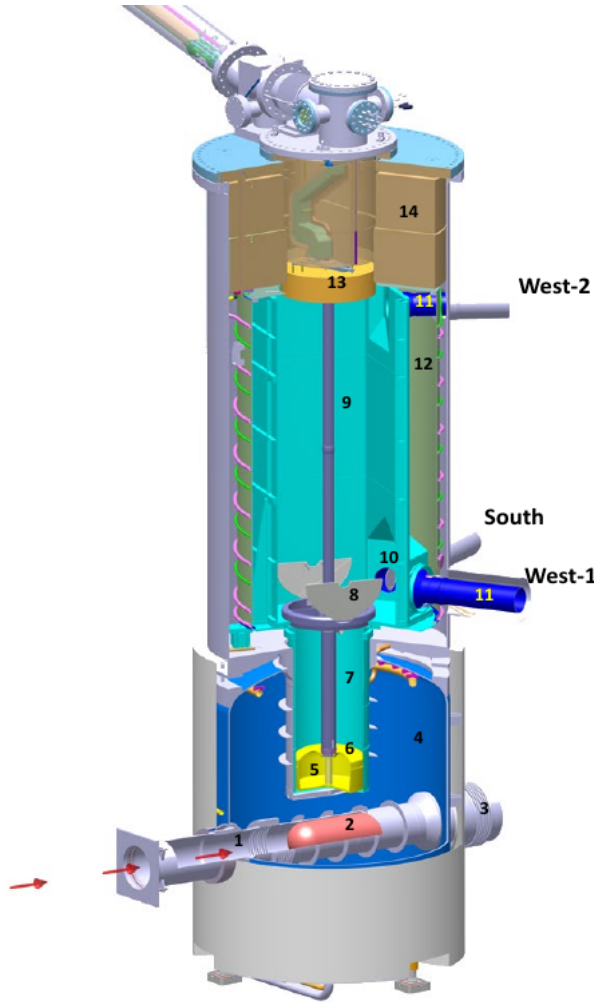


Fig. 1.18: CAD for the UCN source taken from [2]. Some of the key aspects are: 2 - lead spallation source, 4 - heavy water moderator, 5 - D_2 moderator, 9 - storage vessel, 10 - 11 UCN guide and guide shutter.

as the UCN transport from production in the solid deuterium to a beam port. A slow decrease in performance was discovered and a temperature-cycling “conditioning” was developed to regain maximum UCN intensity. The UCN source has been reliably operating since 2011 (see Fig. 1.20).

Results The resulting nEDM limit $d_n = (0.0 \pm 1.1_{stat} \pm 0.2_{sys}) \times 10^{-26}$ ecm (see 1.4.2) was published in 2020 [38] but other results were also obtained thanks to this facility:

- A measurement of the mercury-to-neutron magnetic moment ratio
- Spin-echo spectroscopy with ultracold neutrons
- Measurement of gravitational depolarization of ultracold neutrons
- limit for oscillating electric dipole moments
- limit for spin-dependent forces mediated by axion-like particles

1.5.4 High-Intensity Muon Beams

Currently, PSI delivers the most intense continuous muon beam in the world with up to a few $10^8 \mu^+/\text{s}$. The High-Intensity Muon Beams (HiMB) project at PSI focuses on the development of a new target station and muon beamlines to deliver up to $10^{10} \mu^+/\text{s}$ [51][52]. The aim is to boost

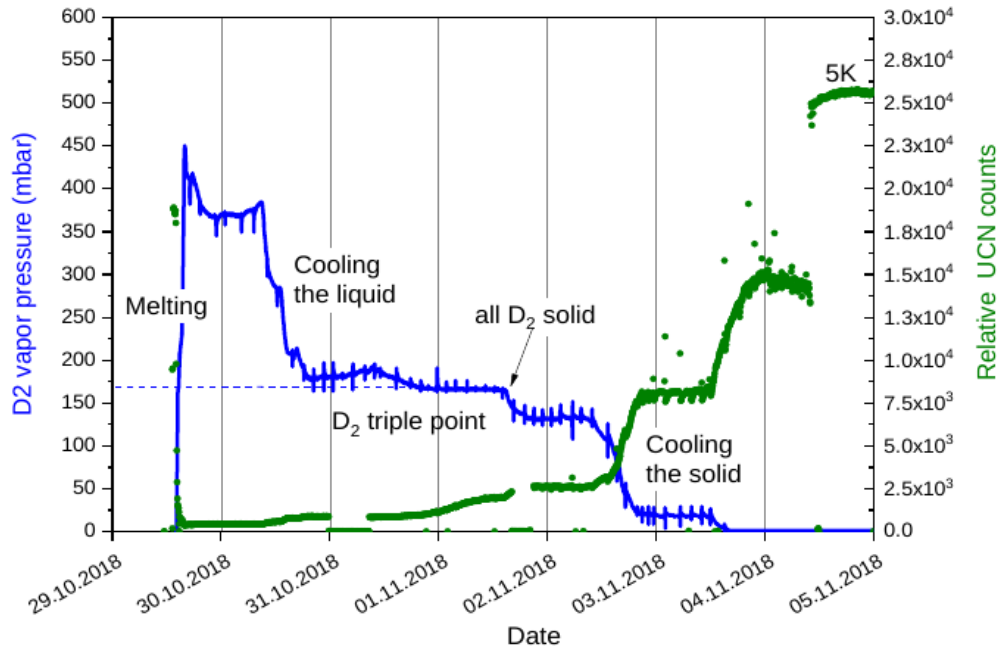


Fig. 1.19: The observed behavior during the slow freezing of the deuterium. The large increase in UCN output demonstrates the strong reduction in UCN losses within the D₂. Figure taken from [2]

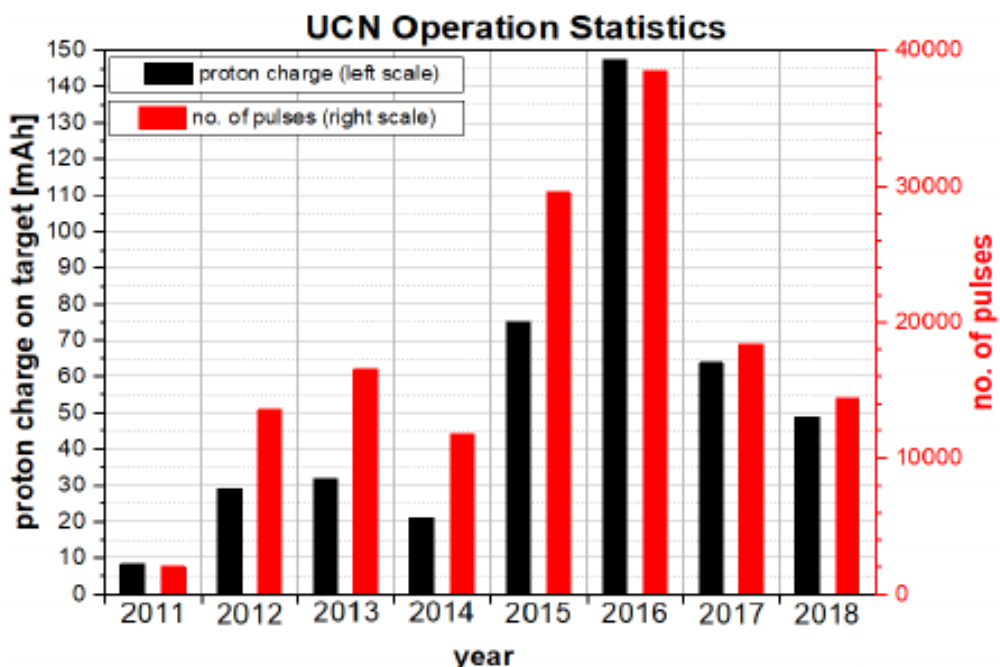


Fig. 1.20: Annual statistics of the UCN source showing total accumulated beam current on target (black bars) and number of beam pulses (red bars) on the UCN spallation target. Figure taken from [2]

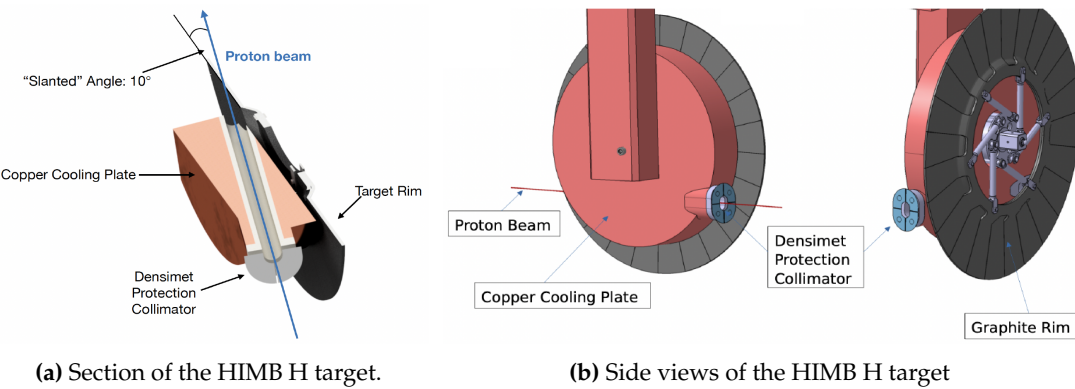


Fig. 1.21: Depiction of the target H for the HIMB project. The slanted target improves the production of surface muons. **a)** The proton beam impinges from the back side passing through a copper water-cooled shielding. **b)** The beam travels lower to avoid the rotating shaft.

the production, collection, and transport of surface muons. HIMB is part of the Isotope and Muon Production using Advanced Cyclotron and Target Technologies project (IMPACT)[[impact](#)].

Production and collection

To increase the surface muon yield, the M target discussed in 1.5.2 will be substituted with target H, having a more slanted geometry. This new target, shown in Fig. 1.21, will be 20 mm thick in the proton direction, with a 10 deg slanting angle: surface muon yields comparable to a 40 mm thick non-slanted target. The protons will impinge below the rotation shaft (Fig. 1.21b), from the back of the target, in a copper water-cooled shielding (Fig. 1.21a). The target will fit in the remote-controlled exchange flask of target E for easier handling and maintenance.

When using solenoids to capture particles, the target is often completely enclosed in the solenoid aperture. This solution is not viable for HIMB because the proton beam is not stopped in the H target. The proposed solution, shown in Fig. 1.22, is to have two different NC solenoids (~ 0.45 T) sideways to the target.

The particles produced by the impact of the 590 MeV proton beam are: electrons, muons and pions. The momentum spectrum of the generated particle is shown in Fig. 1.23: the peak in the μ^+ spectrum is caused by surface muon production while, at higher energies, the muons come from pion decay in flight. This peak is not present for μ^- because stopped π^- undergoes nuclear capture and no muons are produced. In a similar fashion, the peak in positron around Michel edge is produced by stopped μ^+ . The HIMB project focuses on surface muons but the optimization are done to accept and transport momenta up to 80 MeV/c, while keeping the focus on 28 MeV/c.

Beamlines

HIMB will introduce two beamlines: MUH2 and MUH3. The peculiarity of these lines is the extensive use of solenoids. Solenoids achieve focus on both axes (wrt. quadrupoles) but usually, their usage is limited by the required magnetic fields. For the momentum of the surface muons ~ 0.45 T are sufficient and achievable with NC solenoids.

The MUH2 beamline is designed to deliver beams to fixed target experiments (e.g. Mu3e). It will be located at the left-hand side of the target station and its most important figure of merit

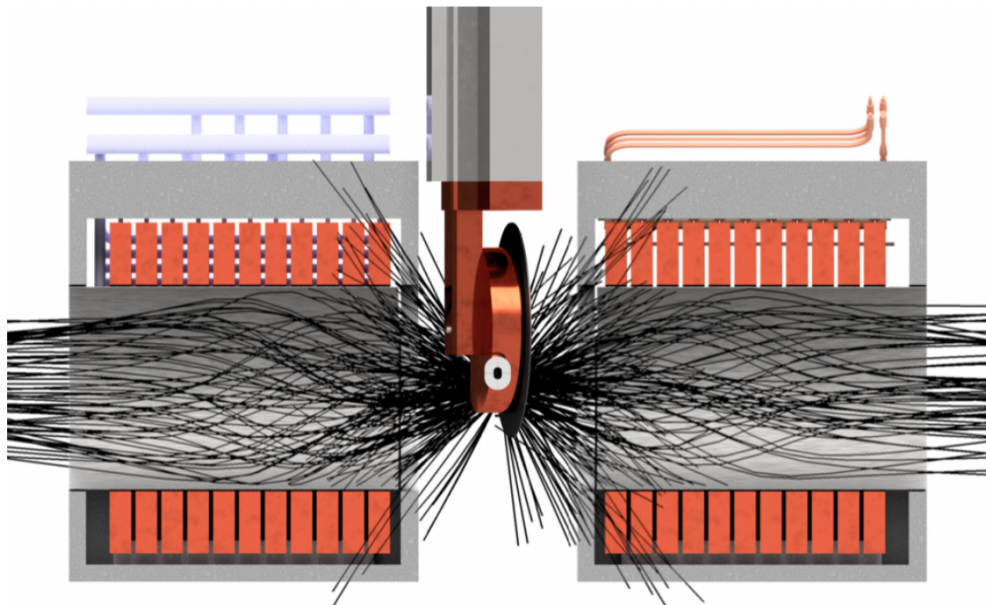


Fig. 1.22: HIMB will have two different NC solenoids sideways to the target. These are required to collect the produced muons and let the surviving proton beam continue toward the spallation SINQ setup.

for MUH2 is transmission. Two 40 deg bends are included in the beam trajectory with dipoles to avoid a direct line of sight to the target.

The model reported in the Conceptual Design Report (CDR) published in January 2022 [10] is able to deliver $1.22 \times 10^{10} \mu^+/\text{s}$ at a proton current of 2.4 mA at the entrance of the experimental area at the surface muon momentum. The beam spot size and the average polarization at the end of the channel are $\sigma_x = 40 \text{ mm}$, $\sigma_y = 42 \text{ mm}$, and $\varepsilon = 0.88$. Interesting to note that a double Wien filter scheme is currently under study to keep the positron contamination under control.

The MUH3 beamline, on the right-hand side of the target station, aims at delivering muon beams for muon spin rotation spectroscopy (μSR). For these applications, $10^{10} \mu/\text{s}$ is not required and part of the beamline follows a more standard approach with quadrupoles. From simulations, while the solenoid section delivers more than $10^{10} \mu/\text{s}$, the rate drops to $3 \times 10^8 \mu/\text{s}$ at 15 MeV and $6 \times 10^6 \mu/\text{s}$ at 10 MeV when reaching the two experimental area. The expected beam spots and polarization are $\sigma_x = 40 \text{ mm}$, $\sigma_y = 42 \text{ mm}$, and $\varepsilon \gtrsim 0.95$.

1.6 Proton Ionization Facility

Another interesting facility at PSI is the Proton Ionization Facility (PIF) [53][54]. This was designed, in conjunction with the European Space Agency, to be a user-friendly testing ground for spacecraft components. The deteriorating effect that high-energy protons can have on semiconductors is a key aspect of the correct functioning of spacecraft in the space environment. Depending on the orbit and the duration of the flight the exposure to this hazard can vary and having reproducible test grounds is cardinal during the design phase. The original goals of this facility:

- Radiation hardness of the new electronic products
- Single Event Upsets (SEU) and Latch-ups (SEL) of electronic components
- Properties of radiation monitors for space and laboratory applications

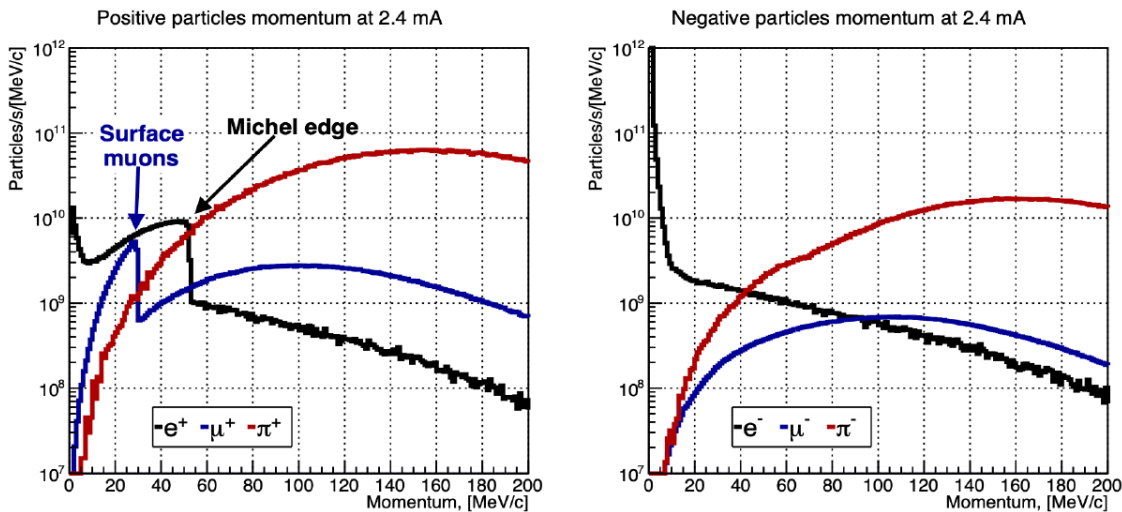


Fig. 1.23: Momentum spectrum for positive and negative e , μ , π produced at the HIMB H target for a proton current of 2.4 mA.

- Basic mechanics of radiation effects in semiconductors
- Space radiation environment by on-earth simulations

Given the broad range of energy and intensities of the facility, alongside ESA many other users apply for beamtime at PIF within the accelerator communities, such as CERN, but also external laboratories, industries, and universities. During the daytime, the beam is usually reserved for biomedical applications and these irradiation studies are done parasitically during the night and on weekends. Although only for a short period, I joined PIF and I had the opportunity to be a shifter. It was quite an interesting experience, allowing me to become acquainted with a different setup and to see a different aspect of the research in particle physics. The usual shift would consist in tuning the beam to be suited to the user's needs and supporting during the data taking.

Bibliography for the introduction

- [1] Lorenzo Calibbi and Giovanni Signorelli. "Charged Lepton Flavour Violation: An Experimental and Theoretical Introduction". In: *Riv. Nuovo Cim.* 41.2 (2018), pp. 71–174. DOI: 10.1393/ncr/i2018-10144-0. arXiv: 1709.00294 [hep-ph].
- [2] Adrian Signer, Klaus Kirch, and Cyrus Hoffman. "Review of Particle Physics at PSI". In: *SciPost Physics Proceedings* (Sept. 2021). DOI: 10.21468/SciPostPhysProc.5.
- [3] Bastiano Vitali. "In situ monitoring of the stopped muon flux at Mu2e". MA thesis. Pisa U., 2020. DOI: 10.2172/1764143.
- [4] M. Raidal et al. "Flavour physics of leptons and dipole moments". In: *Eur. Phys. J. C* 57 (2008). Ed. by R. Fleischer, T. Hurth, and M. L. Mangano, pp. 13–182. DOI: 10.1140/epjc/s10052-008-0715-2. arXiv: 0801.1826 [hep-ph].
- [5] F. J. M. Farley et al. "A New method of measuring electric dipole moments in storage rings". In: *Phys. Rev. Lett.* 93 (2004), p. 052001. DOI: 10.1103/PhysRevLett.93.052001. arXiv: hep-ex/0307006.
- [6] Maxim Pospelov and Adam Ritz. "Electric dipole moments as probes of new physics". In: *Annals of Physics* 318.1 (2005). Special Issue, pp. 119–169. ISSN: 0003-4916. DOI: <https://doi.org/10.1016/j.aop.2005.04.002>. URL: <https://www.sciencedirect.com/science/article/pii/S0003491605000539>.
- [7] A.M. Baldini et al. "Search for the lepton flavour violating decay $\mu^+ \rightarrow e^+ \gamma$ with the full dataset of the MEG experiment". In: *Eur. Phys. J. C* 76.8 (2016), p. 434. DOI: 10.1140/epjc/s10052-016-4271-x. arXiv: 1605.05081 [hep-ex].
- [8] Wilhelm H. Bertl et al. "Search for the Decay $\mu^+ \rightarrow e^+ e^+ e^-$ ". In: *Nucl. Phys. B* 260 (1985), pp. 1–31. DOI: 10.1016/0550-3213(85)90308-6.
- [9] Wilhelm H. Bertl et al. "A Search for muon to electron conversion in muonic gold". In: *Eur. Phys. J. C* 47 (2006), pp. 337–346. DOI: 10.1140/epjc/s2006-02582-x.
- [10] L. Willmann et al. "New bounds from searching for muonium to anti-muonium conversion". In: *Phys. Rev. Lett.* 82 (1999), pp. 49–52. DOI: 10.1103/PhysRevLett.82.49. arXiv: hep-ex/9807011.
- [11] B. Aubert, Y. Karyotakis, et al. "Searches for Lepton Flavor Violation in the Decays $\tau^\pm \rightarrow e \pm \gamma$ and $\tau^\pm \rightarrow \mu^\pm \gamma$ ". In: *Phys. Rev. Lett.* 104 (2 Jan. 2010), p. 021802. DOI: 10.1103/PhysRevLett.104.021802. URL: <https://link.aps.org/doi/10.1103/PhysRevLett.104.021802>.

- [12] K. Hayasaka et al. "Search for Lepton Flavor Violating Tau Decays into Three Leptons with 719 Million Produced Tau+Tau- Pairs". In: *Phys. Lett. B* 687 (2010), pp. 139–143. DOI: 10 . 1016/j.physletb.2010.03.037. arXiv: 1001.3221 [hep-ex].
- [13] E. Abouzaid et al. "Search for lepton flavor violating decays of the neutral kaon". In: *Phys. Rev. Lett.* 100 (2008), p. 131803. DOI: 10 . 1103/PhysRevLett . 100 . 131803. arXiv: 0711 . 3472 [hep-ex].
- [14] D. Ambrose et al. "New limit on muon and electron lepton number violation from $K^0(L) \rightarrow \mu\mu e^- e^-$ decay". In: *Phys. Rev. Lett.* 81 (1998), pp. 5734–5737. DOI: 10 . 1103/PhysRevLett . 81 . 5734. arXiv: hep-ex/9811038.
- [15] Aleksey Sher et al. "An Improved upper limit on the decay $K^+ \rightarrow \pi^+ \mu^+ e^-$ ". In: *Phys. Rev. D* 72 (2005), p. 012005. DOI: 10 . 1103/PhysRevD . 72 . 012005. arXiv: hep-ex/0502020.
- [16] Georges Aad et al. "Search for the lepton flavor violating decay $Z \rightarrow e\mu$ in pp collisions at \sqrt{s} TeV with the ATLAS detector". In: *Phys. Rev. D* 90.7 (2014), p. 072010. DOI: 10 . 1103 / PhysRevD . 90 . 072010. arXiv: 1408 . 5774 [hep-ex].
- [17] R. Akers et al. "A Search for lepton flavor violating Z^0 decays". In: *Z. Phys. C* 67 (1995) () .
- [18] Wilhelm H. Bertl et al. "A Search for muon to electron conversion in muonic gold". In: *Eur. Phys. J. C* 47 (2006), pp. 337–346. DOI: 10 . 1140/epjc/s2006-02582-x.
- [19] A.M. Baldini et al. "MEG Upgrade Proposal". In: (Jan. 2013). arXiv: 1301 . 7225 [physics.ins-det].
- [20] A.M. Baldini et al. "The design of the MEG II experiment". In: *Eur. Phys. J. C* 78.5 (2018), p. 380. DOI: 10 . 1140/epjc/s10052-018-5845-6. arXiv: 1801 . 04688 [physics.ins-det].
- [21] Angela Papa. "Towards a new generation of Charged Lepton Flavour Violation searches at the Paul Scherrer Institut: The MEG upgrade and the Mu3e experiment". In: *EPJ Web Conf.* 234 (2020). Ed. by G. D'Ambrosio et al., p. 01011. DOI: 10 . 1051/epjconf/202023401011.
- [22] Niklaus Berger. "The Mu3e Experiment". In: *Nucl. Phys. B Proc. Suppl.* 248-250 (2014). Ed. by Francesco Grancagnolo and Marco Panareo, pp. 35–40. DOI: 10 . 1016/j.nuclphysbps . 2014 . 02 . 007.
- [23] Ann-Kathrin Perrevoort. "Status of the Mu3e Experiment at PSI". In: *EPJ Web Conf.* 118 (2016). Ed. by G. D'Ambrosio et al., p. 01028. DOI: 10 . 1051/epjconf/201611801028. arXiv: 1605 . 02906 [physics.ins-det].
- [24] R.M. Carey et al. "Proposal to search for $\mu^- N \rightarrow e^- N$ with a single event sensitivity below 10^{-16} ". In: (Oct. 2008). DOI: 10 . 2172/952028.
- [25] L. Bartoszek et al. "Mu2e Technical Design Report". In: (Oct. 2014). DOI: 10 . 2172/1172555. arXiv: 1501 . 05241 [physics.ins-det].
- [26] Y.G. Cui et al. "Conceptual design report for experimental search for lepton flavor violating mu- - e- conversion at sensitivity of $10^{**(-16)}$ with a slow-extracted bunched proton beam (COMET)". In: (June 2009).
- [27] R. Akhmetshin et al. "Letter of Intent for Phase-I of the COMET Experiment at J-PARC". In: (). URL: http://192.153.106.200/researcher/Hadron/en/pac_1203/pdf/COMET-PhaseI-LoI.pdf.

- [28] R. Akhmetshin et al. "Experimental Proposal for Phase-I of the COMET Experiment at J-PARC." In: (). URL: https://j-parc.jp/researcher/Hadron/en/pac_1207/pdf/E21_2012-10.pdf.
- [29] R. Abramishvili et al. "COMET Phase-I Technical Design Report". In: *PTEP* 2020.3 (2020), p. 033C01. DOI: 10.1093/ptep/ptz125. arXiv: 1812.09018 [physics.ins-det].
- [30] Marco Chiappini. "The construction and commissioning of the ultra low mass MEG II drift chamber for the search of the $\mu^+ \rightarrow e^+ \gamma$ decay at branching ratios below 10^{-13} ". PhD thesis. Pisa U., 2019.
- [31] A. Blondel et al. "Research Proposal for an Experiment to Search for the Decay $\mu \rightarrow eee$ ". In: (Jan. 2013). arXiv: 1301.6113 [physics.ins-det].
- [32] F. Abusalma et al. "Expression of Interest for Evolution of the Mu2e Experiment". In: (Feb. 2018). arXiv: 1802.02599 [physics.ins-det].
- [33] David Neuffer. "Mu2e-II Injection from PIP-II". In: (Apr. 2018). DOI: 10.2172/1437287.
- [34] M.G. Catanesi et al. "Large-angle production of charged pions with 3-12.9-GeV/c incident protons on nuclear targets". In: *Phys. Rev. C* 77 (2008), p. 055207. DOI: 10.1103/PhysRevC.77.055207. arXiv: 0805.2871 [hep-ex].
- [35] Andrew Williams John Edmonds. "An Estimate of the Hadron Production Uncertainty and a Measurement of the Rate of Proton Emission after Nuclear Muon Capture for the COMET Experiment". PhD thesis. U. Coll. London, 2015.
- [36] Benjamin Edward Krikler. "Update on the AlCap Experiment". In: *17th International Workshop on Neutrino Factories and Future Neutrino Facilities*. 2015, pp. 408–417.
- [37] Andrew Edmonds. "Latest Updates from the AlCap Experiment". In: *13th Conference on the Intersections of Particle and Nuclear Physics*. Sept. 2018. arXiv: 1809.10122 [physics.ins-det].
- [38] C. Abel et al. "Measurement of the Permanent Electric Dipole Moment of the Neutron". In: *Phys. Rev. Lett.* 124 (8 Feb. 2020), p. 081803. DOI: 10.1103/PhysRevLett.124.081803. URL: <https://link.aps.org/doi/10.1103/PhysRevLett.124.081803>.
- [39] V. Andreev et al. "Improved limit on the electric dipole moment of the electron". In: *Nature* 562.7727 (2018), pp. 355–360. DOI: 10.1038/s41586-018-0599-8.
- [40] Yohei Ema, Ting Gao, and Maxim Pospelov. "Improved Indirect Limits on Muon Electric Dipole Moment". In: *Phys. Rev. Lett.* 128.13 (2022), p. 131803. DOI: 10.1103/PhysRevLett.128.131803. arXiv: 2108.05398 [hep-ph].
- [41] G. W. Bennett et al. "An Improved Limit on the Muon Electric Dipole Moment". In: *Phys. Rev. D* 80 (2009), p. 052008. DOI: 10.1103/PhysRevD.80.052008. arXiv: 0811.1207 [hep-ex].
- [42] N. J. Ayres et al. "The design of the n2EDM experiment". In: *The European Physical Journal C* 81.6 (June 2021). DOI: 10.1140/epjc/s10052-021-09298-z. URL: <https://doi.org/10.1140/epjc/s10052-021-09298-z>.
- [43] Norman F. Ramsey. "A Molecular Beam Resonance Method with Separated Oscillating Fields". In: *Phys. Rev.* 78 (6 June 1950), pp. 695–699. DOI: 10.1103/PhysRev.78.695. URL: <https://link.aps.org/doi/10.1103/PhysRev.78.695>.

- [44] S. Eckel, A. O. Sushkov, and S. K. Lamoreaux. "Limit on the Electron Electric Dipole Moment Using Paramagnetic Ferroelectric $\text{Eu}_{0.5}\text{Ba}_{0.5}\text{TiO}_3$ ". In: *Phys. Rev. Lett.* 109 (19 Nov. 2012), p. 193003. DOI: 10.1103/PhysRevLett.109.193003. URL: <https://link.aps.org/doi/10.1103/PhysRevLett.109.193003>.
- [45] Y. J. Kim et al. "New Experimental Limit on the Electric Dipole Moment of the Electron in a Paramagnetic Insulator". In: *Phys. Rev. D* 91.10 (2015), p. 102004. DOI: 10.1103/PhysRevD.91.102004. arXiv: 1104.4391 [nucl-ex].
- [46] V. V. Flambaum, I. B. Khriplovich, and O. P. Sushkov. "On the Possibility to Study P Odd and T Odd Nuclear Forces in Atomic and Molecular Experiments". In: *Sov. Phys. JETP* 60 (1984), p. 873.
- [47] M. M. Gordon. "The longitudinal space charge effect and energy resolution". In: *Conf. Proc. C* 690917 (1969), pp. 305–317.
- [48] E. Pozdnyev et al. "Longitudinal beam dynamics studies with space charge in small isochronous ring". In: *Phys. Rev. ST Accel. Beams* 12 (2009), p. 054202. DOI: 10.1103/PhysRevSTAB.12.054202.
- [49] C. Baumgarten. "Transverse-Longitudinal Coupling by Space Charge in Cyclotrons". In: *Phys. Rev. ST Accel. Beams* 14 (2011), p. 114201. DOI: 10.1103/PhysRevSTAB.14.114201. arXiv: 1109.1996 [physics.acc-ph].
- [50] W. Joho. "High Intensity Problems in Cyclotrons". In: *9th International Conference on Cyclotrons and their Applications*. 1982, EI03.
- [51] M. Aiba et al. "Science Case for the new High-Intensity Muon Beams HIMB at PSI". In: (Nov. 2021). arXiv: 2111.05788 [hep-ex].
- [52] Giovanni Dal Maso et al. "Future facilities at PSI, the High-Intensity Muon Beams (HIMB) project". In: *EPJ Web Conf.* 282 (2023), p. 01012. DOI: 10.1051/epjconf/202328201012.
- [53] Wojtek Hajdas et al. "The Proton Irradiation Facility at the Paul Scherrer Institute". In: *Nuclear Instruments and Methods in Physics Research Section B: Beam Interactions with Materials and Atoms* 113.1 (1996). Accelerators in Applied Research and Technology, pp. 54–58. ISSN: 0168-583X. DOI: [https://doi.org/10.1016/0168-583X\(95\)01327-X](https://doi.org/10.1016/0168-583X(95)01327-X). URL: <https://www.sciencedirect.com/science/article/pii/0168583X9501327X>.
- [54] Wojtek Hajdas et al. "Proton Irradiation Facility and Space Radiation Monitoring at the Paul Scherrer Institute". In: *Physica medica : PM : an international journal devoted to the applications of physics to medicine and biology : official journal of the Italian Association of Biomedical Physics (AIFB)* 17 Suppl 1 (Feb. 2001), pp. 119–23.

Part I

muEDM

Chapter 2

muEDM

This chapter is an introduction to the muEDM experiment. After describing in some detail the spin dynamics, a reminder on the EDM searches for the different particles will follow. We will then outline the measuring principle of the experiment, the frozen spin technique, and deep dive into the current status of the experiment. The study of systematic uncertainties will close this chapter. As always, the early stage of the experiment means the rate of changes and improvement is outstanding. This my attempt to an up-to-date description but some details might be already outdated.

2.1 Electric Dipole Moment

As introduced in 1.3.5, the Hamiltonian describing the spin dynamics is:

$$\hat{H} = -\mu \hat{\sigma} \cdot \mathbf{B} - d \hat{\sigma} \cdot \mathbf{E}$$

We then saw that, when considering a combination of magnetic and electric fields and a moving particle it is useful to introduce the polarization vector $\boldsymbol{\Pi} = \mathbf{s}/s$ and the Thomas precession $\boldsymbol{\Omega}_0$:

$$\frac{d\boldsymbol{\Pi}}{dt} = \boldsymbol{\Omega}_0 \times \boldsymbol{\Pi}, \quad \boldsymbol{\Omega}_0 = -\frac{e}{m\gamma} \left[(1 + \gamma a) \mathbf{B} - \frac{a\gamma^2}{\gamma + 1} (\boldsymbol{\beta} \cdot \mathbf{B}) \boldsymbol{\beta} - \gamma \left(a + \frac{1}{\gamma + 1} \right) \frac{\boldsymbol{\beta} \times \mathbf{E}}{c} \right]$$

With no electrical field parallel to the momentum and with $\boldsymbol{\Omega}_c$ the cyclotron frequency, the relative spin precession of a muon in a storage ring is described by (T-BMT [**miss-59**]):

$$\begin{aligned} \boldsymbol{\Omega} = \boldsymbol{\Omega}_0 - \boldsymbol{\Omega}_c &= \underbrace{\frac{q}{m} \left[a \mathbf{B} - \frac{a\gamma}{\gamma + 1} (\boldsymbol{\beta} \cdot \mathbf{B}) \boldsymbol{\beta} - \left(a + \frac{1}{1 - \gamma^2} \right) \frac{\boldsymbol{\beta} \times \mathbf{E}}{c} \right]}_{\text{Anomalous precession, } \omega_a = \omega_L - \omega_c} \\ &\quad + \underbrace{\frac{\eta q}{2m} \left[\boldsymbol{\beta} \times \mathbf{B} + \frac{\mathbf{E}}{c} - \frac{\gamma c}{\gamma + 1} (\boldsymbol{\beta} \cdot \mathbf{E}) \boldsymbol{\beta} \right]}_{\text{Interaction of EDM and relativistic } \mathbf{E}, \omega_a} \end{aligned} \quad (2.1)$$

The second term describes the precession due to the EDM coupling to the relativistic \mathbf{E} , perpendicular to the \mathbf{B} in which the particle is moving. In the presence of a muon EDM the plane would be tilted and a vertical precession ($\omega_e \perp \mathbf{B}$), shifted by $\pi/2$ to the horizontal anomalous precession, would become observable.

2.1.1 Symmetry violation

In physics, there are three cardinal discrete symmetries: Charge (C), Parity (P), and Time (T). P and T are related to the invariance under spatial and temporal reversal while C is the invariance for particle \leftrightarrow antiparticle exchange. While the magnetic field and the spin are *pseudo*-vectors under P and vectors under T, the electric field behaves in the opposite way. The implication of this difference is that EDM and MDM behave differently under C, P, and T:

$$MDM : \begin{cases} P(-\mu\hat{\sigma} \cdot B) = -\mu P(\hat{\sigma}) \cdot P(B) = -\mu(+\hat{\sigma}) \cdot (+B) = -\mu\hat{\sigma} \cdot B \\ T(-\mu\hat{\sigma} \cdot B) = -\mu T(\hat{\sigma}) \cdot T(B) = -\mu(-\hat{\sigma}) \cdot (-B) = -\mu\hat{\sigma} \cdot B \end{cases} \quad (2.2)$$

$$EDM : \begin{cases} P(-d\hat{\sigma} \cdot E) = -dP(\hat{\sigma}) \cdot P(E) = -d(+\hat{\sigma}) \cdot (-E) = +d\hat{\sigma} \cdot E \\ T(-d\hat{\sigma} \cdot E) = -dT(\hat{\sigma}) \cdot T(E) = -d(-\hat{\sigma}) \cdot (+E) = +d\hat{\sigma} \cdot E \end{cases} \quad (2.3)$$

In light of the CPT theorem, the breaking of the T symmetry implies the breaking of CP.

2.1.2 Current limits on EDM

As discussed in 1.4.2, the last decades saw a continuous effort to measure the EDM of different particles. There the experiments setting the current limits were discussed but we report in Tab. 2.1 the results to aid the reader. It is important to note there are two limits for μ : one obtained by rescaling the limit on d_e , obtaining an *indirect limit*; one, less stringent, is a *direct limit* (*).

Experiment	Particle	EDM limit in ecm
nEDM [1]	n	0.18×10^{-25}
ACME [2]	e	1.1×10^{-29}
Indirect [3]	μ	$0.19 \times 10^{-19} *$
g-2 [4]	μ	1.8×10^{-19}

Fig. 2.1: Sumary of the current limits on the EDM for neutron electron and muon.

2.1.3 The *frozen spin* technique

As illustrated in [1, 9], with the appropriate choice of electric field and having p , B and E forming an orthogonal basis, the anomalous precession term in eq. 2.1 can be set to zero.

$$aB = \left(a - \frac{1}{\gamma^2 - 1} \right) \frac{\beta \times E}{c} \quad (2.4)$$

In this situation the relative angle between p and spin remains unchanged if $\eta = 0$, hence 'frozen'. In the presence of an EDM the change in polarization would then follow

$$\frac{d\Pi}{dt} = \omega_e \times \Pi, \quad \omega_e = \frac{\eta q}{2m} \left(\beta \times B + \frac{E_f}{c} \right) = \frac{2d_\mu}{\hbar} (\beta c \times B + E_f) \quad (2.5)$$

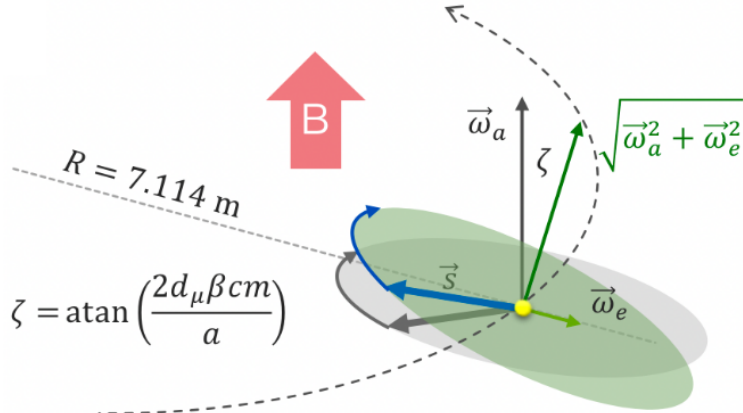


Fig. 2.1

The net result of the EDM is then a vertical build-up of the polarization given by Eq. 2.6 and illustrated by the sketch in Fig. 2.1.

$$|\Pi(t)| = P(t) = P_0 \sin(\omega_e t) \approx P_0 \omega_e t \approx 2P_0 \frac{d_\mu}{\hbar} \frac{E_f}{a\gamma^2} t \quad (2.6)$$

At this point, we would like to evaluate the sensitivity to this vertical build-up and this is dependent on the experimental setup investigated.

$$\frac{dP}{dd_\mu} = \frac{2P_0 E_f t}{a\hbar\gamma^2} \quad (2.7)$$

$$\sigma(d_\mu) = \frac{a\hbar\gamma}{2P_0 E_f \sqrt{N} \tau_\mu A} \quad (2.8)$$

2.2 The muEDM experiment

2.3 The precursor

The task at hand is quite complex and for this reason, the aim is to first have a working prototype to demonstrate the measuring principles, the achieved control on the different sources of uncertainties and the correct working of the different subdetectors.

2.3.1 Superconducting injection channel

To allow the incoming muons to enter the magnet without being reflected or deviated by fringing fields an injection channel is needed. For reasons that will be discussed in the section dedicated to the systematics (see Sec. 2.4), we will actually require two symmetrical injections. The idea is to use a superconducting pipe: the fields around the pipe will generate Eddy currents which will, in turn, generate an opposite field inside the pipe, canceling the first. Clearly, the development of such a system is not trivial, and a precise study of the different shapes and materials is required. The hope would be to find a suitable *high-temperature* superconductor.

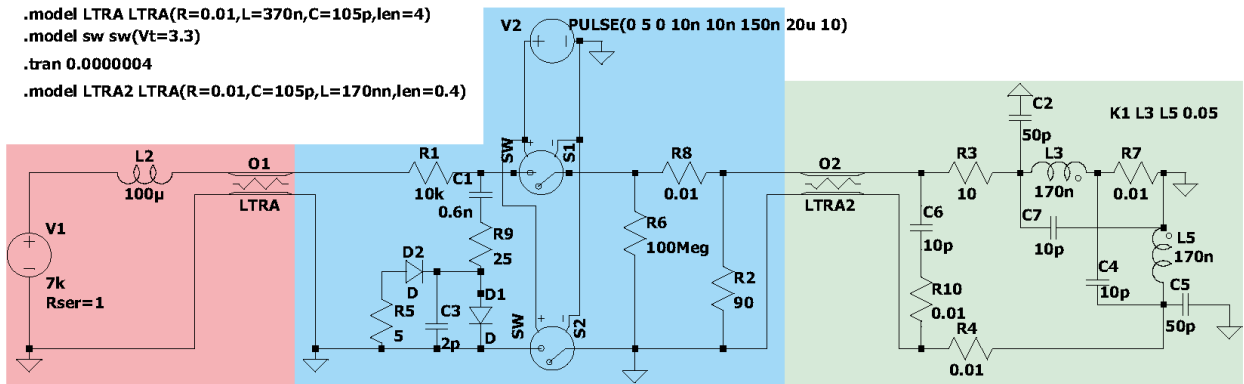


Fig. 2.2: LTSPICE simulation for the kicker circuit.

2.3.2 Entrance detector

After a muon successfully enters the experiment it would spiral to the other side of the magnet. To store it a magnetic kick is necessary. How to produce this kick is going to be discussed in the next section but in either case, this system needs to be triggered. To detect the muon entering the system a thin scintillator can be used. This needs to be thick enough to produce sufficient light but thin enough not to deflect the particle from the design orbit. With a dedicated GEANT4 simulation¹, the amount of light exiting the different sides of the thin scintillator was studied as a function of the muon momentum. The results of the simulations and the dedicated beamtimes to develop this entrance detector will be discussed in Ch. 3, dedicated to this detector.

2.3.3 Muon tracking

Although during physics runs it is important to minimize the number of interactions of the muon along the path, it is a cardinal step to prove the muons are following the correct path. For this reason, a removable muon-tracking device is under development. The idea is to use TPC + GRID-PIX.

Beamtime A prototype of this detector was developed and tested in 2022, the results have been published and can be found in [5]. The setup was quite simple: the beam was centered through the TPC and scintillators were used as an external trigger. During this testing, the detector was tested at different pressures and voltages, and with different mixtures of gas.

2.3.4 Kicker

The prerequisite for the *frozen spin* is to first store the muon around the design orbit. This is achieved by applying a longitudinal kick, canceling the momentum component parallel to the magnetic field. The development of this element is non-trivial because of the stringent requirements on the strength, time scale, and residual effects of the kick. We started by looking into different shapes and types of coil as well as developing LTSPICE simulations of the generating circuit. The current version of the circuit is shown in Fig. 2.2.

¹To be honest this was actually my first GEANT4 project and *few iterations* were needed.

2.3.5 Electrodes

After the muon has been successfully stored around the design orbit the next step is to apply a radial electric field. The strength of this field is going to modify the frequency of the $g-2$ precession, eventually *freezing* the spin (eq. 2.5) along the momentum direction. These electrodes need to be out of the muon orbit and with a minimal material budget to reduce the positron scattering. Dedicated simulations and prototyping have been developed also for this element.

2.3.6 Positron tracking

The development of the positron tracker has been a big part of my work in the collaboration. For this reason, an in-depth description will follow in a dedicated chapter (see Ch. 4) while here we will just outline the basic idea. The project is to use two subsystems:

- A silicon pixel external tracker will be used to track precisely the transverse position of the positron. The aim of this sub-detector is to measure the $g-2$ precession to fine-tune the radial electric field to achieve the frozen-spin condition. A straw-tube-based alternative design for this sub-detector is also under study.
- An internal scintillating fiber detector (with comparable resolution on the transverse position) will complement the silicon pixel with additional hits. The requirement is to have a better resolution on the longitudinal position of the hits to measure the EDM by looking at the pitch of the outgoing helical track. I dedicated most of my effort to this sub-detector.

2.4 Systematics

[6] [muEDM:g-2:2008] [7] [8] [9] [10] [11] [12]

2.5 Schedule

As we just saw, although the development of the precursor is moving at a very nice speed, the tasks are very challenging. To put in perspective the current understanding of the different challenges and time constraints, we add here the schedule that was included in the proposal of the experiment in 2022. Fig. 2.3 is a schedule on the short period up to the long shut-down, in which 6 main milestones are highlighted:

- 1 Demonstration of off-axis injection
- 2 Muon selection and generation of trigger
- 3 Generation of the pulsed magnetic field and measurement of eddy-currents
- 4 Stopping of muons and detection of ($g - 2$) precession
- 5 Adjusting the electric field by tuning ($g - 2$) precession to zero
- 6 Data-taking in muon EDM mode

Fig. 2.4 goes beyond the long shut-down and covers the full life of the experiment, up to 2033.

2.6 Conclusions

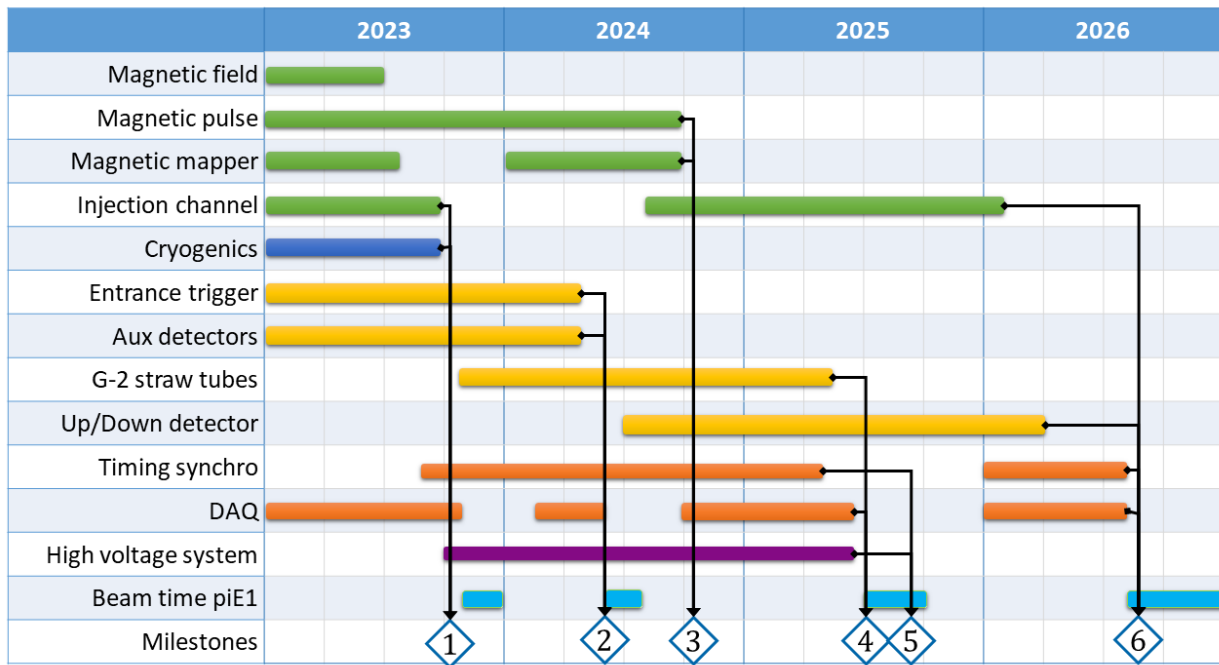


Fig. 2.3: ‘Short’ term muEDM schedule, with highlighted the 6 main milestones up to the *long shutdown*. Milestones: 1) off-axis injection; 2) generation of the entrance trigger; 3) generation of the pulsed B field; 4) detection of $g - 2$; 5) adjust $g - 2$ to zero; 6) EDM data taking.

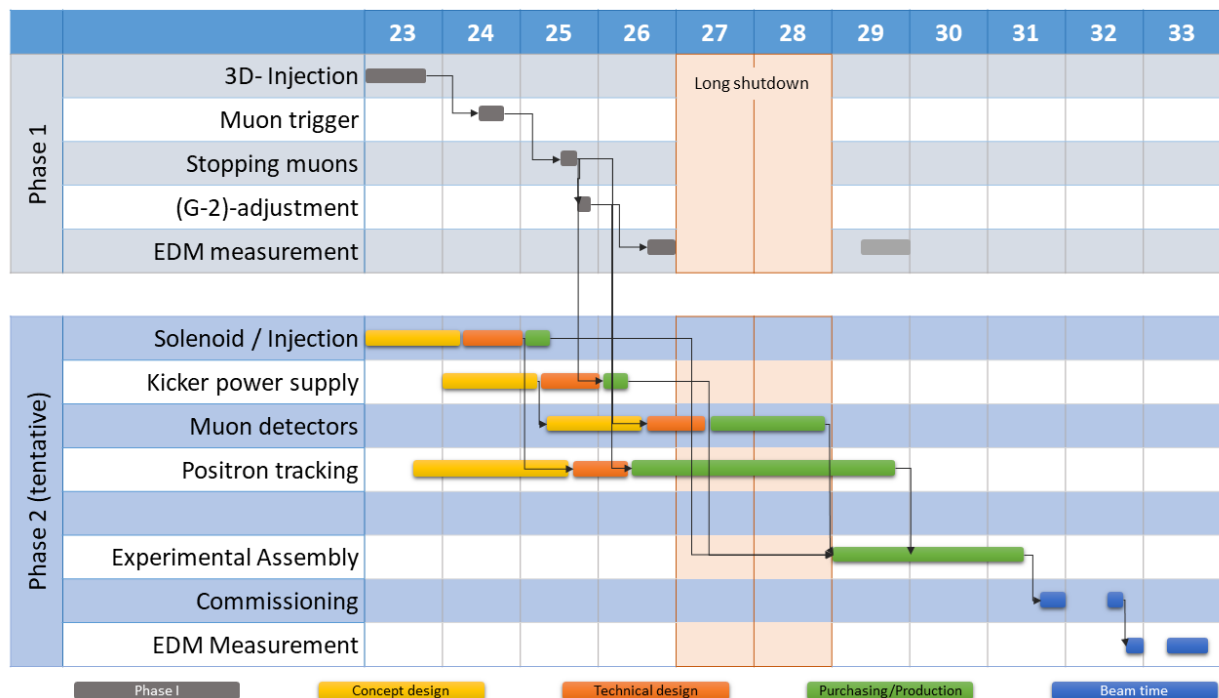


Fig. 2.4: ‘Long’ term muEDM schedule, with the different phases up to the end of the experiment.

Bibliography on muEDM

- [1] C. Abel et al. "Measurement of the Permanent Electric Dipole Moment of the Neutron". In: *Phys. Rev. Lett.* 124 (8 Feb. 2020), p. 081803. DOI: 10.1103/PhysRevLett.124.081803. URL: <https://link.aps.org/doi/10.1103/PhysRevLett.124.081803>.
- [2] V. Andreev et al. "Improved limit on the electric dipole moment of the electron". In: *Nature* 562.7727 (2018), pp. 355–360. DOI: 10.1038/s41586-018-0599-8.
- [3] Yohei Ema, Ting Gao, and Maxim Pospelov. "Improved Indirect Limits on Muon Electric Dipole Moment". In: *Phys. Rev. Lett.* 128.13 (2022), p. 131803. DOI: 10.1103/PhysRevLett.128.131803. arXiv: 2108.05398 [hep-ph].
- [4] G. W. Bennett et al. "An Improved Limit on the Muon Electric Dipole Moment". In: *Phys. Rev. D* 80 (2009), p. 052008. DOI: 10.1103/PhysRevD.80.052008. arXiv: 0811.1207 [hep-ex].
- [5] G. Cavoto et al. "Operating the GridPix detector with helium-isobutane gas mixtures for a high-precision, low-mass Time Projection Chamber". In: (May 2023). arXiv: 2305.03599 [physics.ins-det].
- [6] Yannis K. Semertzidis et al. "A sensitive search for a muon electric dipole moment". In: *AIP Conf. Proc.* 564.1 (2001). Ed. by G. Cantatore, pp. 263–268. DOI: 10.1063/1.1374993.
- [7] A. Adelmann et al. "Compact storage ring to search for the muon electric dipole moment". In: *J. Phys. G* 37 (2010), p. 085001. DOI: 10.1088/0954-3899/37/8/085001.
- [8] Hiromi Iinuma. "New approach to the muon g-2 and EDM experiment at J-PARC". In: *J. Phys. Conf. Ser.* 295 (2011). Ed. by Hans Stroher and Frank Rathmann, p. 012032. DOI: 10.1088/1742-6596/295/1/012032.
- [9] Hiromi Iinuma et al. "Three-dimensional spiral injection scheme for the g-2/EDM experiment at J-PARC". In: *Nucl. Instrum. Meth. A* 832 (2016), pp. 51–62. DOI: 10.1016/j.nima.2016.05.126.
- [10] A. Adelmann et al. "Search for a muon EDM using the frozen-spin technique". In: (Feb. 2021). arXiv: 2102.08838 [hep-ex].
- [11] Mikio Sakurai et al. "muEDM: Towards a search for the muon electric dipole moment at PSI using the frozen-spin technique". In: *24th International Symposium on Spin Physics*. Jan. 2022. arXiv: 2201.06561 [hep-ex].
- [12] Kim Siang Khaw et al. "Search for the muon electric dipole moment using frozen-spin technique at PSI". In: *PoS NuFact2021* (2022), p. 136. DOI: 10.22323/1.402.0136. arXiv: 2201.08729 [hep-ex].

Chapter 3

muEDM entrance detector

In the previous chapter, the muEDM experiment was introduced and the current status was described. In this, we will describe the simulations and beamtimes connected to the entrance detector of the experiment. We will start with the GEANT4 simulations of thin and thick scintillators, moving then to the entrance detector and the ‘telescope’ used in the beamtime of 2022. We will then move through the beamtimes.

3.1 Short intro to scintillators

A scintillator is any material that emits light (visible or ultraviolet) when exposed to ionizing radiation, like high-energy photons or charged particles. The main distinction is between organic and inorganic scintillators:

- Organic scintillators are typically composed of carbon, hydrogen, and other organic (carbon-based) compounds. These materials often include fluorescent dyes or organic molecules that emit light when excited by ionizing radiation. They are often used for neutron detection and can also be used for other types of radiation, such as alpha and beta particles. They are versatile and find applications in various fields, including nuclear and particle physics
- Inorganic scintillators are composed of inorganic materials that do not primarily contain carbon-hydrogen (C-H) bonds. These materials can include compounds like sodium iodide ($\text{NaI}(\text{Tl})$), cesium iodide ($\text{CsI}(\text{Tl})$), bismuth germanate ($\text{Bi}_4\text{Ge}_3\text{O}_{12}$ often “BGO”), and lanthanum halides (LaBr_3 and LaCl_3). These are commonly used in applications requiring high energy resolution and efficiency, like in gamma-ray spectroscopy, high-energy physics experiments, or medical imaging.

Organic scintillators typically have relatively fast response times and are less expensive, while inorganic scintillators tend to have better energy resolution. Organic scintillators divide in: liquid, crystalline and plastic. We will discuss plastic scintillators while an example of a liquid scintillator, based on Xenon, will be presented when describing the MEG II apparatus (see Ch.7).

3.1.1 Plastic scintillators

Plastic scintillators are by far the most widely used and their densities range from 1.03 to 1.2 g/cm^3 , with a light yield of $1 \div 100 \gamma/\text{eV}$ of energy deposit [1]. The number of photons emitted is not linear with the energy deposit: in very dense ionization the light yield is lower than expected. This

effect is described with the Birks's formula (Eq. 3.1) for the luminescence \mathcal{L} .

$$\frac{d\mathcal{L}}{dx} = \mathcal{L}_0 \frac{\frac{dE}{dx}}{1 + k \frac{dE}{dx}} \quad (3.1)$$

Where $\frac{d\mathcal{L}}{dx}$ is the Light output, $\frac{dE}{dx}$ the energy loss per unit length by ionizing radiation and k Birks' constant (also known as the stopping power ratio).

Plastic scintillators are widely used in particle detectors due to their high light yield and fast response time, enabling sub-nanosecond timing resolution. They offer the advantage of pulse shape discrimination, allowing for particle identification based on emitted light during the decay "tail," particularly sensitive to proton recoils from neutrons due to their hydrogen content.

These scintillators are popular due to their ease of fabrication into various shapes and cost-effectiveness. Scintillating fibers made from plastic scintillators are commonly used in tracking and calorimetry applications.

3.1.2 Scintillation process

Charged particles passing through matter create excited molecules, some of which release about 3% of their energy as optical photons through a process known as scintillation. This phenomenon is prominent in organic substances containing aromatic rings like polystyrene (PS) and polyvinyl-toluene (PVT), as well as in liquids such as toluene, xylene, and pseudocumene.

In fluorescence, molecules are initially excited by absorbing a photon and then deexcite by emitting a longer wavelength photon. To shift scintillation light to a more convenient wavelength, fluorescent materials, or "fluors," are used as "wavelength shifters." However, complex molecules in fluorescence can exhibit self-absorption, which shortens the attenuation length. The greater the Stokes' shift (the difference between absorption and emission wavelengths), the less self-absorption occurs, making a larger Stokes' shift desirable for fluors.

In high-energy physics, plastic scintillators are typically composed of selected fluors dissolved in a plastic base containing aromatic rings. Most plastic scintillators use either PVT or PS as their base, with PVT-based scintillators being up to 50% brighter. Adding a "primary" fluor in high concentration (1% by weight) into the base helps improve the attenuation length, as it efficiently re-radiates absorbed energy at wavelengths where the base is more transparent.

The primary fluor also plays a crucial role in shortening the scintillator's decay time, increasing the total light yield. The strong coupling between the base and fluor, known as Foerster resonance energy transfer, occurs at short distances, enhancing the speed and light yield of plastic scintillators.

In some cases, when the selected fluor doesn't meet all requirements, a "secondary" fluor may be added in fractional percent levels, and occasionally even a third.

External wavelength shifters are employed to aid light collection in complex geometries. They consist of a lightpipe with a wave-shifting fluor dissolved in a non-scintillating base. Typically, an acrylic base is used for its optical qualities, along with a single fluor to shift the emitted light to the blue-green range. These shifters also contain additives to absorb ultraviolet light and reduce sensitivity to Cherenkov radiation.

For specialized applications, scintillators with increased radiation resistance or unique prop-

erties like neutron/gamma discrimination can be created by significantly increasing fluor concentrations.

3.1.3 Scintillating Fibers

This is also a good moment to introduce The concept of *scintillating fibres*. We will not use them in this chapter but will be key in Ch. 4, dedicated to the e^+ tracking.

The use of clad optical fibers containing scintillators and wavelength shifters (WLS) has proven highly beneficial. Scintillating fiber (SCIFI) calorimeters, first demonstrated in [45], have become mainstream due to their speed, density, radiation resistance, and impressive resolution akin to lead glass. SCIFI trackers can handle high rates and radiation but require sensitive photodetectors due to low photon yield at the fiber's end.

Control over the sensitive region of scintillating fibers can be achieved by splicing them onto clear, non-scintillating fibers.

Typically, these fibers have a core of polystyrene-based scintillator or WLS (refractive index $n = 1.59$), surrounded by a cladding of PMMA ($n = 1.49$), sometimes with an additional fluorinated PMMA cladding ($n = 1.42$) for enhanced light capture, resulting in a diameter of 0.5 to 1 mm. The capture fraction, representing the proportion of generated light transported down the optical fiber, is around 6% for single-clad fibers and 10% for double-clad fibers. A minimum-ionizing particle traversing a 1 mm diameter fiber perpendicularly generates fewer than 2000 photons, with approximately 200 captured. In a large collider tracker, attenuation may eliminate up to 95% of these photons.

The attenuation length, the distance over which the signal diminishes to $1/e$ of its original value, is influenced by factors such as re-absorption of emitted photons, polymer base crystallinity, photodetector sensitivity, and internal surface quality. High-quality fibers can achieve attenuation lengths of several meters.

3.2 GEANT4 simulations

3.2.1 GEANT4

GEANT4 (GEometry ANd Tracking) is a powerful open-source simulation toolkit used in various scientific fields, primarily for studying the interactions of particles with matter, and is widely employed in particle, nuclear, and medical physics. At its core, GEANT4 works by representing the physical world as a set of geometric shapes and materials. After defining the properties of particles, their energy, and the materials they interact with, GEANT4 simulates their behavior. This toolkit utilizes a range of physics models and algorithms to accurately model particle interactions, including electromagnetic, hadronic, and optical processes. It can simulate particles of various energies, from subatomic to cosmic ray levels. The simulation is *step* based: at every interaction, the physical properties of the particle are updated and, if needed, secondary particles are generated. Steps are forced to end when crossing the boundary between two materials/volumes to ensure proper care is taken in the transition. This is of particular importance for optical simulations, such as the propagation of OpticalPhotons produced by scintillation.

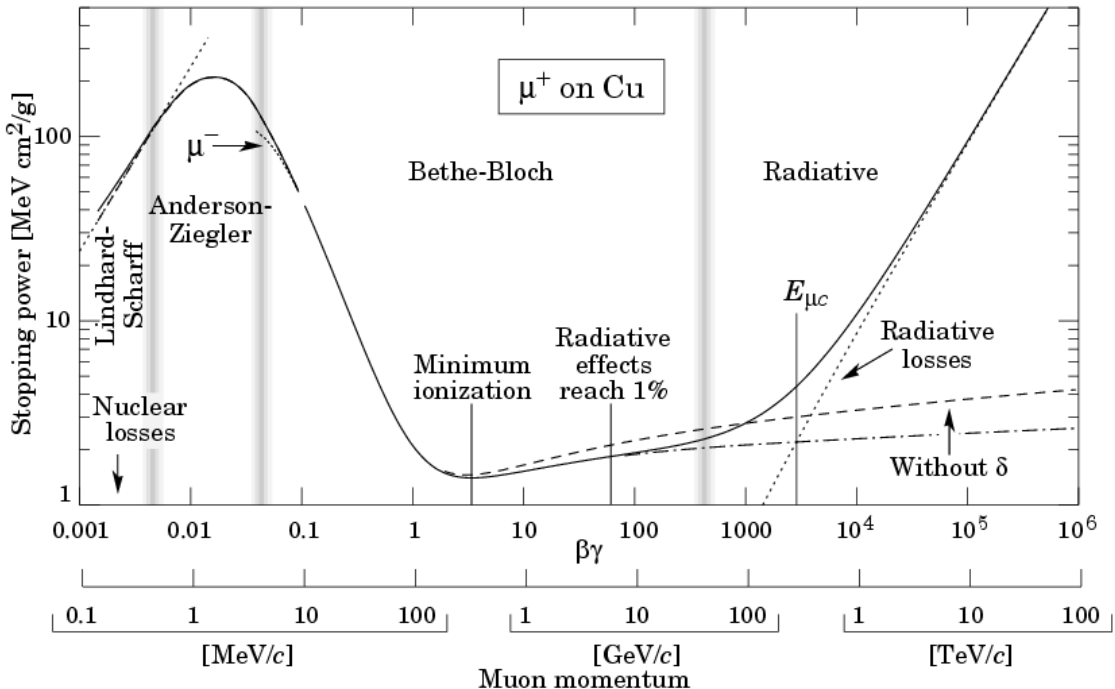


Fig. 3.1: This figure illustrates the Bethe-Bloch formula [1], a vital tool in particle physics, depicting how charged particles lose energy when traversing through matter.

3.2.2 Entrance system

To study the feasibility of the entrance thin scintillator, a GEANT4 simulation was developed. The first step, after achieving a running simulation of scintillation, was to study the range of muons of the interesting momenta, as well as the energy deposit. These first results are shown in Fig. 3.2. Here we can see the energy deposit for e^+ and μ^+ in scintillators of different thicknesses, reflecting the well-known Bethe-Bloch plot shown in Fig. 3.1. Interesting features are:

- The energy deposit is linear with the thickness for the e^+
- The linearity is lost for the μ^+ . First, we have an exponential trend and then a plateau, when $E_{dep} \approx E_k$ and the μ^+ is stopped
- The shape of the deposit slowly changes from Landau to Gaussian

In Fig. 3.3 we recover the linear (and then exponential) trend when sampling the energy deposit for μ^+ for lower thicknesses at both 28 MeV/c and 128 MeV/c.

Multiple scattering

An important sanity check was also to study the multiple scattering in the scintillator. More details on the functional description and the GEANT4 implementation of the multiple scattering will follow, in 3.3. This was done with a fit to the Highland formula (Eq. 3.2) the average value of the scattering angle as a function of the thickness. These fits are shown in Fig. 3.5 and the results, $X_{0,28MeV} = (54.36 \pm 0.17) \text{ gm/cm}^2$ and $X_{0,128MeV} = (54.30 \pm 0.14) \text{ gm/cm}^2$, are consistent with the value for BC400® of $X_0 \sim 50$.

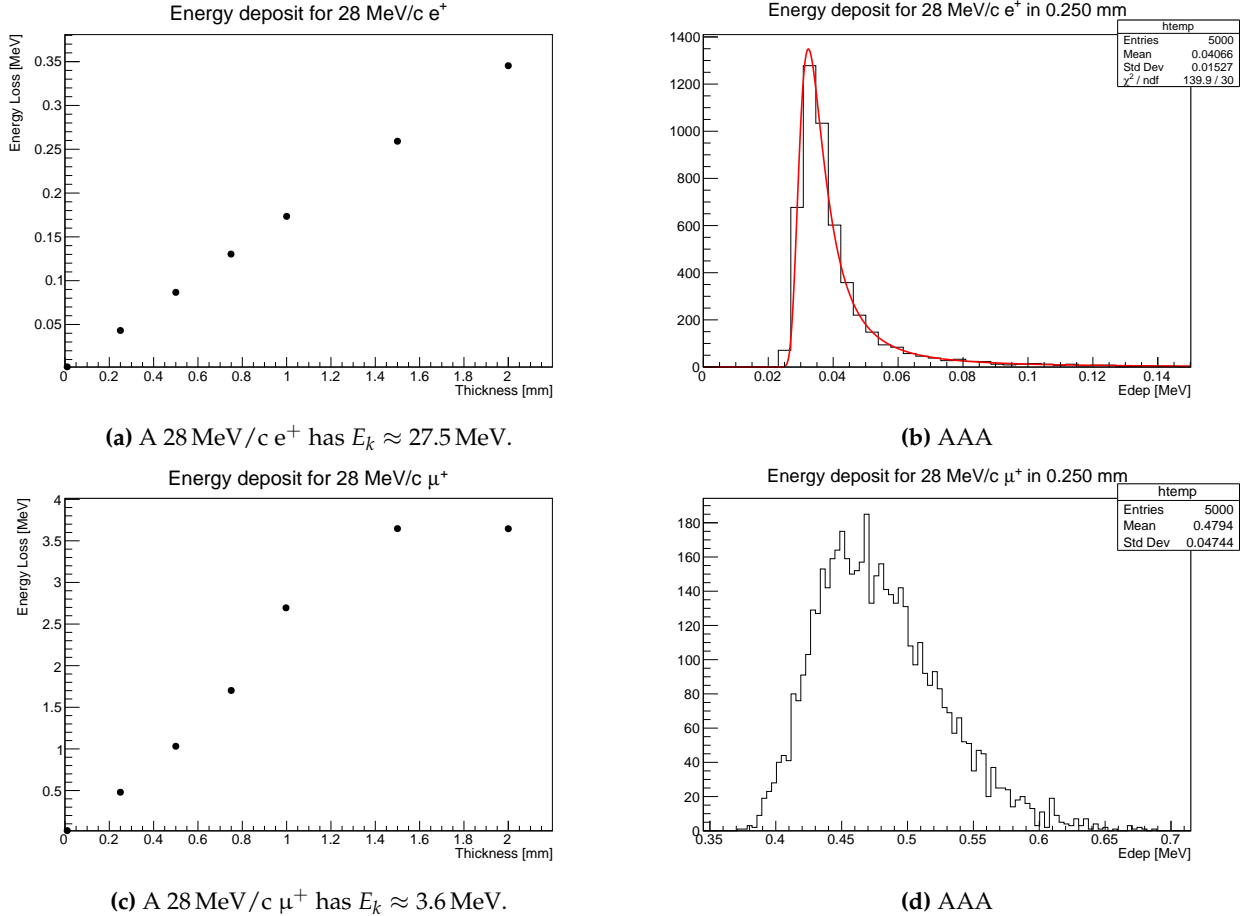


Fig. 3.2: Curve for the average energy deposit in a BC400® scintillator for μ^+ (3.2a) and e^+ (3.2c) at 28 MeV/c. Clearly visible is the linearity of the energy loss for the e^+ with thickness. This linearity is lost for the μ^+ : first, we see an exponential trend and then a plateau when $E_{dep} \approx E_k$ and the μ^+ is stopped. The distribution of the energy deposit slowly transitions from a Landau to a Gaussian: (3.2b) is an example of the first type; (3.2b) is an example of the transition.

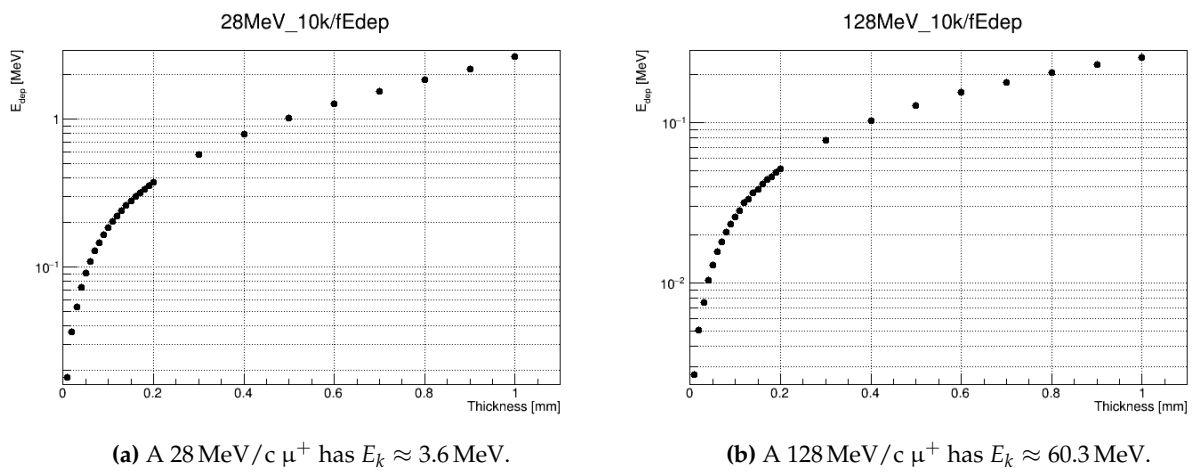


Fig. 3.3: Detail on the lower section of the curve for the average energy deposit in a BC400® scintillator for μ^+ at 28 MeV/c and 128 MeV/c.

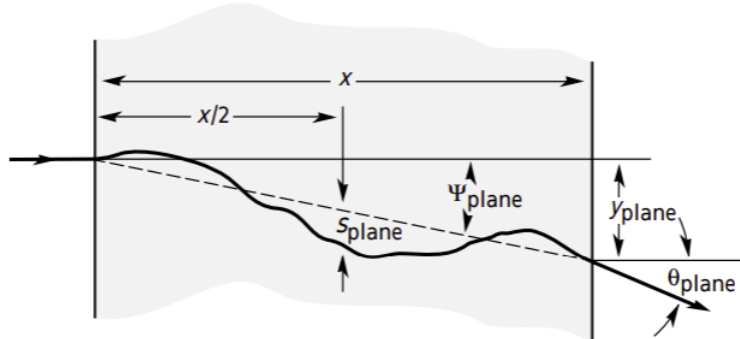


Fig. 3.4

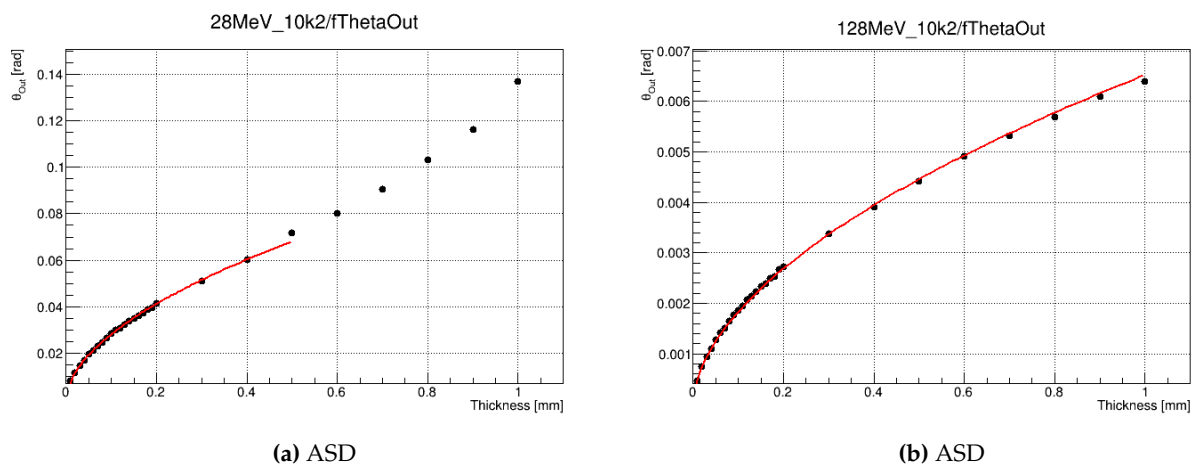


Fig. 3.5: Average scattering angle in different thicknesses of BC400® scintillator for μ^+ at 28 MeV/c and 128 MeV/c. From these plots was found $X_0 = (54.33 \pm 0.12) \text{ g/cm}^2$.

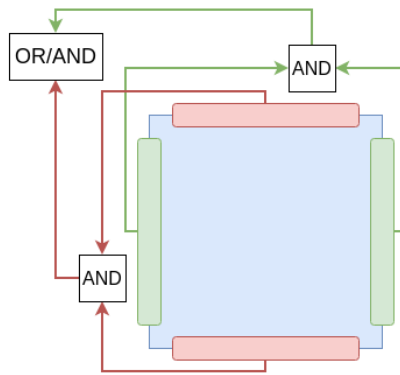


Fig. 3.6: Multiple readouts of a thin scintillator to lower the threshold and improve the dark noise rejection. Possible schemes are $(s_1 \wedge s_3) \vee (s_2 \wedge s_4)$, $(s_1 \wedge s_3) \wedge (s_2 \wedge s_4)$, or simply $(s_1 \wedge s_3)$.

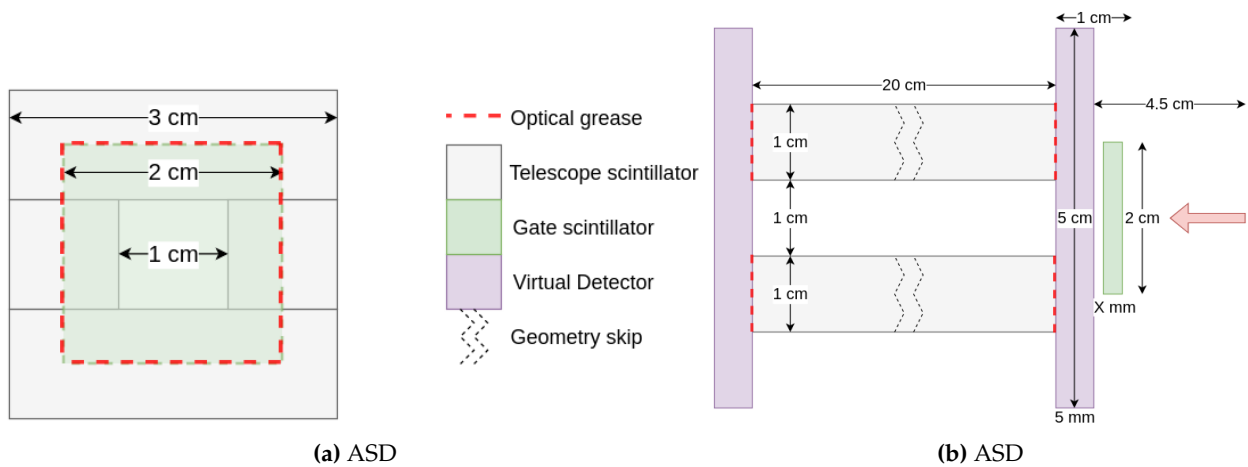


Fig. 3.7

Thickness and number of photons

Detection of photons

Not all photons produced will be detected. This is affected by the position, number, size, and PDE¹ of the SiPMs. To simulate the SiPM readout we can use a silicon volume coupled to the scintillator via an additional volume of optical grease². Multiple readouts would allow us to lower the threshold and improve the dark noise rejection. Calling the sides s_i , the options could be $(s_1 \wedge s_3) \vee (s_2 \wedge s_4)$, $(s_1 \wedge s_3) \wedge (s_2 \wedge s_4)$, or simply $(s_1 \wedge s_3)$. We studied these different readouts schemes in the beamtime of Dec. 2023 (see Sec. 3.5)

3.2.3 Telescope and entrance detector

3.3 Beamtime 2021

This was the first muEDM beamtime I participated in. I took an active part in the setup and measurement and I followed the analysis of the data collected. This section relies on the Master Thesis of Tim Hume, part of the muEDM collaboration. This beamtime was designed to study the positron multiple scattering in different thin foils of the material expected to be viable solutions for the different parts of the experiment. On top of the material details, the aim was also to validate the scattering model used in the GEANT4 simulations for further reference. The setup was quite simple: a telescope of five silicon pixel sensors, three upstream and two downstream.

3.3.1 Description of the multiple scattering

Highland The Highland formula for multiple scattering is a parameterization for the width of the multiple scattering distribution. For a particle of charge z , momentum p traversing a thickness of x of a material with radiation length X_0 , the RMS of the gaussian distribution is estimated as:

$$\theta_0 = \frac{13.6 \text{ MeV}}{\beta p c} z \sqrt{\frac{x}{X_0}} \left(1 + 0.038 \ln\left(\frac{xz^2}{X_0 \beta^2}\right) \right) \quad (3.2)$$

Often, in the context of high particle physics, the projection on the directions orthogonal to the momentum are considered:

$$P(\theta_{x,y}) = \frac{1}{\theta_0 \sqrt{2\pi}} \exp\left(-\frac{\theta_{x,y}^2}{2\theta_0^2}\right) \quad (3.3)$$

GEANT4 The default parameterization of the multiple scattering in GEANT4 is the Urbán. This is based on a different description of the process, required because when evaluating the processes at each step of the simulation, meaning *within* the volume. This model describes the angular distribution of multiple scattering and samples it every interaction. The probability density of the angular distribution is usually indicated with $g(u)$ where $u = \cos \theta$ and the form is the following:

$$g(u) = \alpha + \begin{cases} \beta \exp(\gamma u) & \text{for } u_0 \leq u \leq 1 \\ \delta(1-u)^\epsilon & \text{for } -1 \leq u < u_0 \end{cases} \quad (3.4)$$

The parameter u_0 is the one used to transition between the central Gaussian-like distribution and the Rutherford-like tails at larger angles.

For the Highland formula, the PDG reports an accuracy of $\sim 10\%$ in the range $10^{-3} < x/X_0 < 10^2$ [1], meaning it is less reliable for thin targets for which $x/X_0 \sim \mathcal{O}(10^{-4})$. On the other hand, while GEANT4 results have been widely tested against experimental measurements, there is a lack of data to compare in the ranges we are interested in.

¹Photon detection efficiency describes the effectiveness of a photon detector in registering incoming photons. It quantifies the probability that a photon incident on the detector will be detected and converted into an electrical signal

²Also known as optical coupling grease or index-matching grease, is a specialized type of grease used in optics and photonics applications. It is designed to improve the optical coupling between two optical components, such as lenses, prisms, or optical fibers.

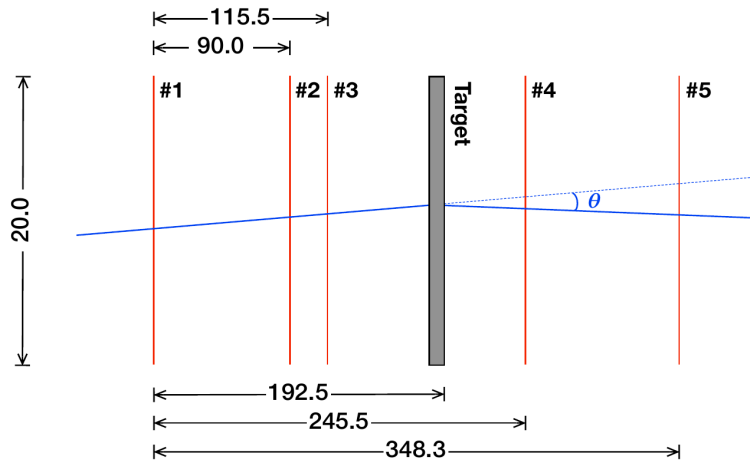


Fig. 3.8: Sketch of the telescope of Silicon Pixel Sensors used to study the multiple scattering in different materials. The samples are held in the position of the 'target'. In this sketch, the beam is coming from the left side.

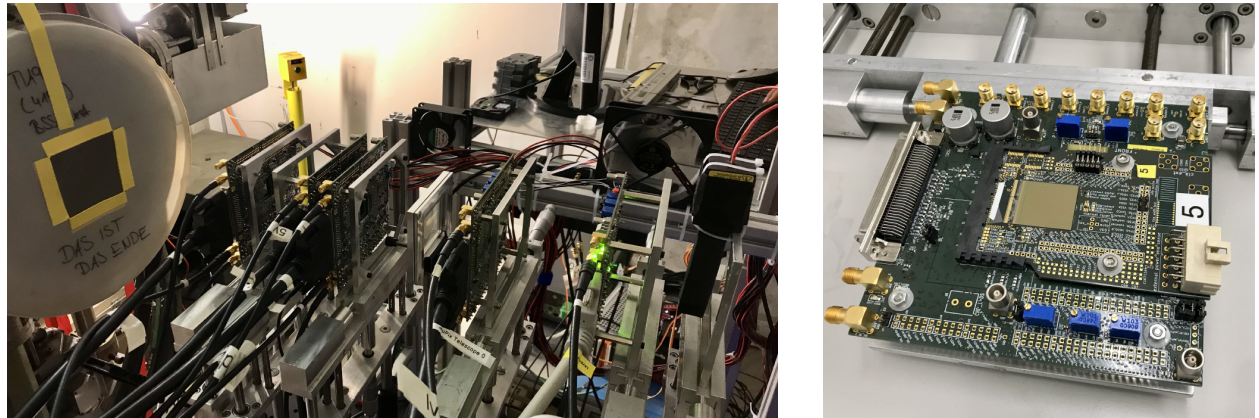
3.3.2 Data taking

The idea behind the data taking is quite simple: a study on the multiple scattering can be performed using a beam telescope, such as the one sketched in Fig 3.8, in which the two sides of the telescope are used to track the in/out-coming particles. The delicate point is to carefully take into account the scattering of the particles in the telescope itself. It is then needed to collect data without the sample to apply a deconvolution of the telescope response. The downstream part of the detector is not symmetrical to the upstream because only five sensors had the necessary performance. This made the tracking task more challenging, leading to wider distributions. The beamline used is the $\pi E1$, which provides π^\pm, μ^\pm, e^\pm in a momentum range 100 MeV to 500 MeV. Clearly, a good understanding of the beam is key in both data-taking and analysis. An example is the study of the beam changing the degrader's thickness, shown in Fig. 3.10. For brevity, the description of the electronics and DAQ system will be skipped.

Silicon Pixel Sensors The sensors used are the last iteration of the sensors of the *mu3e* experiment, the MuPix10. These are High Voltage Monolithic Active Pixel Sensors (HV-MAPS) with 250×256 pixels of dimensions $80 \mu\text{m} \times 80 \mu\text{m}$. The sensor itself is on a PCB used for delivering the required voltages. A second, larger, PCB is set below the first and is responsible for reading and transmitting the data to FPGA. These sensors have been developed to achieve excellent position and time resolutions ($100 \mu\text{m}$ and 20 ns) with efficiency of $\epsilon \approx 0.99$. The thickness of these sensors is $50 \mu\text{m}$ but this was the case for just the detector positioned after the samples. The others were $100 \mu\text{m}$, important to be considered during the analysis. The whole apparatus is shown in Fig. 3.9a while a singular MuPix10 is shown in Fig. 3.9b.

3.3.3 Data analysis

Track selection Initial angular distributions obtained were broad due to noise in downstream sensors, making it difficult to distinguish noise from true hits. To address this, a filtering process was developed to select the track candidate with the least spatial separation between the



(a) Picture of the setup for the beamtime of 2021. On the right, the scintillator was used as an external trigger, on the left, beam exit window.

(b) Picture of one of the MuPix10 mounted on the two PCBs.

Fig. 3.9: Picture of the setup and one of the MuPix10 (grey-colored square) mounted on the PCBs.

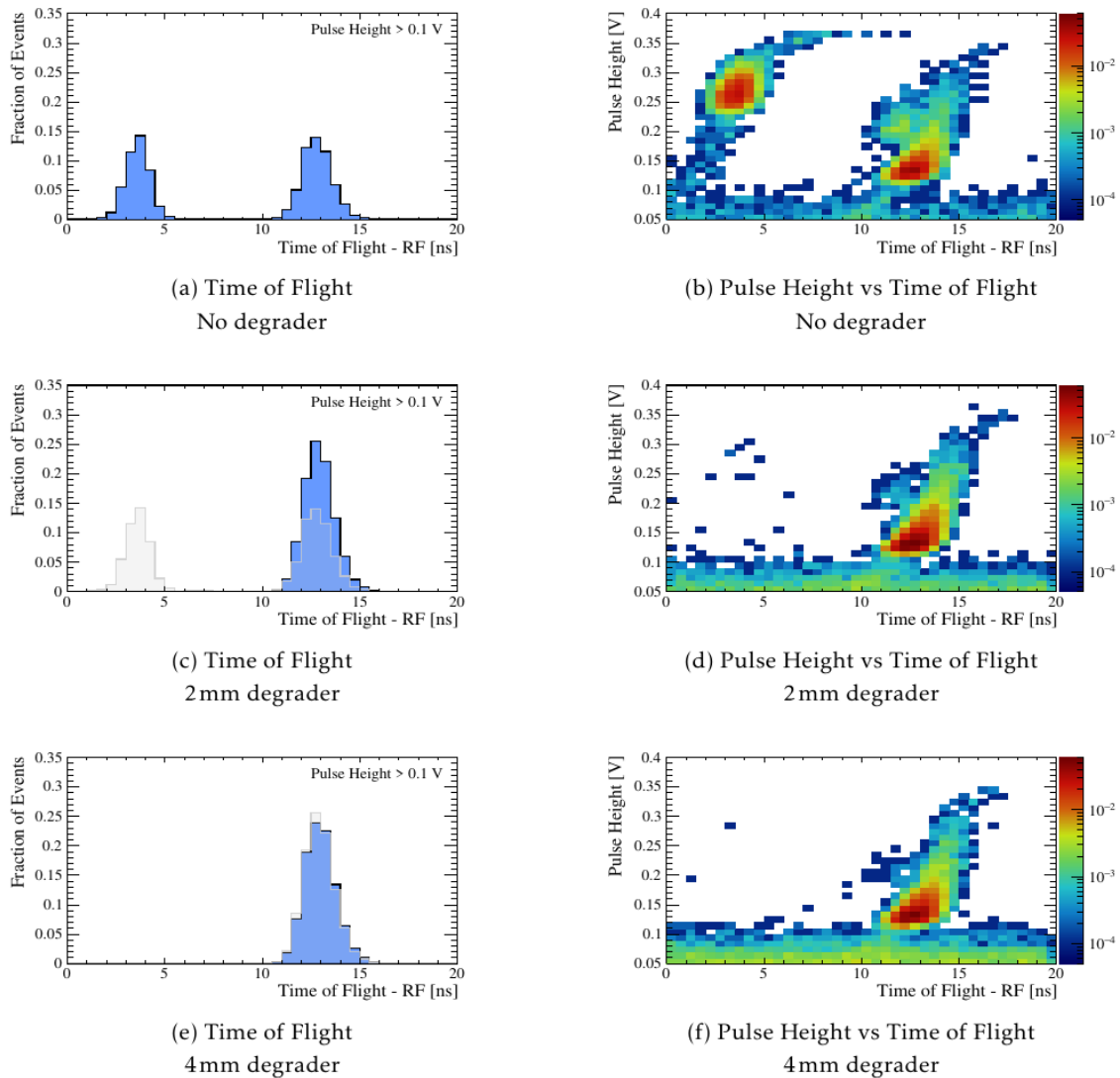


Fig. 3.10: Timing and the 2D plot for time and pulse height for 120 MeV/c particles. The three rows show what happens when inserting degraders of different thicknesses. With no degrader, the π peak is visible at lower TOF. When increasing the thickness, the contributions of π and μ decrease. It is important to note that the e and μ distribution overlap. In gray the distribution of the previous plot to make a comparison.

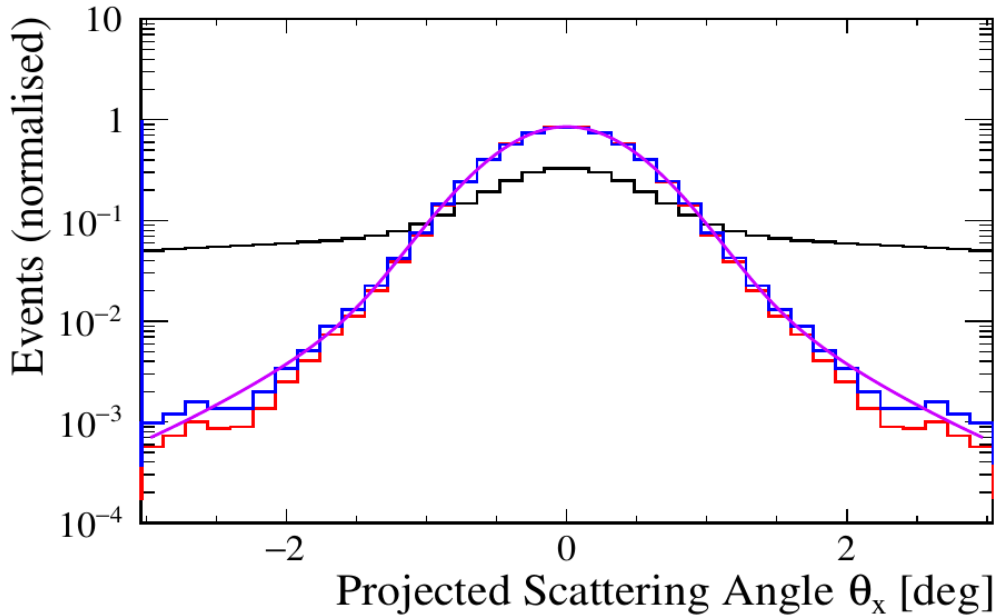


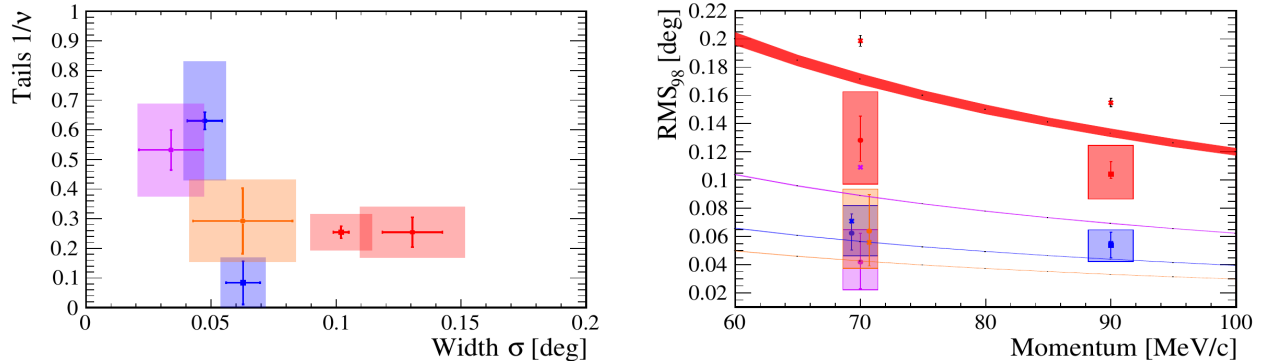
Fig. 3.11: The angular distributions show: the full distribution (black), the distribution after cuts in the distance at the sample’s plane (red), the distribution after acceptance correction (blue), and the fitted function for telescope characterization (violet).

intersections of upstream and downstream tracks on the plane of the sample. The expected angular distribution for particles passing through a material at normal incidence should be spatially symmetric and independent of chosen projection axes. Any deviation from this symmetry could indicate experimental, data processing, or analysis errors. To mitigate the effects the idea was to combine distributions from multiple axes. In the initial distributions, the broad background can be attributed to false tracks generated by noise, poor fits, and some contribution of events with large angles of scattering in the telescope itself. This background was suppressed by enforcing a distance of 1 mm between the points at which the upstream and downstream tracks intersect the plane of the sample. Distributions before and after applying this filter are shown in black and red in Fig. 3.11. This distribution was then corrected for the geometric acceptance of the telescope.

Acceptance The correction for the geometrical acceptance of the telescope was essential to accurately determine the tails of the angular distribution. To estimate the acceptance, for each upstream track identified, scattering angles were randomly assigned and added to a histogram, distinguishing instances within the acceptance of the most downstream sensor. The ratio of histograms yielded the average acceptance as a function of projected scattering angles. The acceptance correction was applied on a per-event basis, adjusting the scattering angles based on the acceptance value. An example of such correction is shown in blue in Fig. 3.11

Deconvolution The method of track selection and acceptance correction was applied to both runs with and without the sample. The distributions from these runs were then fitted. The process involved:

- Characterizing the telescope’s response without the sample using a weighted sum of a Gaussian distribution and a Student’s t distribution



(a) Pokalon (orange), 17 μm Graphite (blue), 50 μm Graphite (violet), Silicon (red); circular markers for data at 70 MeV and squared at 90 MeV; error bars are the statistical uncertainties and the shaded area is the total uncertainties.

(b) Same color/shape coding as Fig. 3.12a and the predictions of the Highland formula are shown by lines of width representing the uncertainty in thickness.

Fig. 3.12: Results of the analysis of the different samples and confronted with predictions using the Highland formula and GEANT4. The details are not easy to read but the ‘bring-home’ message is that the results are somewhat in agreement and some improvement are planned on the analysis.

- Convolving the response function with the sample’s angular distribution, assumed to follow a single Student’s t distribution
- using the negative log-likelihood to determine the best-fit parameters for describing the measured distribution with the sample

3.3.4 Model evaluation and conclusions

This first beamtime aimed at testing the agreement between the Highland formula and the GEANT4 Urbán model for the multiple scattering in thin materials. The analysis of the data collected is still not finalized, but a rough agreement between data and models can be seen in Fig. 3.12. There are improvements that could be added to the analysis and/or to the simulation of the experimental setup, so updated results are expected in the following months.

3.4 Beamtme 2022: Telescope and entrance detector

This second beamtime³ happened in November 2022. The amis where:

- Test of entrance scintillator with the additional ‘telescope’
- parasitic measurements for the TPC + GRIDPIX

This time I, together with Prof. Angela Papa and a David Stäger (a master student from ETH) participated actively in the development of the setup. In particular we took care of the entrance scintillator, auxiliary detectors, the electronic, vacuum system, and one version of the telescope. To test different reading options a second telescope was developed by the Shanghai part of the collaboration and they also helped developing the mechanical structure.

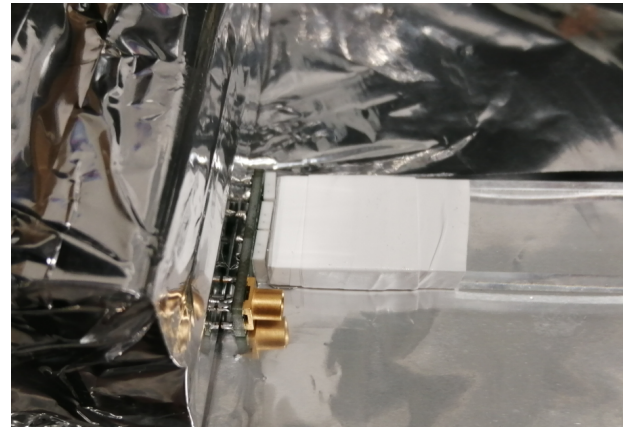
3.4.1 Construction

Electronics

³Not counting the one for the TPC + GRIDPIX of Sec. 2.3.3, this is the second beamtime related to the entrance detector.

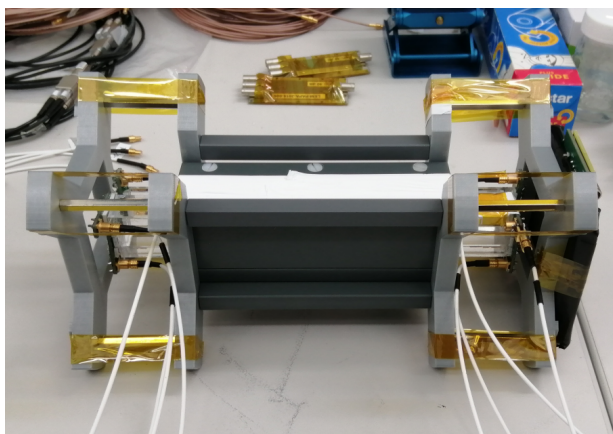


(a) Custom feed-throughs: PCB board, with soldered connectors, sealed with Stycast in a blind flange.



(b) A small PCB board with 3 SiPMs and one connector attached with optical cement to one of the scintillators.

Fig. 3.13: Part of the preparation needed for the beamtime was to develop the detectors, as well as the vacuum in which the measurement would have taken place.



(a) Assembly of the *telescope* with *entrance* and *veto*.



(b) "T" beamlne piece used as vacuum chamber.

Fig. 3.14: The *entrance* scintillator, the *telescope*, and the *veto* were assembled in a rigid structure. A "T" beamlne piece was used to put the detector in the beamlne. The lateral flange was adapted for the feedthroughs while, on the back, a Mylar® widow was mounted to allow further measurements of the beam.

Scintillators

Final setup

Shanghai's version

3.4.2 Data taking

3.4.3 Data analysis

3.5 Beamtime 2023: Multi readout entrance

3.5.1 Data taking

3.5.2 Data analysis

Bibliography on muEDM entrance detector

- [1] R. L. Workman et al. "Review of Particle Physics". In: *PTEP* 2022 (2022), p. 083C01. doi: 10.1093/ptep/ptac097.

Chapter 4

muEDM positron tracker

This chapter is an in-depth study on the development of the scintillating fiber part of the muEDM positron tracker. We will skip some preliminary studies and we will start with the description of the positron tracker which was included in the proposal of the experiment submitted to PSI at the end of 2022; we will move to the simulations done after that and the current design of this detector.

4.1 Tracking e^+ in muEDM

As already introduced in Ch. 2, the muEDM experiment is based on the *frozen spin* technique. First of all, it is cardinal to stop the muon in the right orbit. The careful calibration of the radial electric field will then change the $(g - 2)$ precession, bringing it eventually to 0. At this point, the direction of the positron emission will be the relevant variable for the EDM search. These three steps require a way to track the outgoing e^+ . Developing such a tracker in the muEDM environment is the challenge to which this chapter is dedicated.

4.1.1 The g-2 anomaly

4.1.2 The EDM

4.1.3 Design in the 2022 proposal

The ‘barrel’ geometry

SciFi prototype

Issues

Alternatives

4.2 CHeT or CyFi

The first step in developing and prototyping the geometry chosen in the previous paragraph is to understand the requirements for this sub-detector and how the prospected resolutions compare

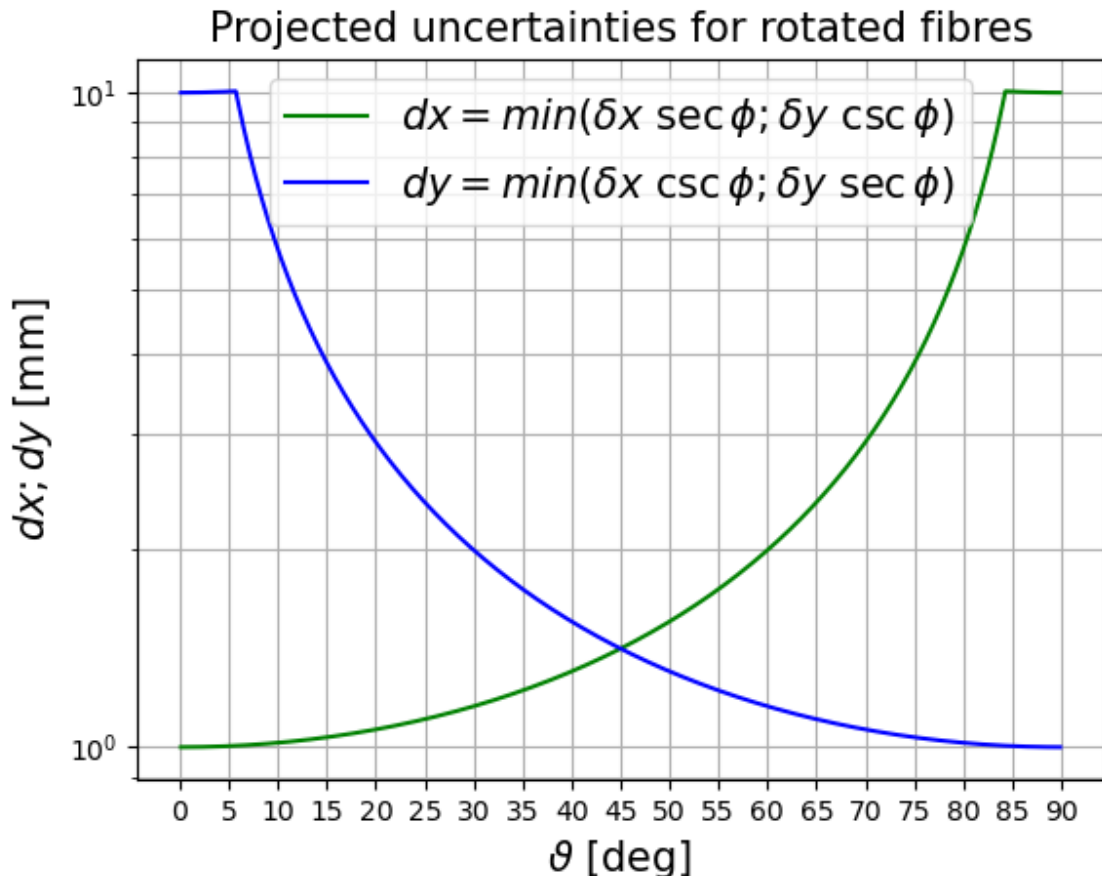


Fig. 4.1: Projection along the \hat{x} ; \hat{y} axes of the resolutions considering a ribbon of fibers rotated in different angles. The intrinsic resolutions are here assumed $\delta_x = 1 \text{ mm}$; $\delta_y = 10 \text{ mm}$.

to these. This scintillating fiber tracker will be used for position tracking and in particular is going to be complemented by silicon strips. The crucial information this system needs to provide is the longitudinal position of the particle with a good resolution: $\delta\ell \lesssim 1 \text{ mm}$.

4.2.1 Resolutions of crossed fibers ribbons

Let's consider a ribbon $3 \text{ cm} \times 15 \text{ cm}$ of squared fibers $250 \mu\text{m}$ running vertically. Assuming a 'perfect' readout, the resolution across the ribbon is given simply by the fibers' width while the resolution along the ribbon is extracted by reading the fibers on both sides. This second resolution is often quite worse than the previous. For practical purposes we will here assume $\delta_x = 1 \text{ mm}$; $\delta_y = 10 \text{ mm}$. Rotating the ribbon by an angle θ changes the projection of the resolutions on the \hat{x} ; \hat{y} axes and for this reason crossing two ribbons can improve the resolutions on the position of a crossing particle. When reading the ribbon on both sides the resolutions, as a function of θ , are given by the smaller between the projection of the two intrinsic resolutions.

$$\begin{cases} dx = \min(\delta_x \sec \theta; \delta_y \csc \theta) \\ dy = \min(\delta_x \csc \theta; \delta_y \sec \theta) \end{cases} \quad (4.1)$$

The relation between resolutions and the tilt angle is shown in fig. 4.4a.

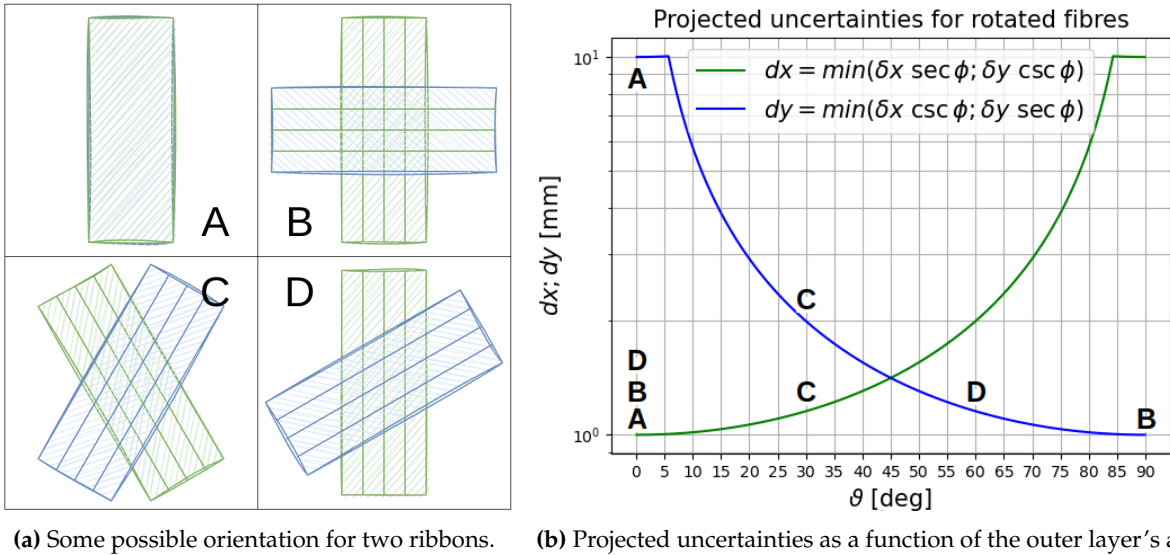


Fig. 4.2: Relation between the direction of the fibers and the associated uncertainties projected onto the axes. Some specific orientations of two overlapping ribbons are shown.

4.2.2 Angle choices for the layers

When considering two layers the angles must be chosen to improve the overall resolution, which in practice means minimizing the uncertainty only on one axes per ribbon. Let's consider the different layouts in 4.2a and how they translate to resolutions in 4.2b. Clearly having the two ribbons at 90 deg along the axes is the best option but if we want to avoid having the readout on the plane of the muon orbit we need to consider less steep angles for the single ribbons. Options C and D are the possible solutions and, looking at the resolutions, D is actually the configuration minimizing the resolutions on both axes. At this point is important to notice an additional constraint, given by the cylindrical geometry: if two fibers cross multiple times when both are scintillating the position of the impinging particle is ill-defined. There is a ‘real’ crossing point but also additional ‘ghosts’ hits. If we consider a two-layer system the requirement of having only one crossing point (i.d. no ‘ghosts’) translates to having a difference in the number of turns $\lesssim 1$. In a cylindrical geometry the relation between the angle of the fibers and the number of turns completed, shown in Fig. 4.3, is determined by the dimensions of the cylinder itself. At this point, we can plot the resolutions as a function of the angle of one of the layers keeping the angle for the second layer such as $\Delta T = 0$. The results are in Fig. 4.4a while Fig. 4.4b shows the difference in angle for the two layers. We will consider two concentric cylinders, the outer layer being the one with a shallower angle: this is intended to reduce the effect of multiple scattering on the longitudinal position. Building the layers with infinite precision on the angle is clearly not feasible for this reason we can use the plots in Fig. 4.5, where the angles have been rounded to multiples of 5 deg. Additional attention we can have is to consider the length of the scintillating fibers: if the fibers are too long the light collection at the ends is decreased by the absorption. The length of the fibers in both layers is shown as a function of the outer angle in Fig. 4.5c. Clearly, this is the extreme case: depending on the intrinsic resolutions of the fibers, shallower angles and $\Delta T < 1$ could be chosen, simplifying the construction.

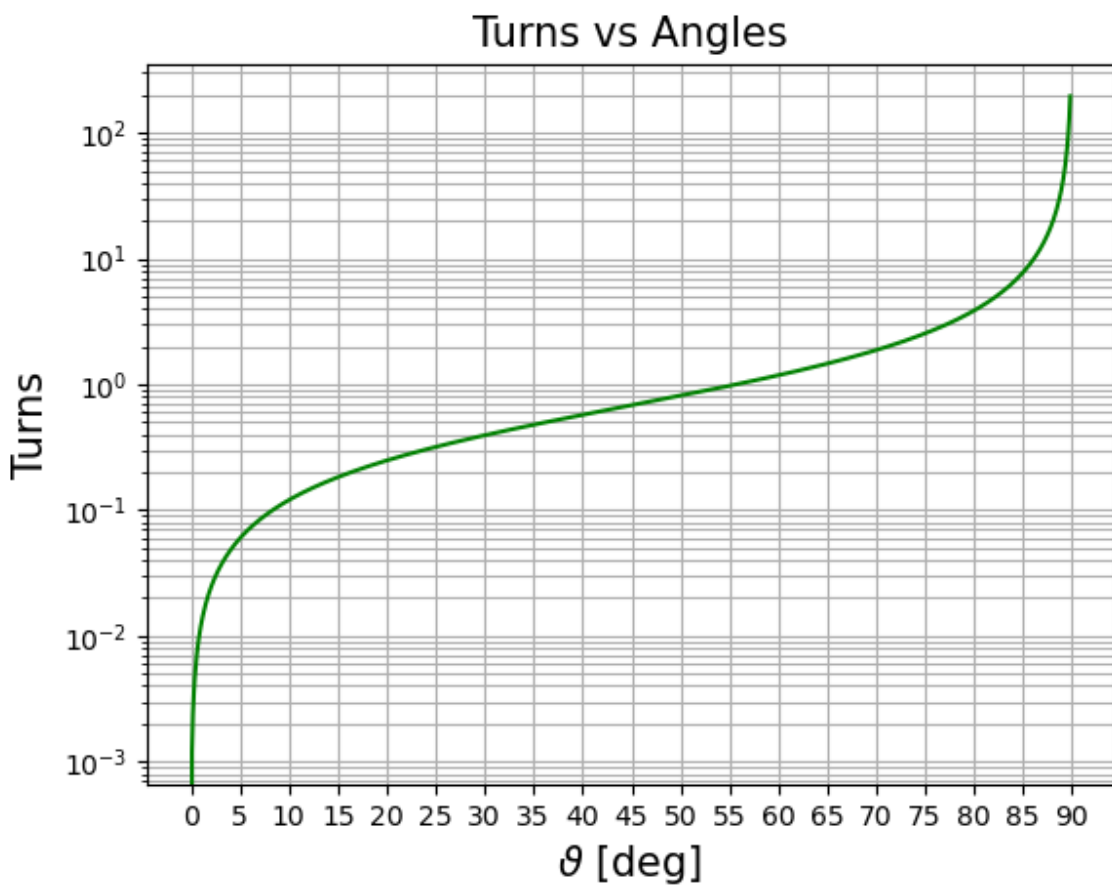
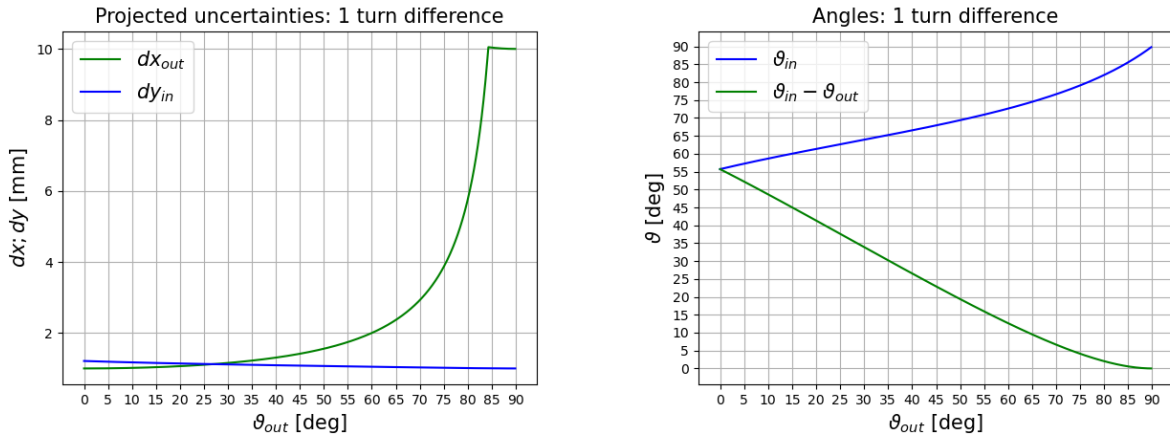


Fig. 4.3: In a planar configuration, the angle at which the fibers run translates directly to the angle at which the ribbon is oriented. In a cylindrical geometry, a fiber running at a given angle will complete a different number of turns depending on the dimensions of the cylinder.



(a) Projected uncertainties as a function of the outer layer's angle
(b) Angle of the inner layer and difference in angle as a function of the angle of the outer layer

Fig. 4.4: The results when considering two layers in a cylindrical geometry keeping the requirement $\Delta T = 0$: 4.4a shows the projected uncertainties; 4.4b shows the angle of the inner layer.

4.2.3 GEANT4 simulation

G4TessellatedSolid The first hurdle in the Geant4 simulation for this sub-detector is the definition of the geometry. The shape is the result of wrapping a squared fiber around a cylinder resulting in a ‘squared helix’. After some consideration there are two ways of defying this geometry:

- Taking bool difference of two G4TwistedBox¹. This is a simple solution but comes with some limitations: the shape of the fiber cannot be changed to circular; the twisted box cannot be twisted more than 90 deg, so a stack of clones is needed;
- Defying the geometry using G4TessellatedSolid², which means creating it by hand triangulating the shape. Clearly, this is a more cumbersome solution but it allows for more flexibility.

The core part of the code for generating the G4TessellatedSolid fibers is in appendix A.

Fibers and read-out Aside from the specific geometry, the cardinal point is how to describe the fibers and their readout. The fiber itself is simulated as a three-layer volume:

- Core:
- First cladding: PMMA
- Second cladding: PMMA EMA

The optical property of the surface between the different layers is specified with a G4OpticalSurface³.

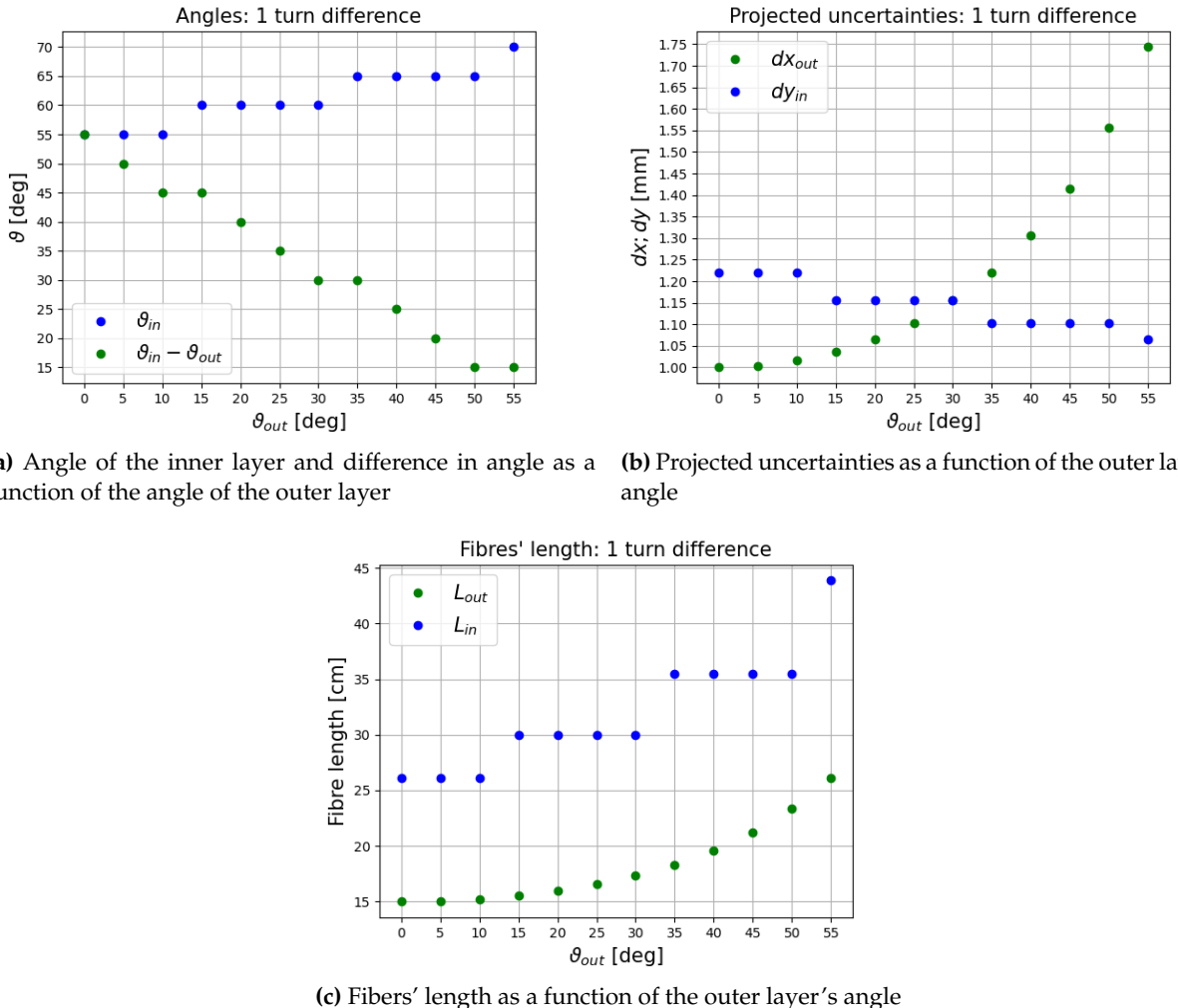
The readout simulates a SiPM:

- Optical grease:
- SiPM window: Silicon resin
- SiPM :

¹The documentation can be found here: G4TwistedBox

²The documentation can be found here: G4TessellatedSolid

³The documentation can be found here: G4OpticalSurface



(a) Angle of the inner layer and difference in angle as a function of the angle of the outer layer

(b) Projected uncertainties as a function of the outer layer's angle

(c) Fibers' length as a function of the outer layer's angle

Fig. 4.5: Key parameters as a function of the outer layer's angle keeping 1 turn difference between the two layers and rounding the angles to multiples of 5 deg.

4.2.4 From γ s to waveforms

The simulation in GEANT4 ends with the recording of the optical photons entering the SiPM SensitiveDetectors. The physical processes going from the impinging photons to the analog signal are quite complex and simulating them would require a lot of effort (and CPU time). To get a feeling of the type of signals we can expect from the simulation we can create a simple script *faking* the readout. The required steps are:

- *PDF*: probability of a photon converting. This is a binomial distribution and is SiPM dependent: reasonable values $p_{PDF} \in [0.3, 0.5]$
- *Response*: per photon converted, add a 'waveform' at the photon time. The shape $w(t)$ is SiPM/electronics dependent but some assumptions can be made.
- *Dead time*: when a pixel generates a signal, any additional photon coming within a t_D is lost.
- *Dark noise*: add a probability of spurious photons converting. This is a Poissonian process that gives n_{dark} photons distributed flat in the readout time.

$$W(t) = \sum_{i=0}^{n_\gamma} w(t_i | \Delta t > t_D) \cdot p_{PDF} + \sum_{i=0}^{n_{dark}} w(t_{flat}) \quad (4.2)$$

(4.3)

Once we obtain $W(t)$ we can apply a threshold w_{th} and turn the signal from analog to digital. If the w_{th} is crossed, we recorded a *hit*. Given the geometry under consideration, we need >2 *hits* to make a ‘cylinder’-*hit* (a *c-hit*). Mapping groups of hits in chits is not trivial and takes as parameters the dimensions of the cylinder and the SiPM numbers (or alternatively their position).

4.2.5 From *hits* to *c-hits*

4.3 Prototype/Beamtime

4.4 Conclusions

Part II

muCool

Chapter 5

muCool

5.1 The working principle

5.2 Simulations

5.2.1 Cooling

5.2.2 Extraction

5.2.3 Re-acceleration

5.3 Validation

5.4 Conclusion

[1] [2] [3] [4] [5] [6] [7]

Chapter 6

muCool upgrade

6.1 New target

6.2 Cryogenic system

6.3 High Voltage system

6.4 Conclusion

[1] [2] [3] [4] [5] [6] [7]

Part III

MEG II

Chapter 7

MEG II and the Cockcroft–Walton

This Chapter is dedicated to an in-depth description of the MEG II search and apparatus. After the description of the different subdetectors and their functionality a description of the beamlines will follow. MEG II is served by the main muon beamline, part of the PSI beamlines described in the Introduction Chapter, and a secondary proton beamline equipped with its own Cockcroft–Walton. This machine has different uses in the collaboration, which will be here discussed, and its functioning has been one of my main tasks. For this reason, some additional details will be here included. Most of the information on MEG II can be found in the two recent papers: detector [MEG_II:detector] and 2021 data-analysis [MEG_II:2021].

7.1 MEG II

The MEG II experiments aims at improving the limit set by its predecessor: $BR(\mu^+ \rightarrow e^+\gamma) < 4.2 \times 10^{-13}$ [1] down to $\sim 6 \times 10^{-14}$. The signature of this process is a back-to-back pair of γ and e^+ , with $E_\gamma = E_{e^+} = 53.2$ MeV. The main background is the accidental coincidence of high momentum positrons from Michel decay $\mu^+ \rightarrow e^+\nu_e\bar{\nu}_\mu$ and high energy photons from the radiative muon decay (RMD) $\mu^+ \rightarrow e^+\nu_e\bar{\nu}_\mu\gamma$, positron Bremsstrahlung or positron annihilation.

The experiment, which is located at PSI, is currently running and a sketch of it is shown in Fig. 7.1. In particular, the muons are delivered by the $\pi E5$ beamline. The key aspects of the upgrade are: a thinner and more slanted target, a pixelated Timing Counter (pTC), a new Cylindrical Drift Chamber (CDCH), the addition of a Radiative Decay Counter, a finer granularity for the Liquid Xenon Calorimeter (XEC) using MPPC, new electronics and calibration methods. The kinematic variables associated with the positron are measured with the spectrometer (COntant Bending RAdius magnet (COBRA)+CDCH+pTC). The kinematic variables ($E, t, \text{position}$) of the γ , expected to be monochromatic at 52.8 MeV, are measured with the XEC. This is a 1000 ℓ “c-shaped” Liquid Xe calorimeter, equipped with both PMT and SiPM.

Coordinate system The coordinate system used is cylindrical (r, ϕ, z) with its origin located at the center of COBRA. The z -axis aligns with the COBRA axis, coinciding with the direction of the incoming muon beam. The azimuthal angle $\phi = 0$ is positioned opposite the center of the LXe detector and corresponds to the x -axis, with the y -axis pointing upwards. Positrons follow trajectories characterized by decreasing ϕ coordinates. The polar angle θ , measured with respect

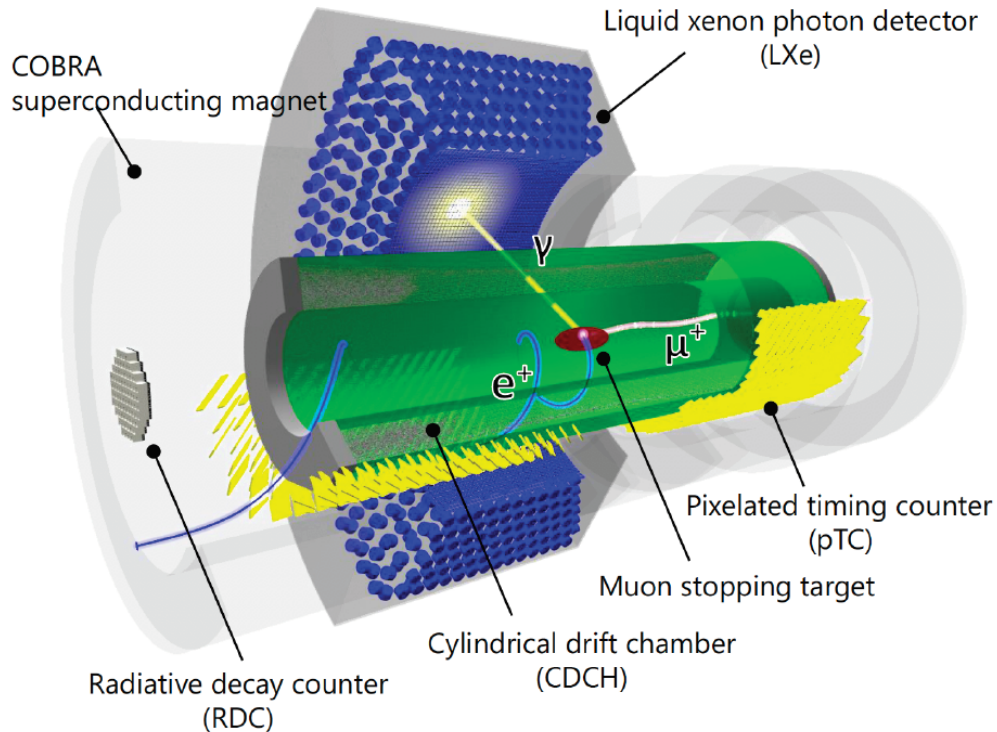


Fig. 7.1: Sketch of the MEG II apparatus with a $\mu^+ \rightarrow e^+\gamma$ event.

to the z -axis, is also employed. The region where $z < 0$ is referred to as upstream, while the region where $z > 0$ is termed downstream. The size of the LXe fiducial volume defines the geometrical acceptance of $\sim 11\%$: $\phi_\gamma \in [\frac{2}{3}\pi, \frac{4}{3}\pi]$ and $|\cos \theta_\gamma| < 0.35$.

Alignment The analysis of the relative alignment within each detector, like the extraction of the *real* position of the wires in the CDCH, and between the different detectors is key in the event reconstruction. We will not describe how these are performed but all the details can be found in [MEG_II:detector].

7.2 The liquid XEnon Calorimeter

As already introduced, the kinematic variables ($E, t, \text{position}$) of the γ , expected to be monochromatic at 52.8 MeV, are measured with the liquid XEnon Calorimeter (XEC). This is a 900 L LXe c-shaped tank and the main improvement from MEG has been the increase in the granularity of the photosensors on the inner face: from 216 5 cm round PMTs to 4092 $15 \times 15 \text{ mm}^2$ Multi-Pixel Photon Counters (MPPCs). The other faces are equipped with the same 668 PMTs as in MEG. To get the best performances from this detector, the running condition of the Xe is 165 K and 0.12 MPa. the description of the *ad hoc* cryogenic circuit will be skipped but can be found in the references. The local coordinate system is the following: u - axis along the beamline, v - vertical axis intersecting COBRA center, w - the depth in the detector.

7.2.1 Xe scintillation

MEG's XEC is the first large Xe detector based on scintillation. In Sec. 3.1 the working principle of scintillators was discussed but the description of liquid scintillators was postponed. Now is the time to pick up where we left off. Among the noble gases, Xe has a higher light emission wavelength, fast response, and short radiation length. On top of these qualities, its high density allows to keep the size of the detector reduced. All these aspects are the reason this element was chosen by the collaboration. However, the quality of commercial Xe is not at the level required, so a purification system was developed to guarantee transparency to the scintillation light.

Two processes can take place leading to the emission of scintillation photons at 178 nm:

- Excitation: $\text{Xe}^* \xrightarrow{\text{Xe}} \text{Xe}_2^* \longrightarrow 2\text{Xe} + \gamma(178\text{ nm})$
The ionizing particle creates an exciton which combines as an excimer and radiates
- Ionization: $\text{Xe}^+ \xrightarrow{\text{Xe}} \text{Xe}_2^+ \xrightarrow{e^-} \text{Xe} + \text{Xe}^{**} \longrightarrow \text{Xe}^* + \text{heat} \longrightarrow \text{Excitation}$
If a charged exciton is created, the charged excimer first needs to be thermalized

The fraction of excitation and ionization depends on the status of the Xe and on the ionizing particle and some deviations are possible from the processes illustrated, meaning not every exciton will lead to scintillation. We will not cover these aspects but we will name a peculiar aspect related to the ratio between the different processes. Experimentally has been proven the waveforms produced by α and γ present different decay time: $\tau_\alpha = (19.4 \pm 1.9)$ ns and $\tau_\gamma = (50.9 \pm 4.0)$ ns.

Purification To keep a high light yield and vacuum ultra-violet (VUV) transparency, the Xe needs to be purified, removing water, oxygen, and nitrogen. The most effective way is to purify it in the liquid phase, circulating through a molecular sieve. Unfortunately, this cannot happen while taking data due to the noise introduced in the system and is done every year before the run starts. Purification in the gaseous phase is done during the whole beam time with a hot getter.

7.2.2 Photon detection

The MPPCs and PMTs used went through a period of R&D due to the harsh environment:

- The Xe spectrum is centered at 178 nm: vacuum ultra-violet regime
 - To ensure the light collection, the sensors are immersed at 165 K
 - A high rate is given by radiative muon decays and secondary particles from the beamline
- Still, the gains and efficiency of these sensors are continuously evolving, making it necessary to develop different calibrations to optimize the detector and specific procedures to regain efficiency lost in the in-between runs. For example, the PDE of the MPPC is recovered via the *annealing*.

Annealing While the value for the UVU photon detection efficiency (PDE) of the MPPS was measured to be 0.20 ± 0.02 , during the commissioning run of 2017 the value measured was 0.13 ± 0.01 . After a detailed investigation, the decrease was attributed to radiation damage. To recover the PDE, a process of annealing was applied to the MPPCs. The Joule heating of the MPPC served as the heat source while LED light was used to induce a current. Each MPPC was annealed ~ 28 h, recovering the PDEs enough to tolerate radiation damage of the physics run for a full year. The

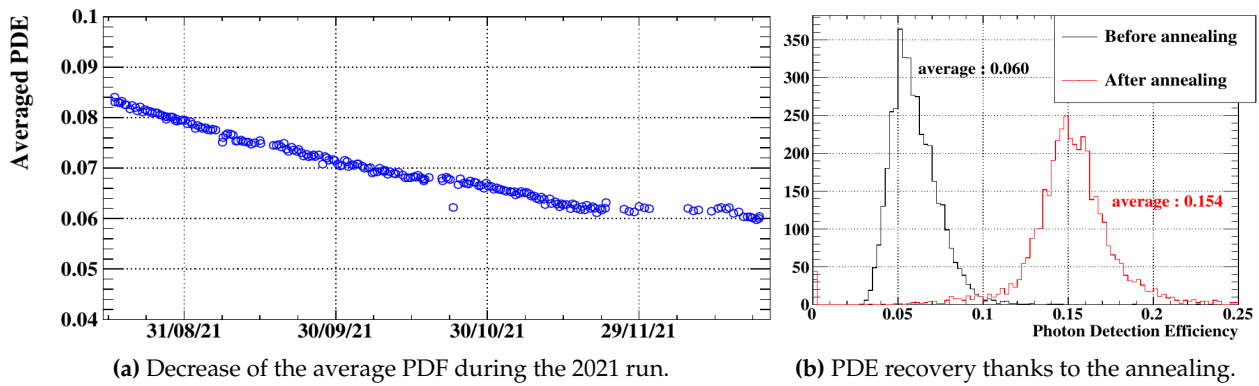


Fig. 7.2: The PDE of the MPPCs was found to be deteriorating due to radiation damage (a). The process of annealing carried out before every physics run, allows the recovery of the PDE (b).

decrease of PDE during 2021 and the recovery after the annealing process are shown in Fig. 7.2. This procedure has been repeated every year before the MEG II physic runs.

PMTs' gain The absolute gain of PMTs is evaluated by shining the sensors with a blue LED and evaluating the linear correlation between the mean and variance of the *charge* as a function of the LED intensity. At the beginning of each run, the gains are set to $\sim 0.8 \times 10^6$ adjusting the HV. This value will then lower during the run, as shown in Fig. ??.

7.2.3 Calibration

As anticipated, different calibrations were developed to follow the evolution of the XEC and to tune its functionality. There are three calibrations taken 3/5 times a week plus the Charge Exchange calibration, done once a year.

LEDs The first of these procedures is done every day, shining the sensor with two different LED lights. This allows us to evaluate the photon detection efficiency (PDE) and Excess Charge Factor (ECF) of the MPPCs. The absolute gain of PMTs is also evaluated, with a blue LED, and extrapolating the linear correlation between the mean and variance of the *charge* as a function of the LED intensity. At the beginning of each run, the PMT's gains are set to $\sim 0.8 \times 10^6$ adjusting the HV. Just like the MPPC PDE, this value will then lower during the run.

α -particles PDEs and QEs are evaluated by comparing the number of registered photoelectrons and the expected value, evaluated via MC knowing the positions of the ^{241}Am source of α -particles. The cosmic rays are the background for this calibration and are distinguished via a pulse shape discriminator. The uncertainties on the PDEs/QEs is 10%.

$^{7}\text{Li}(p, \gamma)^{8}\text{Be}$ The 17.6 MeV line of the $^{7}\text{Li}(p, \gamma)^{8}\text{Be}$ reaction is also used to calibrate the XEC. This line is produced impinging a beam of 500 keV protons, produced via a Cockcroft-Walton (which will be described in a following section) on a ^{7}Li target.

CEX The last of the calibrations is more complex and requires changing the beam from μ^+ to μ . For this reason, it is performed only once a year. The process is the Charge EXchange reaction (CEX), $\pi^- p \rightarrow \pi^0 n$ and $\pi^0 \rightarrow \gamma\gamma$, and produces flat γ in [54.9, 82.9] MeV. Tagging the back-to-back events it is possible to select the low end of the spectrum, which is close to the expected signature of $\mu^+ \rightarrow e^+\gamma$ at 52.8 MeV. This calibration will be discussed in detail in Ch. 8.

7.2.4 Reconstruction and performance

Let's now discuss how the kinetic variables of the detected γ are extracted and the current understanding of the overall performance of this detector. We will outline the process for the reconstruction without going into details, which can be found in the recent paper [[MEG_II:detector](#)].

Position The procedure used to find the position x_γ of the hit is based on the assumption the amount of light collected by each sensor is proportional to the solid angle at the interaction point. This defines a quantity to minimize, a χ^2 of the registered and expected photons, given the position of each sensor. The position resulting from the fit is then corrected to account for the directionality of the detected photon and the finite size of the EM shower.

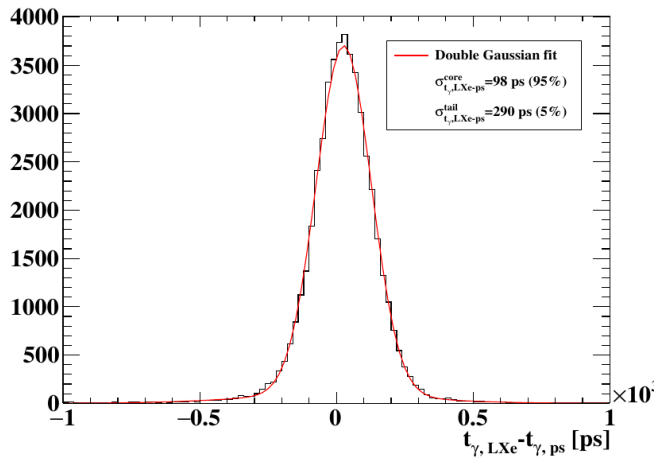
Time The timing t_γ of the first interaction of the photon is evaluated by minimizing a second χ^2 taking into consideration all the different aspects, like the travel time from the position to the sensors or the offset of each sensor. These parameters are evaluated via a dedicated calibration, the Charge EXchange reaction (CEX). The results of such a calibration are shown in Fig. 7.3a

Energy The last ingredient is E_γ , which is evaluated as the sum of the number of photoelectrons of each sensor scaled by a factor from N_γ to energy and corrected for a temporal and positional dependence ($T(t)$, $X(u, v, w)$). Again, the resolution near the signal energy is evaluated via the CEX. The results are shown in Fig. 7.3b. The energy scale has been found to be non-uniform. For this reason, a 3D correction $C(x, y, z)$ was developed by joining the information from the CEX runs, the ${}^7\text{Li}(p, \gamma){}^8\text{Be}$ 17.6 MeV line, and the studies of the background.

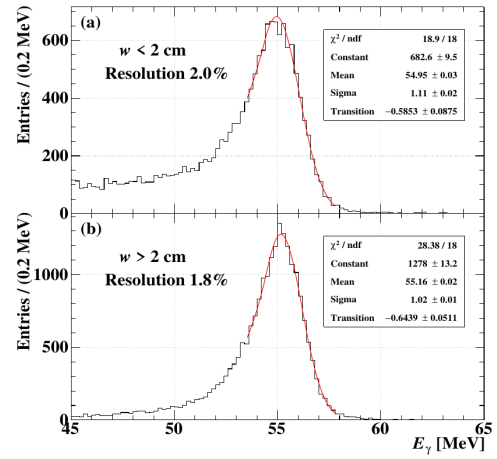
Resolutions

From the analysis of the data collected during the CEX, energy, and timing resolutions can be evaluated near the signal region ($E_{CEX} \sim 55$ MeV vs $E_{MEG} \sim 52$ MeV). The resolutions are extracted by performing a fit, shown in Fig. 7.3 to a double Gaussian for the timing and Eq. 7.1 for the energy. For the energy, two regions are necessary because of a low-energy tail originating from the interaction with the detector surface. The resolutions obtained are $\sigma_{E_\gamma} / \mu_{E_\gamma} = 2\%; 1.8\%$. From design, the relative resolution was expected to be $\sigma_{E_\gamma} / \mu_{E_\gamma} = 2\%; 1.7\%$ and the discrepancy is still under study. One possible explanation could be in the behavior of the Xe as a scintillator, given that a similar discrepancy was found also in MEG.

$$F = \begin{cases} A \exp\left\{-\frac{(x - \mu_{E_\gamma})^2}{2\sigma_{E_\gamma}^2}\right\} & \text{if } x > \mu_{E_\gamma} + \tau \\ A \exp\left\{-\frac{\tau(\tau/2 - x + \mu_{E_\gamma})^2}{\sigma_{E_\gamma}^2}\right\} & \text{if } x \leq \mu_{E_\gamma} + \tau \end{cases} \quad (7.1)$$



(a) Time resolution of the XEC, obtained via the time difference of XEC and *pre-shower* fitted with a double Gaussian.



(b) Energy resolution of the XEC. The function used is Eq. 7.1.

Fig. 7.3: Timing (a) and energy (b) resolutions of the XEC obtained for 55 MeV γ s generated via the CEX. The results are for the central region of the detector ($u \in [-10, 10]$ cm and $v \in [-30, -10]$ cm).

7.3 Spectrometer

As already introduced, the spectrometer for the positron's kinematic variables is made of COBRA, CDCH, and pTC. We will now review their working principles and designs.

7.3.1 COBRA

The COnstant Bending RAdius magnet (COBRA) consists of a main superconducting magnet and two normal conducting compensation coils. The main magnet itself is made of five coils with three different radii to generate a carefully studied gradient to achieve two goals:

- Make so that a positron with a given momentum would follow a trajectory of specific radius *independently of the angle* at which the particle has been emitted
- *Quickly* sweep particles emitted at very steep angles, to reduce the pileup

7.3.2 Cylindrical Drift CHamber (CDCH)

The major difference between MEG's drift chamber and its successor is that the CDCH is a single-volume, replacing the segmented structure. This is a ~ 1.9 m long cylinder, filled with a helium-isobutane mixture and containing nine concentric layers of 192 gold-plated tungsten wires, which are the heart of this detector. While these wires collect the signals from drift electrons, cathode and guard wires ($\sim 10\,000$ silver-plated aluminum wires) form squared drift cells ranging from 6.6 mm to 9.0 mm.

The geometry of the CDCH differs slightly from the design. For example, 10 layers were planned but 9 were installed due to time limitations. This time was invested in studies to reduce the probability of wire braking. This was mainly due to galvanic corrosion of the aluminium core, caused by air humidity penetrating through small cracks in the silver coating. The final result after mounting all the wires is shown in Fig. 7.4. The change in tracking efficiency was studied with simulation yielding a decrease of $< 1\%$. Many additional studies can be found in [MEG_II:detector], like the GARFIELD++ simulations, gas mixtures analysis, and wire tensions. To prevent discharges and

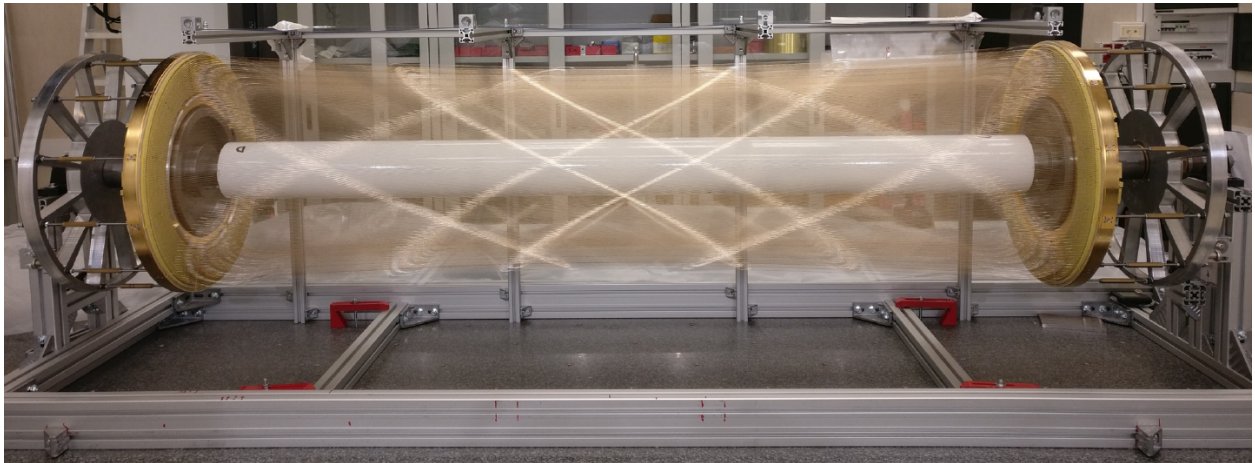


Fig. 7.4: CDCH with all the wires mounted.

improve the overall stability, the original He-isobutane gas mixture (90 : 10) was also modified adding a small fraction of oxygen and isopropyl alcohol.

While the 144 HV are supplied with a commercial system, WaveDREAM boards supply the necessary low voltage for the front-end and take care of the digitalization of the waveforms collected at both ends of the wires.

Hits The first step in positron tracking is identifying signals (*hits*) induced by drift electrons in the waveforms of the CDCH cells. These hits are characterized by multiple pulses from different ionization clusters, stretched due to the slow drift time of electrons. Signal-to-noise discrimination and pileup identification are essential. Two waveform processing algorithms have been developed:

- The first algorithm entails two reductions of the noise, fixed voltage thresholds, and integration over 20 ns. First, subtraction of a coherent low-frequency noise averaged on adjacent channels (excluding the region with signal pulses). This reduces the noise levels from 23 mV to 13 mV. Then a high-frequency cut-off at 225 MHz using a discrete Fourier transform technique to eliminate incoherent high-frequency noise.
- The second method utilizes a deep-learning algorithm based on a convolutional neural network (CNN). This CNN model takes waveforms from eight neighboring cells as input and learns the patterns of coherent noise and signals, outputting the probability of the first cluster's arrival time at each sampling point. It is trained using simulated waveform data with randomly added hits and overlaid with real noise data collected without the beam.

The second method results in higher hit efficiency but also a higher fake hit rate. To optimize results, the reconstruction process is done once with hits found using the first method and once with hits from both methods combined. The final results are combined after the reconstruction is completed, favoring higher quality tracks if successful with both methods.

The arrival time differences of signals and charges collected at both ends of a wire provide rough (few cm) information about the z-coordinate of the hit along the wire. Stereo wire configuration further improves the z-coordinate resolution. This makes the track finding more robust, especially against pileup.

Since multiple clusters often appear on one waveform, identifying the first cluster's time is crucial

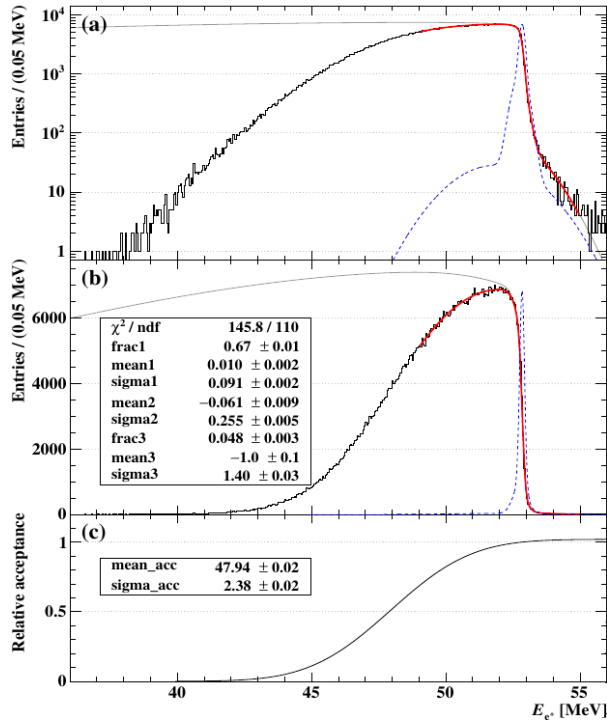


Fig. 7.5: Michel positron spectrum in logarithmic (a) and linear (b) scales. Black - data; Blue - 3 Gaussians to describe the resolution; Red- fit. The acceptance curve is shown in (c).

for correct drift circle reconstruction. The arrival time of the first cluster is determined from the summed waveform of both ends after adjusting their relative timing. The drift time of the first cluster is converted to DOCA using the time-distance relationship (TXY tables).

Track After identifying and reconstructing hits, a pattern recognition algorithm (track finder) and a track-fitter algorithm, both based on Kalman filters¹, are employed:

- The track finder initiates from hit pairs in outer layers with lower occupancy and generates track seeds by combining compatible pairs from different layers. Each seed is propagated through adjacent layers, checking consistency with hits and updating track parameters. Candidates with at least seven hits are formed.
- The track fitter utilizes an extension of the Kalman filter called the deterministic annealing filter (DAF) and resolves left/right ambiguities. It fits individual track candidates from the track finder, combining segments to form multi-turn tracks within CDCH. Tracks are propagated to the pTC and backward to the target, with re-fitting based on updated DOCA using the best-estimated T0.

During tracking, DOCA of each hit is iteratively refined. Initial DOCA values are estimated from Garfield++ simulations, but they can be biased due to low cluster density. An alternative DOCA estimate is obtained through neural network approaches, providing a more accurate estimation and improving positron kinematics by about 10%. This CNN-based method is used for final DOCA estimation during the re-fit process.

¹The Kalman filter is a recursive procedure to ‘bend’ the result of a fit. A simple example explanation and an example in 2D are shown in App. B, taken from [2]

Performance and efficiency

CDCH2 The studies prompted by the wire breakage evolved in an R&D for the updated version of the CDCH. The main change was the choice of pure aluminum 50 µm wires, almost insensitive to corrosion. One of the main challenges spawned by this choice was to develop a solid way of fixing the wires to the PCBs: the solution found was a combination of soldering and gluing. The CDCH2 will be completed by the end of 2023 and delivered to PSI in spring 2024. The choice of mounting the new system will then depend on the current status and stability of the CDCH.

7.3.3 pixelated Timing Counter (pTC)

The time coincidence between e^+ and γ is crucial at high R_μ . The pixellated Timing Counter plays two roles: first, it is part of the trigger algorithms; second it assigns the time of the positron track, which is then propagated backward to the target plane t_{e^+} . This detector is made of two symmetric half-cylinders of scintillators between the CDCH and COBRA, as shown in Fig. 7.6. To cover the e^+ acceptance corresponding to a γ entering the XEC, the pTC covers : $23\text{ cm} < |z| < 117\text{ cm}$ and $-166\text{ deg} < \phi < 5\text{ deg}$. Each sector is made of 256 Bicron BC422® plastic scintillators read on opposite sides by arrays of 6 AdvanSiD $3 \times 3\text{ mm}$ SiPM, as shown in Fig. 7.7. The tiles are wrapped in 35 µm polymeric reflector and 30 µm TEDLAR®.

The size and location of the tiles were optimized with ad hoc simulations: two different sizes ($120 \times 40 / 50 \times 5\text{ mm}^3$) are placed in a 16×16 matrix in the $z\phi$ plane and tilted by 45 deg to be orthogonal to the positron trajectories. This configuration was chosen to maximize the multiplicity for signal-like positrons limiting the material budget. The mean multiplicity from MC is $\langle N_{hit} \rangle \sim 9$ and the obtained resolution $\sigma_{t_{e^+},pTC} \sim 40\text{ ps}$. To intercalibrate the timing offsets of the system, most tiles are lit with a synchronous light pulse via optical fibers.

Performance The single-counter time resolutions were measured to be $\sigma_{t_{e^+},pTC}(N_{hit} = 1) \sim 80 - 120\text{ ps}$ for counters with heights of 40 mm and 50 mm. These resolutions correlate with light yield, influenced by scintillator aging, SiPM detachment, and radiation damage. Multi-hit time resolution is assessed via the "even-odd" method, improving average resolution to $\sigma_{t_{e^+},pTC} = 43\text{ ps}$ by combining results from different hit groups. Efficiency of pTC was studied with MC simulation, yielding a total detection efficiency of $\epsilon_{e^+,pTC} = (91 \pm 2)\%$, considering factors like geometric acceptance and scattering effects on endcaps.

7.4 Trigger and DAQ

7.5 Beam and target

The beamlines at PSI were described in 1.5. The beamline delivering μ^+ to MEG II, in particular, is the $\pi E5$ line, shown in Fig. 7.9. The design, tuning, and deep understanding of this line play a key role in the success of the MEG experiment. Here we will describe the beamline, outline the key elements, and the related simulations. We will then describe the MEG II target, with some detail on the way to take into account its deformations during the analysis.

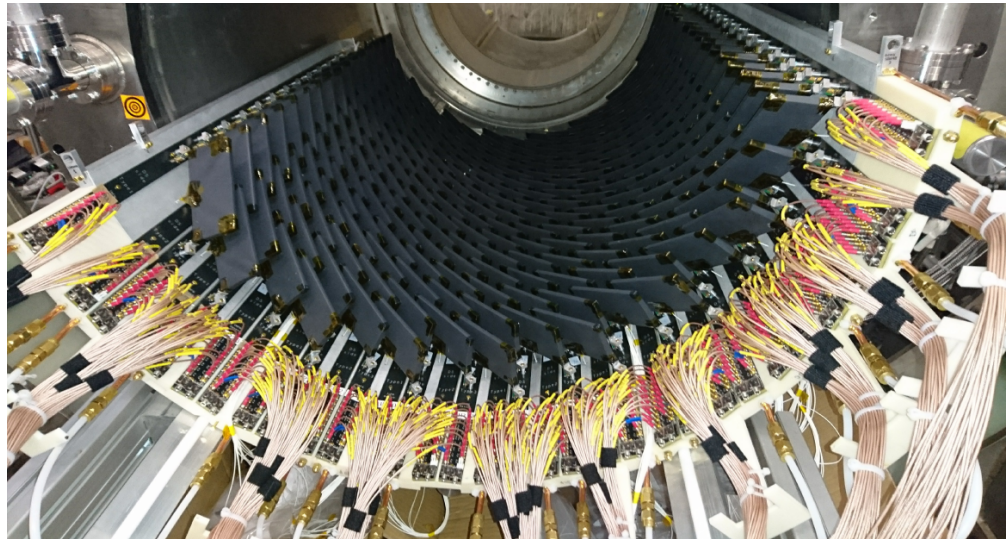
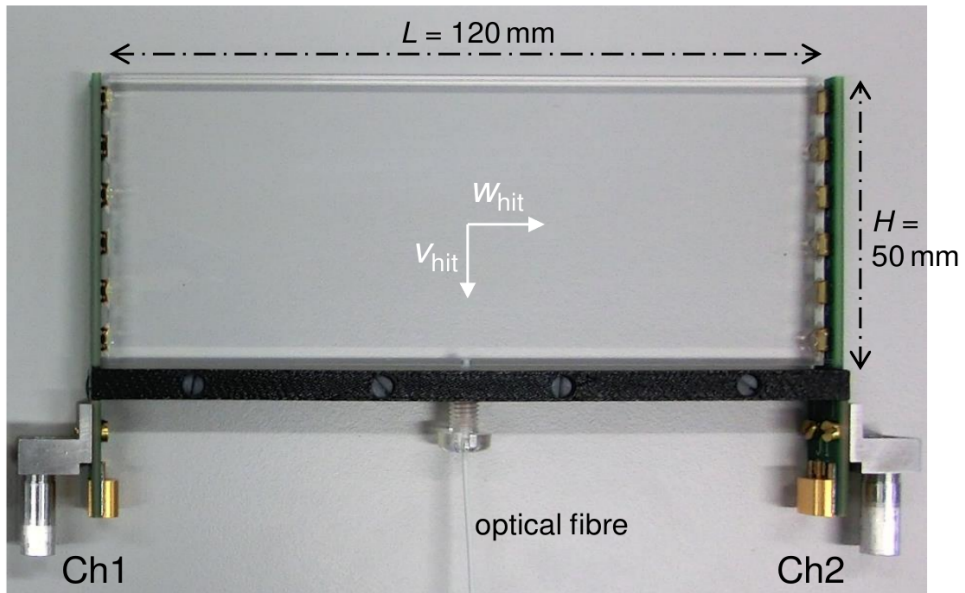
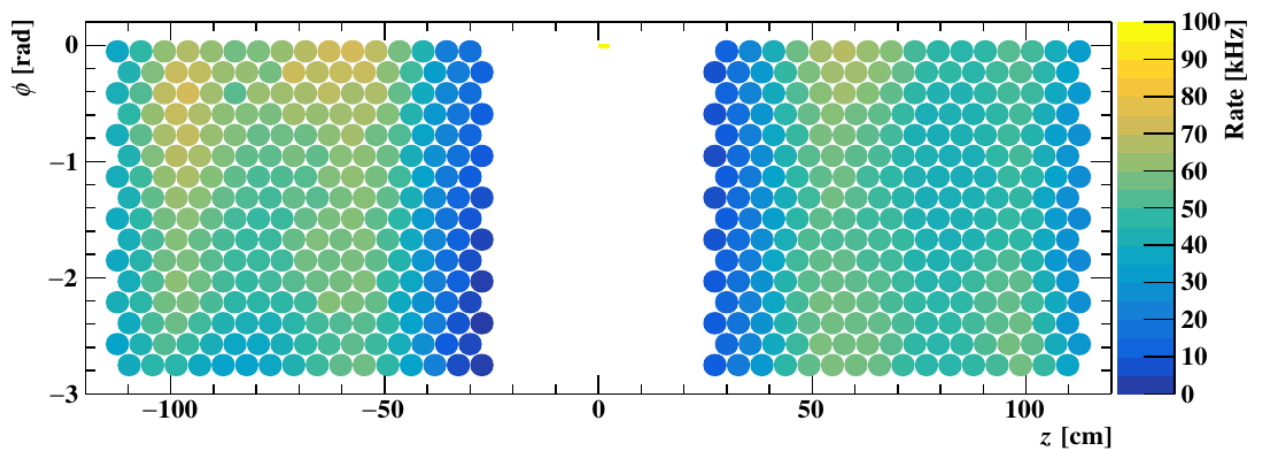


Fig. 7.6

Fig. 7.7: A pTC tile: $120 \times 40/50 \times 5 \text{ mm}^3$ of BC422® read by arrays of 6 AdvanSiD $3 \times 3 \text{ mm}$ SiPM.Fig. 7.8: Hit rates map of the pTC at $R_\mu = 5 \times 10^7 \mu/\text{s}$ during the 2022 run. Each circle indicates a counter.

7.5.1 $\pi E5$

This beam-line has actually two possible configurations: this will allow the area to be shared between MEG II and Mu3e. As already illustrated, the surface muons delivered by this beamline are produced for the decay of the pions generated as secondary beams from the HIPA proton beam. On top of muons, pions, and positrons also are transported by the beamline. We will briefly describe the elements of $\pi E5$ (COBRA has been already described).

- AHSW41 dipole: Captures the pions and muons in the backward direction and defines the momentum acceptance of the beamline.
- Straight section: Quadrupoles (QSF4*), sextupoles (HSC4*) and three slits (FS41–42–43) shape the beam. FS41 In particular is used to reduce the beam intensity and momentum spread.
- AST41 dipole: This element is used to define in which channel the beam is sent. "Z" channel for MEG II and "U" channel for (the upcoming) Mu3e.
- Separator: The beam arrives in a Wien filter via Triplet I and a quadrupole triplet. Te aim is to separate the muons from pions and positrons.
- Triplet II at a collimator: This pair focuses the beam and cuts the tails.
- BTS: This Beam Transport Solenoid contains a 300 μm thick Mylar[®] moderator.
- A 190 μm Mylar[®] window separates the beampipe from the He atmosphere in COBRA.
- COBRA: The design choice for this element was previously illustrated (7.3.1). The behavior of the beam inside this element is quite tricky to simulate consistently.

Although not one of my tasks, I helped during some of the beam tuning done during these last years. Aside from the beginning of the run, these elements are tuned also when there is a major change in the main proton beam, often related to the overall current of incoming particles. Another tune is done at the end of the year to change the beam from μ^+ to π , necessary for the CEX.

Beam profile In Fig. 7.10 is shown a typical beam profile at COBRA center: The beam is in $x_b = (0.0 \pm 0.5)$ mm, $y_b = (-0.8 \pm 0.5)$ mm with standard deviations $\sigma_x = (11.35 \pm 0.50)$ mm and $\sigma_y = (11.36 \pm 0.50)$ mm. This beam was measured with slits such as the stopped muon rate was $R_\mu = 5.3 \times 10^7 \mu/\text{s}$ at the primary proton beam current $I_p = 2.2 \text{ mA}$. Similar profiles were achieved in the range $R_\mu = (2 \div 5) \times 10^7 \mu/\text{s}$. The measurements on the stopped muon rate are evaluated using the stopping efficiency extracted by simulations (89%) and are affected by a 5% uncertainty due to the variations of the proton beam position on Target E.

7.5.2 Simulations

As introduced in the previous section, the understanding of the beam behavior is a key aspect of the experiment. The beamline itself was developed using TRANSPORT, a beam optics simulation program. The model was later implemented in G4BEAMLINE². The reason to have a physics-based simulation on top of the optics simulation is quite obvious: optics programs cannot simulate interaction with materials and all the physical processes taking place in a beamline.

G4BEAMLINE Being based on GEANT4, this program is a flexible and extensible framework for implementing complex simulations of particle interactions, including electromagnetic and

²G4BEAMLINE is a simulation program for particle physics based on GEANT4 and can be found [here](#).

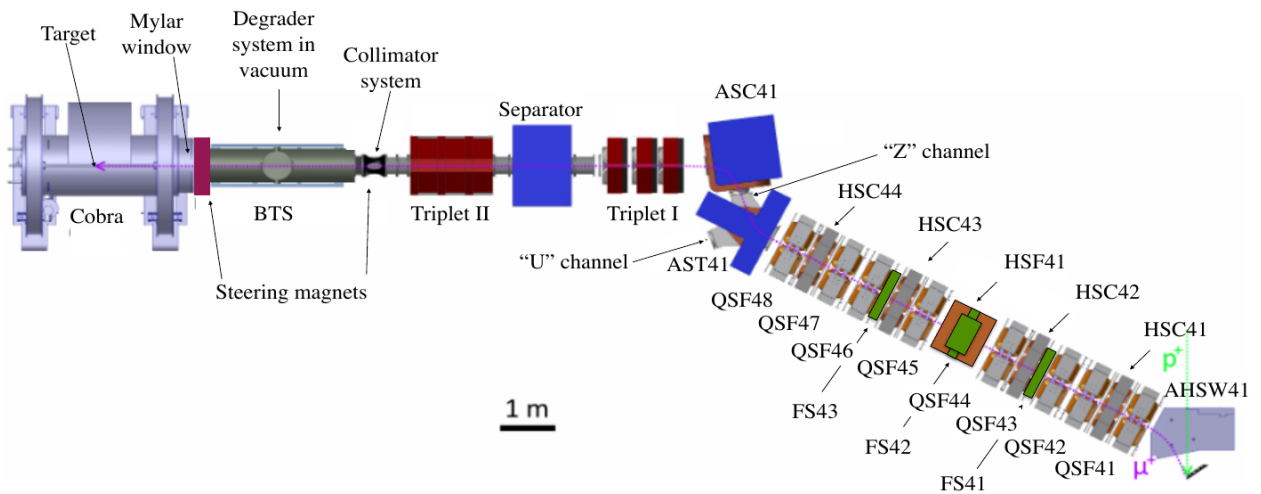


Fig. 7.9: Detail sketch of the $\pi E5$ beamline at PSI.

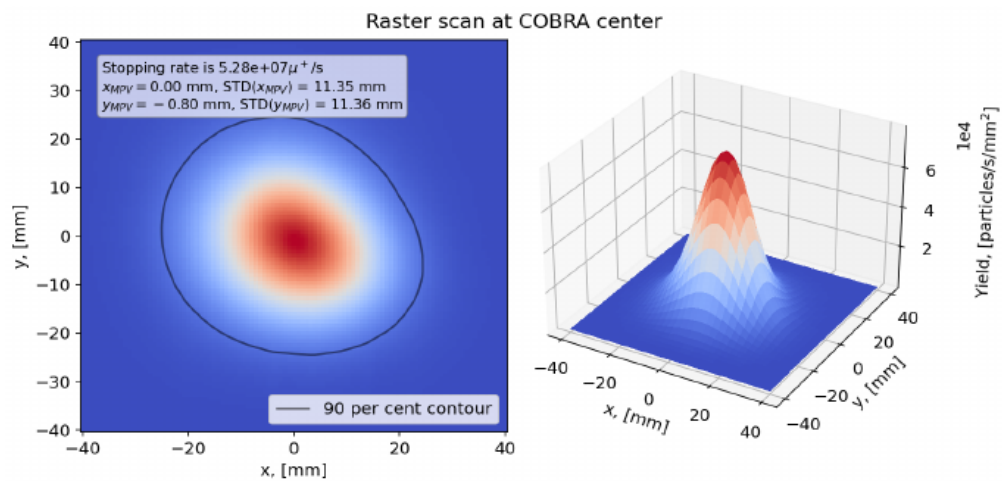


Fig. 7.10: Beam profile at COBRA center for a stopped muon rate of $R_\mu = 5.3 \times 10^7 \mu/\text{s}$ at $I_p = 2.2 \text{ mA}$.

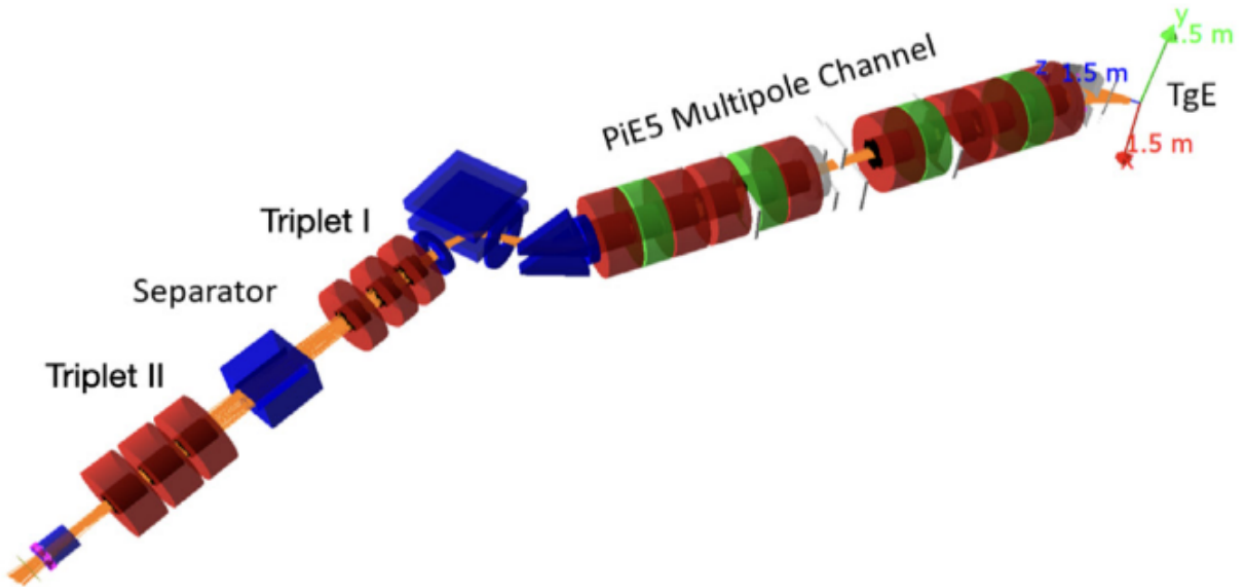


Fig. 7.11: G4BEAMLINE simulation of few tracks (orange lines) in the $\pi E5$ beamline. It's possible to recognize the elements discussed previously and showed in Fig 7.9.

hadronic processes, decay processes, and tracking in magnetic fields. Just like GEANT4, the simulation is run particle by particle and *step-based*. This means that at every interaction physical models are used to update the particle state and generate necessary secondary particles. The major extensions in G4BEAMLINE are predefined beamline elements, beam generators, and some optic tools to study the performance of the beamline. An example of particle tracking in this program is shown in Fig. 7.11. In the last years this simulation has been updated and developed by Giovanni Dal Maso to extract the best possible understanding of the stopped muon rate R_μ .

MAD-X During 2022/2023 Luca Biasia, a Master student in Pisa, developed a MAD-X³ simulation to describe the $\pi E5$ line and cross-validate the results obtained using G4BEAMLINE and to start the transition from TRANSPORT to MAD-X. My contribution to this simulation was only partial: I provided Luca with some working MAD-X examples, developed while attending the JUAS, and some initial help for him to start playing with this simulation framework. After this initial ‘starting kit’, Giovanni Dal Maso was the one overseeing the development while I only followed the updates and gave feedback or suggestions.

After a comparison with data and G4BEAMLINE some discrepancies arose and, after many iterations, they were associated with the description of the fringing fields of the components in MAD-X. The solution adopted was to slice the field maps in thin layers and define many thin ‘MAD-X elements’. A comparison of the results from QSK41 to COBRA center is shown in Fig. 7.12. During the beam tuning in June 2023, this simulation was crosschecked: after measuring the beam spot at COBRA center the currents of the magnets were chosen with MAD-X to obtain a different beam shape. The measurement was consistent with the resulting simulation. This was a great achievement and, moving forward, this tool is going to play a key role during the beam tuning.

³MAD-X is a general-purpose tool for charged-particle optics design and can be found [here](#).

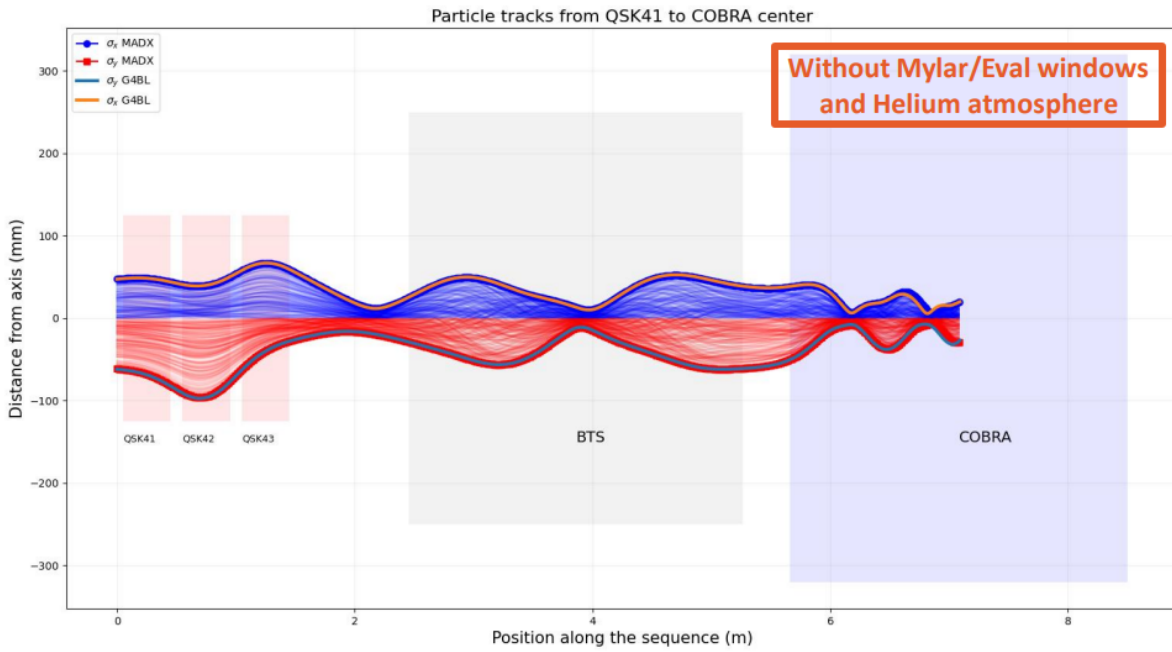


Fig. 7.12: Comparison of the results from the G4BEAMLINE and MAD-X simulations for $\pi E5$. While the agreement is very good for most of the beamline, there is some difference inside COBRA. This is due to the difficulty in describing the highly ‘non-standard’ magnet. Given MAD-X has no particle interaction, the comparison is fair only when removing all materials from the beamline in the G4BEAMLINE simulation.

7.5.3 MEG II target

The aim of the target is to stop μ^+ at COBRA center while minimizing the interaction of the secondary particles produced. The knowledge of the position of the target and planarity are key components in evaluating the systematic errors on the reconstructed vertex position. After in-depth studies, the BC400 scintillating plastic was selected as the material for the target. The shape is a ellipse of 270 mm \times 66 mm and 170 μm thick, with a maximum variation of 20 μm . The target is inclined such as the normal of its surface creates a $(75.0 \pm 0.1)^\circ$ angle with the beam.

Deformation and pictures In order to identify the $\mu^+ \rightarrow e^+\gamma$ process, it is necessary to measure the angles (ϕ_e, θ_e) at the target, back-propagating the reconstructed tracks. The resolution on these variables is ~ 7 mrad, but a simple displacement of 500 μm of the target propagates as systematics of ≥ 4 mrad on ϕ_e . For this reason, the collaboration developed three different ways of keeping these systematics under control:

- A yearly optical survey to measure the position inside COBRA.
- Fiducial holes in the target: This allows to study the position of the target reconstructing the position of the vertices for many events, but it requires months of data.
- Photogrammetric survey of a dot pattern on the target itself.

While the first two were used already in MEG, the third was developed for the upgraded MEG II. A picture of the target is in Fig. 7.13, where the dot pattern is clearly visible. Two different CMOS cameras are used to take pictures of the target and two different methods are then employed to study the sequence of pictures. The position of the center of the target is described in the MEG II coordinate system, while the deformation is accounted for differently by the two methods:

- In the first method, χ^2 is evaluated between the measured and expected dot positions. The

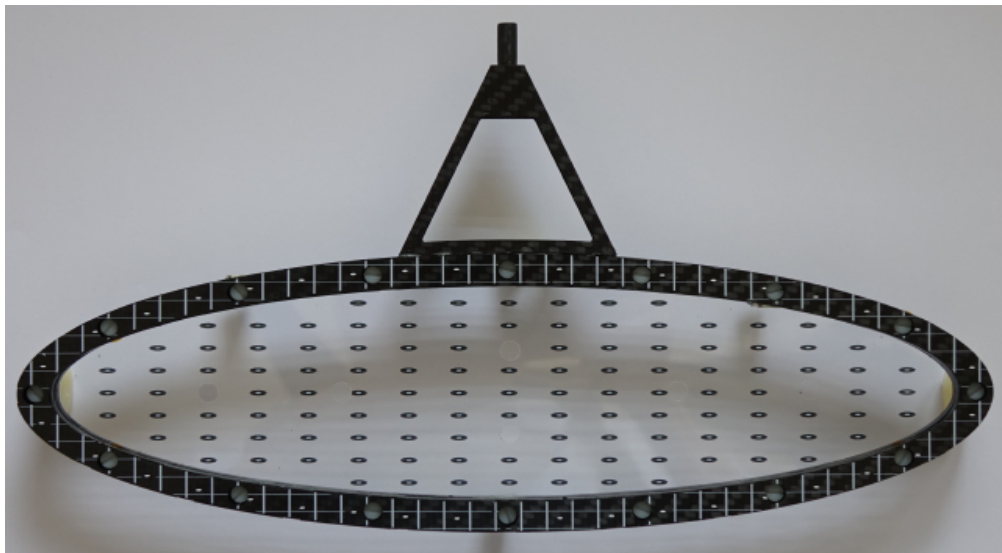


Fig. 7.13: Picture of the BC400 target. Clearly visible is the dot pattern on both the target and carbon fiber frame. Six holes, admittedly less visible, are located on the axes of the ellipse.

expected positions depend on the position of the target, the deformation (parametrized with Zernike⁴ polynomials), and the optical parameters of the system.

- The second method minimizes the χ^2 for the observed and measured 2D positions of the dots on the camera plane. Clearly, the optical projection on this plane is the cardinal element.

These two methods have been proven to be compatible within 100 μm .

7.6 Cockcroft–Walton

In addition to the muon beamline, MEG II has a Cockcroft–Walton proton accelerator. After the description of the machine, we will highlight the use of this accelerator by the collaboration (calibrations of the XEC and exotic searches) and the recent maintenance. One of my main tasks during this Ph.D. has been the usage of this machine, so I was quite fortunate to be able to shadow the expert during the maintenance.

7.6.1 Description of the machine

The accelerator is a single-stage in-line singletron produced by HVEM. This machine is a compact Cockcroft–Walton with a terminal voltage of 0.1 \div 1.0 MV and a proton current up to 100 mA.

Source The RF ion source is a bottle of gas that is excited by an RF oscillator. The electrons in the gas are excited and, because of the collisions with the neutral gas particles, cause ionization. The plasma produced is confined with an axial magnetic field and serves as the source of positive ions, which are extracted by applying a DC electric field. A schematic of the working principle of the RF ion source is shown in Fig. 7.15

⁴Zernike polynomials are a set of orthogonal functions commonly used in optics and image analysis (see [Wikipedia](#)).

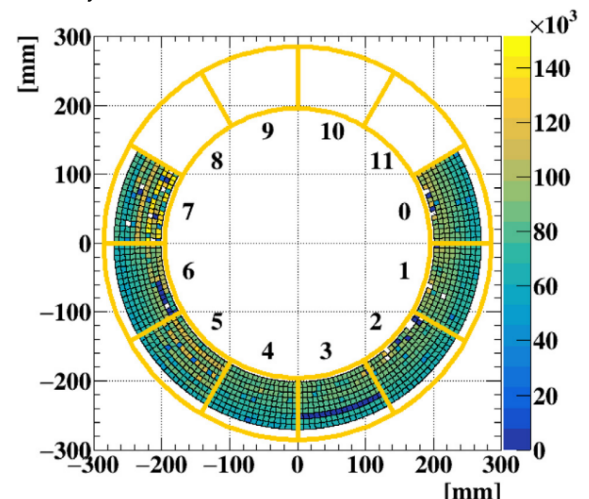
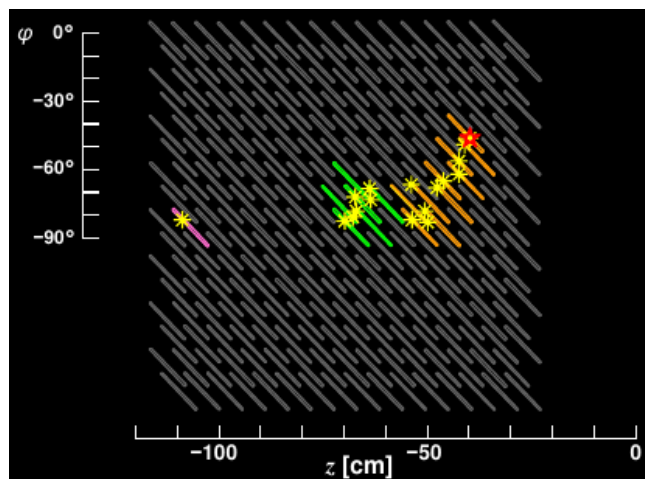
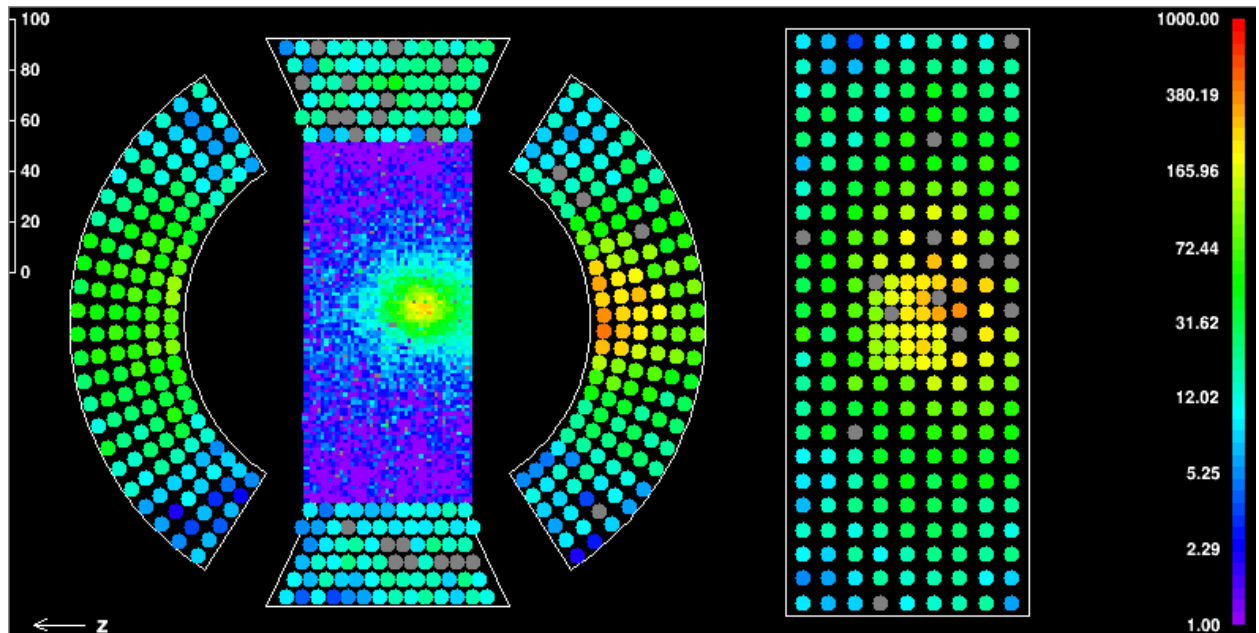


Fig. 7.14

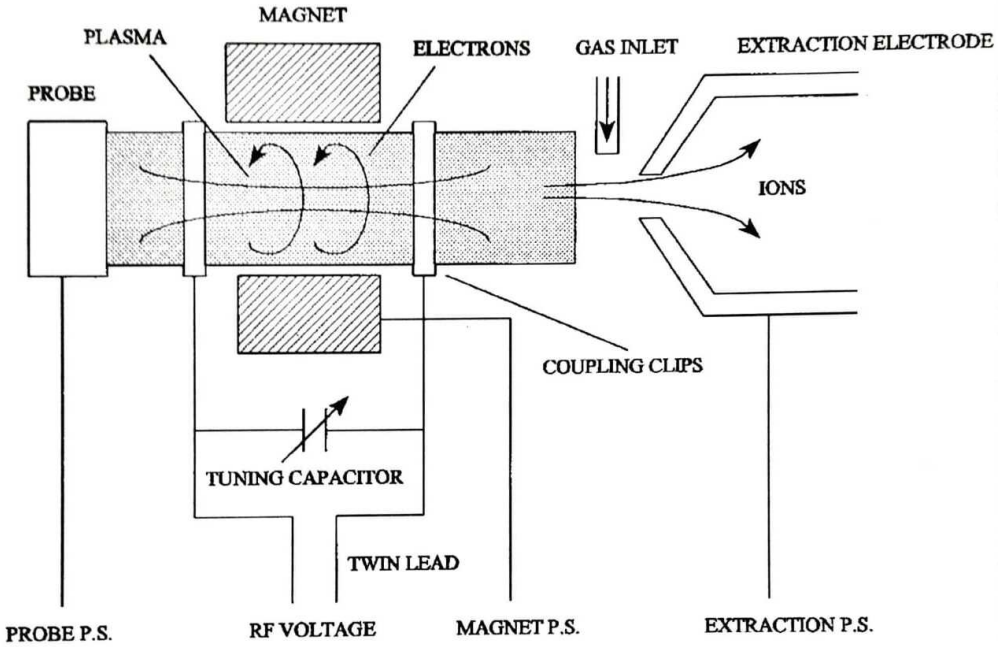


Fig. 7.15: Sketch of the ion source of the CW.

CW-Circuit The high-voltage multiplier and rectifier stack, together with the RF driver and HV control and stabilizing system, is one of the core sections of the machine. It is located in the main pressure tank, while the RF resonance coils are in a separate SF_6 filled tank and the RF driver in a separate cabinet. This gas is often used as a gaseous dielectric medium because of its high dielectric strength, the result of the gas's high electronegativity⁵ and density. In the case of an arc, SF_6 can break down in different ways but most of the decomposition products tend to quickly re-form SF_6 , a process termed *self-healing*. Arcing or corona can also produce disulfur decafluoride (S_2F_{10}), a highly toxic gas, which is the reason extra care is needed when opening such a system. This stack is a parallel-fed CW power supply that consists of a series of high voltage rectifiers and capacitive coupling *corona* rings. The power is fed via an RF driver capacitive coupled. A sketch of the inner structure of a rectifier assembly (*ass'y*) is shown in Fig. 7.16b while in Fig. 7.23b is clearly visible the way the ass'ys are mounted.

Driver The driver, as the name suggests, is the circuit that feeds the voltage/power to the whole system. In between the driver and the CW stack of rectifiers' ass'ys a resonant circuit is used to amplify the output of the driver. The power is fed to this resonant circuit in phase with the oscillating current. Keeping the frequency at resonance, the driver controls the terminal voltage adjusting the pulse width. A block diagram of the driver is shown in Fig. 7.17

Start-frequency The system can operate only at resonance and this frequency f_{res} is defined by the coil and dynodes. During start-up, the system starts at f_{start} higher than the resonance and then lowers it until the resonance is found. A parasitic frequency f_{par} , with $f_{par} > f_{res}$, is also present. At this frequency, the driver oscillates at a higher frequency, and no power is transferred to the terminal. To avoid the higher frequency, a tuning is needed so that $f_{par} > f_{start} > f_{res}$.

⁵Electronegativity is a measure of the attraction of an atom for bonding electrons in molecules compared to that of other atoms: large values indicate a stronger attraction and it increases from left to right across the periodic table.

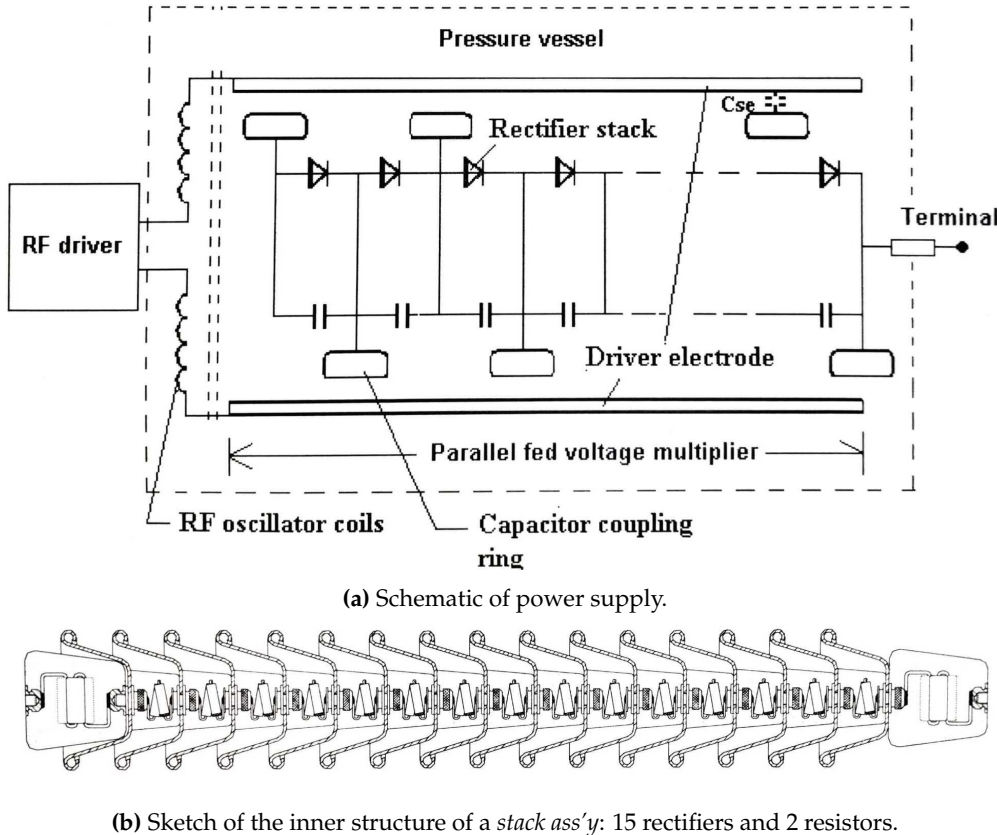


Fig. 7.16: The first schematic (a) shows the CW circuit and the capacitive coupling to the RF driver while the second (b) shows the internal structure of a rectifier stack (*stack ass'y*).

Q-factor In the RF resonance circuit high amounts of ‘blind power’ can be present (up to 1 MW). The quality factor (Q-factor) of the RF resonance circuit is the ratio of blind to dissipated power. E.g. for a blind power of 1 MW and a Q-factor of 1000 the transformer coil dissipates 1 kW of heat. If this factor is not high enough the dissipated power is too high and will prevent the driver from operating correctly. The Q-factor is measured using a function generator and looking at the relative phase and amplitude of voltage in two points of the accelerator’s RF resonance circuit. A sketch of the measurement is shown in Fig. 7.18a. The system is at resonance when there is no relative phase between V_1 and V_2 , and the value of V_1/V_2 is used to evaluate the Q-factor:

$$Q = Z_{coil}/R_{loss} = 2\pi f_{req} I_{coil} (V_1/V_2 - 1)/R_l \approx 43.9 \times f_{res} [\text{kHz}] \times (V_1/V_2 - 1) \quad (7.2)$$

7.6.2 Usage

This machine is used 3 times a week, together with a ${}^7\text{Li}$ target, to produce the 17.6 MeV line of the ${}^7\text{Li}(p,\gamma){}^8\text{Be}$ to calibrate the XEC. This process was already outlined in Sec. 7.2.3. On top of taking care of these calibrations⁶ I ironed out the procedure and reworked the documentation.

X17 The protons coming from the CW have been mainly used for the calibration of the XEC detector, but also to perform a parasitic measurement: the search for the X17 anomaly. This search,

⁶This 3 times a week task was shared between 3 people, me included.

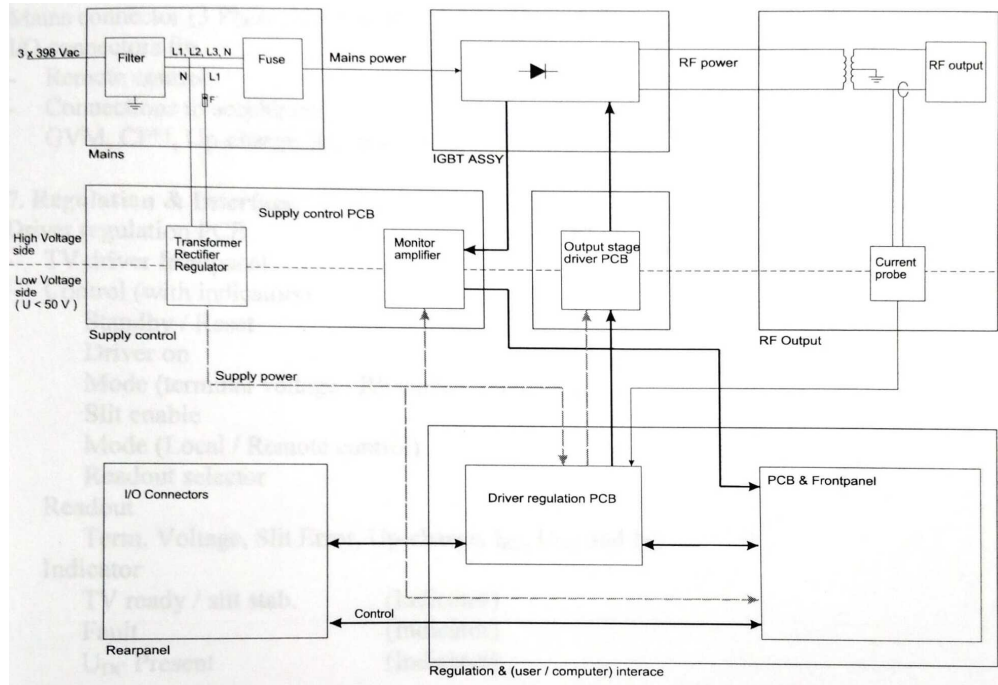


Fig. 7.17: Block diagram of the driver

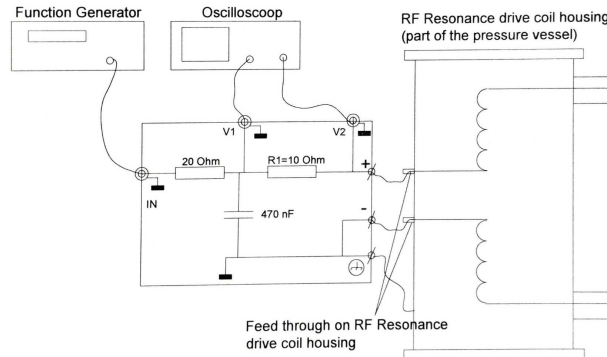
done in 2021-2023, will be extensively discussed in Ch. 9 but we wanted to underline here the key role that the CW machine has played in this parasitic search for exotic physics.

7.6.3 CW issues and maintenance

By the end of 2020, the CW started having some minor problems: the machine was running fine but the time required to switch it on kept growing longer. While the whole procedure would normally take ~ 15 min the time required exceeded the hour. We also noticed the machine was getting unstable when running near the maximum voltage at 1 MV. Following this behavior, an intense exchange with the HVEE company started and we performed many different tests on both the software and hardware sides.

Hot Fix We performed a measurement of the Q-factor of the machine using Eq. 7.2, shown in Fig. 7.18b. The value found was a factor $\sim 2k$ lower than expected and the position of the resonance frequency was shifted from the design value. For more information on the functioning of the machine and the Q-factor see Sec. 7.6.1. We adjusted the frequency at which the machine starts when turning ON. This solved the delay problem but didn't recover the maximum voltage. The machine was now starting quickly but working in a stable configuration only up to half of the nominal maximum voltage. As explained in the previous paragraph this was not a problem for the ‘usual’ calibrations but was a worrying sign on the health of the machine and would have prevented the CEX. At this point, an expert from HVEE was sent to inspect the machine.

Maintenance After running some checks opening the CW was deemed necessary and for this reason, we removed the SF₆ contained in the main tank. After the extraction of the CW, we inspected and measured all the elements, removing also some of the *corona rings* for easier inspec-



(a) Sketch of the circuit to measure the Q-factor.

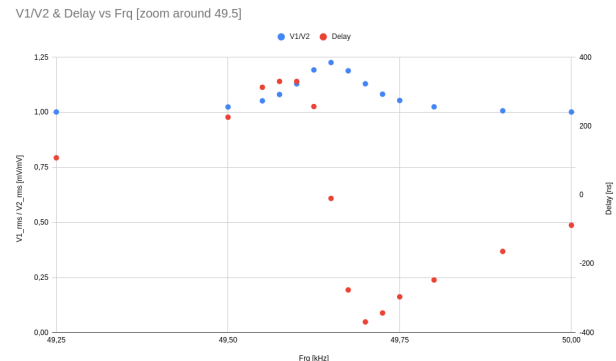
(b) Example of measurement of the Q-factor: in red the delay while in blue the fraction V_1/V_2 .

Fig. 7.18: The Q-factor is the ratio of blind to dissipated power. Via this number is possible to evaluate the energy dissipated as heat running the machine. If it is too low the machine cannot operate correctly.

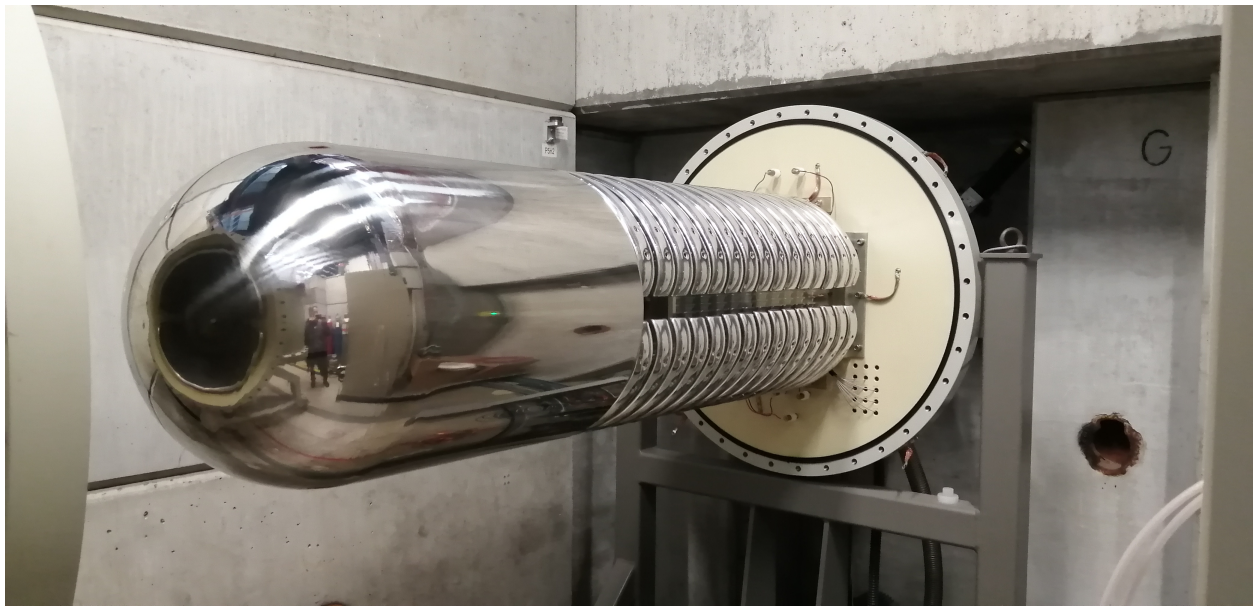


Fig. 7.19: View of the CW after the extraction from the external volume. This volume contains SF₆ which is used as a gaseous dielectric medium and needs to be evacuated before the extraction.

tion. We found signs of arcing on one of the *rectifier ass'y*. After the substitution of this element⁷, the machine was closed again, filled with SF₆, and tested again. This whole process is shown in the pictures in Fig. 7.23. Unfortunately, the faulty behavior persisted and we noticed sparks in the main volume. After re-opening we found burning marks on the rectifier ass'y next to the exchanged one. We then realized that both were damaged but the first was functioning as a 'bridge', preventing the second from being completely destroyed. After the substitution of the second and the tuning of the machine, we finally recovered its full functionality: quick switching ON and stable operation in the full range of voltages. 7.24.

⁷The rectifier ass'y are stacks of alternated diodes and aluminum capacitors capped by two resistors. We could re-use the capacitors, after careful cleaning, while resistors and diodes were too badly damaged. The process of refurbishing is shown in Fig. 7.24

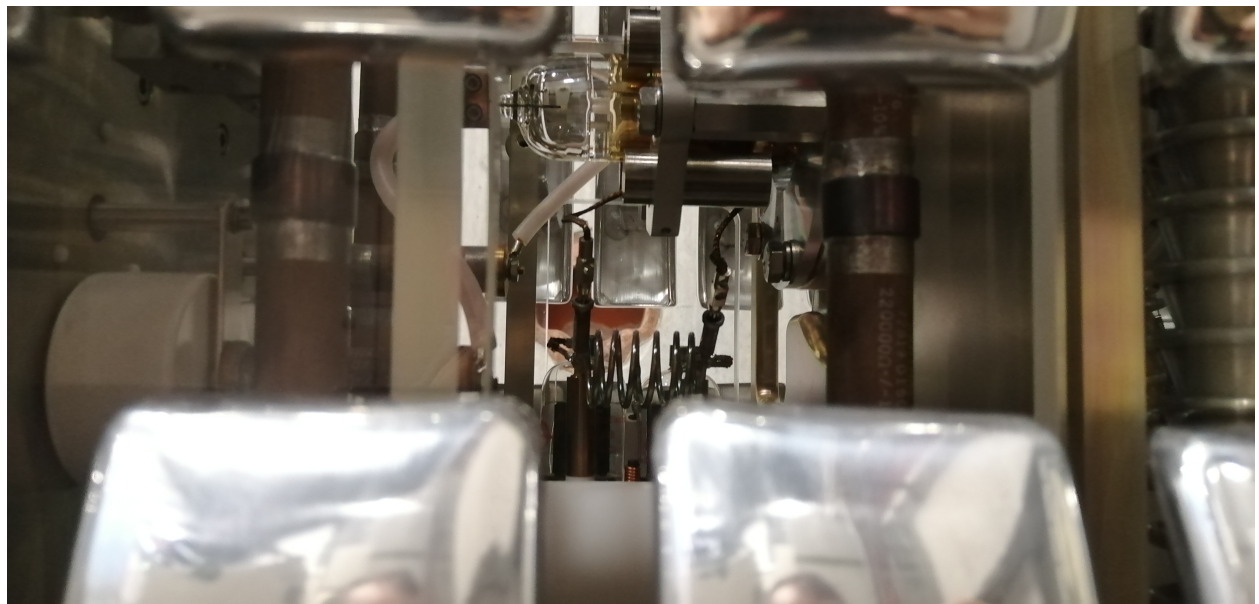


Fig. 7.20: View of the source of the CW machine.



Fig. 7.21: Top view of the CW after the removal of a few *corona rings*. Here we can see all the elements of a CW circuit: red - the resistors on top; metallic rings on the central tube - the capacitors; blue and metallic cups - the resistance and capacitors of the rectifiers, which run vertically.

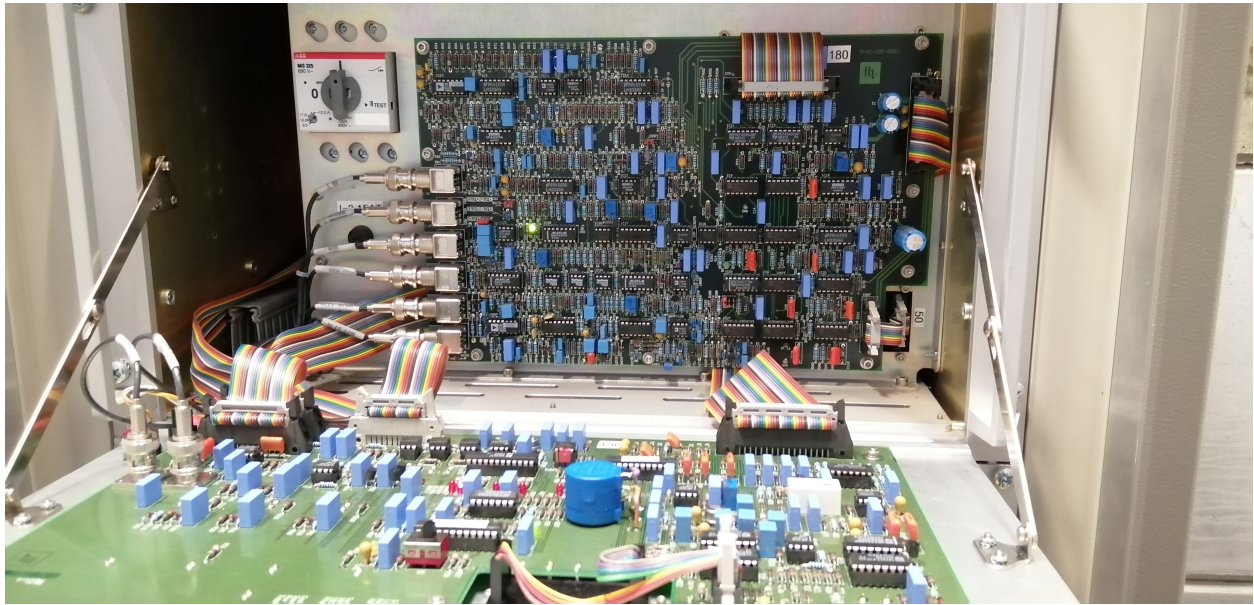
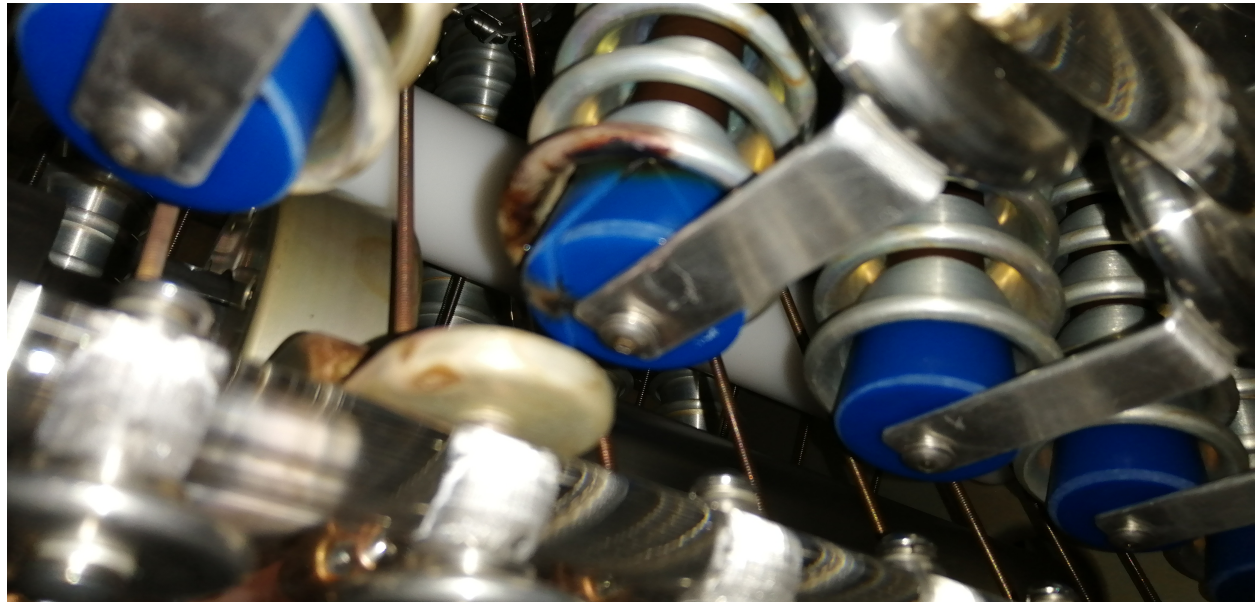


Fig. 7.22: Picture of the control panel for the CW machine.

7.7 Conclusions

In this (very dense) chapter we went through the description of two key elements of the work I have done during these three years: the MEG II apparatus and the Cockcroft–Walton. While I took no part in the design of either, in these years I spent a lot of time ‘hands-on’ on many subsystems of the MEG II apparatus: calibrations, tuning, and fixes of various types. On the other side, the CW functioning has been one of my main tasks. The unfortunate hiccup with it gave me the additional unforeseen opportunity to assist the HVEE technician in testing and fixing the machine, which was an extremely interesting and instructive experience.



(a) Discovery of the burning marks on two rectifiers. The reflectivity was a challenge in taking the picture.



(b) Extraction of the broken rectifiers.



(c) Broken rectifier ass'y after the extraction: clearly visible is the burned blue resistor at the top.

Fig. 7.23: After close inspection we found burning marks on two rectifiers' ass'y (7.23a). These were removed (7.23b) and carefully inspected (7.23c). The only salvageable part of the rectifiers were the aluminum capacitors, which we cleaned from burning residuals, while all diodes and resistors had to be exchanged.



(a) Picture of the burning marks on the end resistors of the rectifier ass'y.



(b) Assembly of one of the new stack: black - resistors; brown - diodes; metallic - aluminum capacitors.



(c) One of the finished new rectifiers.

Fig. 7.24: The rectifiers are made of three elements: diodes; aluminum capacitors; resistors (7.24a). Only the capacitors were salvageable: we re-assembled the rectifiers with new diodes and resistors (7.24b; 7.24c).

Bibliography on MEG II

- [1] A.M. Baldini et al. “Search for the lepton flavour violating decay $\mu^+ \rightarrow e^+ \gamma$ with the full dataset of the MEG experiment”. In: *Eur. Phys. J. C* 76.8 (2016), p. 434. DOI: 10.1140/epjc/s10052-016-4271-x. arXiv: 1605.05081 [hep-ex].
- [2] Bastiano Vitali. “In situ monitoring of the stopped muon flux at Mu2e”. MA thesis. Pisa U., 2020. DOI: 10.2172/1764143.

Chapter 8

Liquid Hydrogen target

In this chapter the Charge EXchange reaction, a calibration for the liquid XEnon Calorimeter, will be discussed and an in-depth description of the associated Liquid Hydrogen Target is given. Data taking, analysis, performances, and the different modifications will be also discussed. This target was designed in 2020 to overcome some limitations of the previous and in the last two years went through some heavy re-development. This calibration is cardinal for the correct functioning of the key subdetector of the MEG II experiment. It was one of the main tasks in my involvement in this experiment and it absorbed a sizable portion of my time and effort.

8.1 Charge EXchange reaction

As already discussed, the $\mu \rightarrow e\gamma$ process searched by MEG leads to a monochromatic photon at 53.2 MeV. We saw in Sec. 7.6 the XEC calibration which is performed three times a week. Unfortunately, while the frequent calibrations are great for the time dependencies, the photon produced by the Li is at lower energy than the signal. To calibrate the calorimeter near the signal region, the Charge EXchange reaction is exploited. The Charge EXchange (CEX) process $\pi^- p \rightarrow \pi^0 n$; $\pi^0 \rightarrow \gamma\gamma$ produces γ with a flat distribution in the interval [54.9, 82.9] MeV. Extremal values are reached for photons emitted back to back. Thus, a signal-like photon can be tagged by detecting a high-energy photon in the opposite direction. The tagging is performed with a BGO detector which can be positioned (steps of 30 cm in \hat{z} and 16 deg in $\hat{\phi}$) opposite to specific patches of the XEC. The requirement $\Delta E/E < 1\%$ translates to $\Delta\theta_{\gamma\gamma} < 5^\circ$. A sketch of the CEX measurements, a picture of the BGO detector, and its moving structure is shown in Fig. 8.1.

8.2 BGO

The BGO crystal already mentioned, and shown in Fig. 8.1b, is an auxiliary detector that plays a key role in two subjects of this thesis. For this reason, we will here describe it in some detail. BGO refers to $\text{Bi}_4\text{Ge}_3\text{O}_{12}$, a compound with a cubic crystal structure and often used as a scintillator. This detector is, in particular, a matrix 4x4 of $4\text{ cm} \times 4\text{ cm}$ crystals and mounted on a structure (see Fig. 8.1c) that allows it to translate and rotate around COBRA.

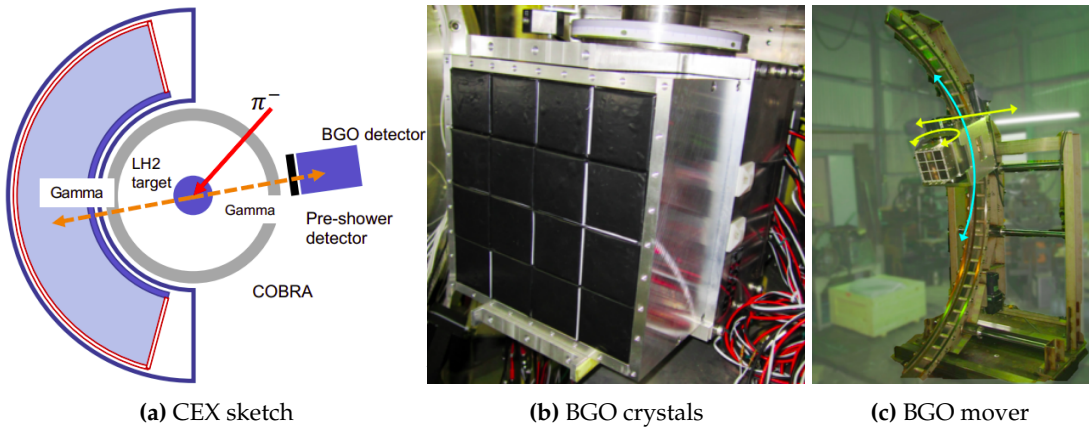


Fig. 8.1: Diagram of the CEX measurement, with the back-to-back photons configuration to define the XEC patch via the BGO positioning (8.1a) Picture of the BGO detector (8.1b) Picture of the BGO mover (8.1c).

8.3 LH2 target working principle

The details of the circuit and the operation changed on a yearly basis but it's worth do discuss the overall working principle before seeing the evolution of this system. Liquid Hydrogen was chosen to provide the protons needed for the CEX reaction. The incoming 70.6 MeV/c π^- are stopped in a cylindrical cell (60 mm diameter, 70 mm length) of 0.5 mm stainless steel containing liquid Hydrogen. This corresponds to $\sim 90\%$ stopping efficiency. The hydrogen has to be kept liquid ($T < 20.39$ K at 1 atm) and in the center of the COBRA magnet, requiring a cryogenic infrastructure to be inserted for 2 m. The target consists of four sub-systems:

- A “closed volume” hydrogen circuit, in which a 1.5 bar over-pressurized 100 ℓ buffer is connected to the target cell
- A copper rod (2 m in length and 2 cm in diameter): supported and cooled at one end with liquid helium flowing in a copper coil; holding the target cell at the other.
- Vacuum Insulation for the whole system
- A slow-control based on an SCS2000 [**midas**] controlling: temperatures, pressures, He flux, and the alarm system

The buffer volume for the gaseous hydrogen, as well as all the infrastructure and services, are kept outside the magnet. The circuit for the 2021 version is shown in Fig. 8.2 and, to increase the readability, the different sub-circuits are color-coded:

- Blue - Hydrogen is filled into the buffer from a cylinder, which gets then removed. The buffer itself is connected to the cell, the exhausting line, a vacuum pump, piezoresistive pressure transmitters and a Nitrogen bottle
- Red - The liquid He flux is obtained by pressurizing a Dewar with an He bottle. The He passes around the Cu rod and through a heater before entering the He recovery line
- Green - Insulation vacuum system
- Yellow - A nitrogen bottle is used for purging the hydrogen when emptying the buffer and kept connected for safety

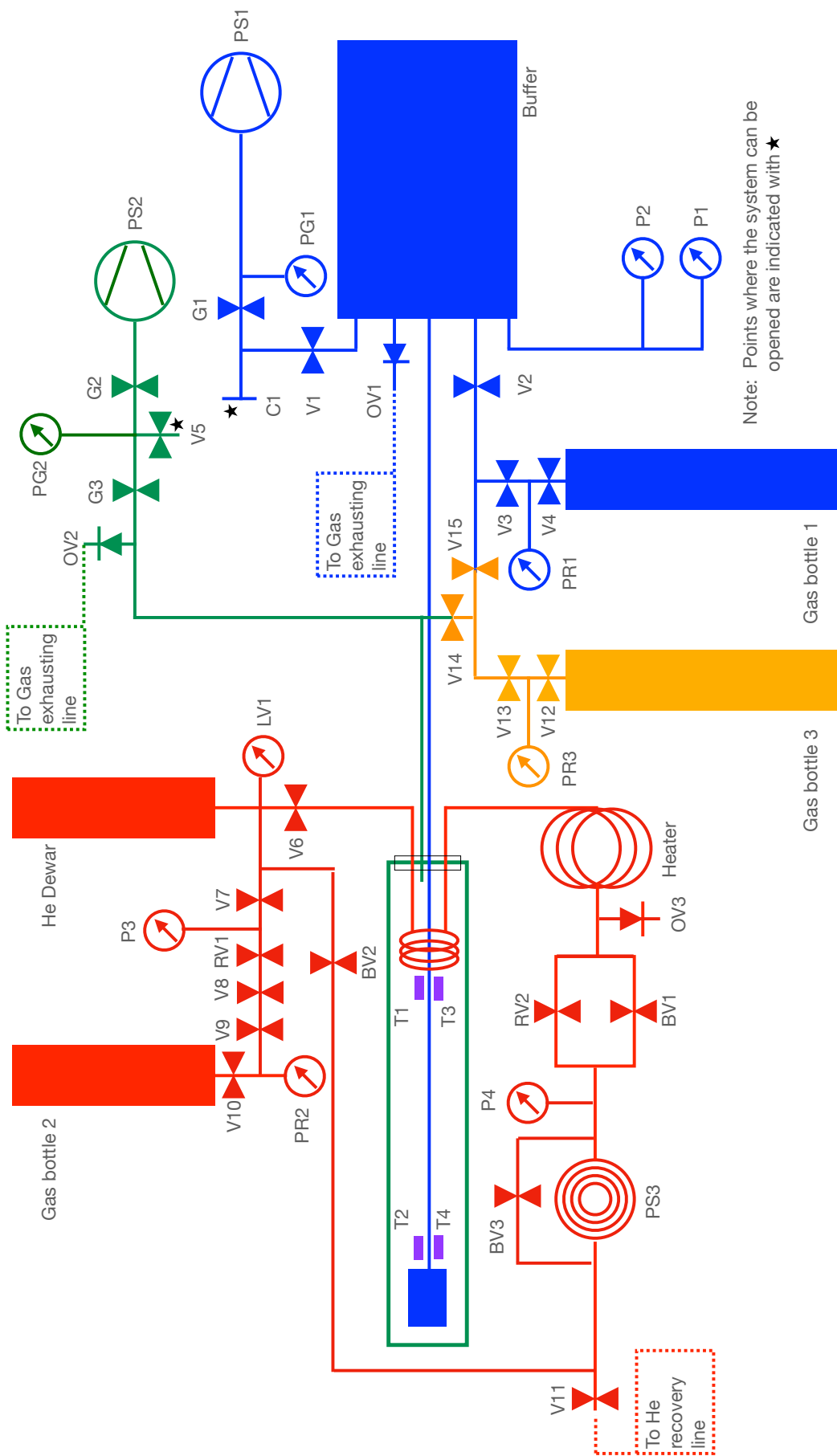


Fig. 8.2: Circuit of the LH2 target. To increase the readability of the scheme of the circuit, the different sub-circuits are color-coded:
Blue - Hydrogen; Red - Liquid Helium; Green - Insulation vacuum; Yellow - A nitrogen

8.3.1 Operation and control

The operation of the target itself is partially manual and partially controlled through a LabVIEW program which, for example, controls the read-out of the various sensors and the flux of the incoming He. A module SCS2000 allows to read the various sensors. There are two key indicators used to monitor the liquefaction process and stability of the system:

- Temperature sensors: resistors(later replaced by Lakeshore silicon diodes sensors) have been put in thermal contact with the Cu rod at both ends (two per side for redundancy). The readings of these elements allow us to monitor the cooling at the Cu coil and the cell.
- Hydrogen pressure: at room temperature, the hydrogen is set to 1.5 bar over-pressure. When the liquefaction starts the overall pressure is reduced and can be linked to the amount of liquid Hydrogen in the cell.

8.4 2021

I started my Ph.D in November 2020 but I joined the activities after the first year, in October 2021. For this reason, I did not participate in the development of the first iteration of the target and I joined directly the first tests before the data taking period. The status of the LH2 Target and the preliminary results of the 2021 CEX were presented at the 15th Pisa Meeting on Advanced Detectors [1].

8.4.1 Data taking

The data taking lasted roughly two weeks, during which CR runs and XEC calibrations were run while the target was cooling and liquefying. As soon as the level was sufficient the pion beam would be used for CEX data taking for a specific patch of the XEC. When the dewar needed to be exchanged, the data taking would be stopped and CR/calibrations would restart, waiting for the target to be sufficiently full to restart. In figure 8.3 is shown the history of the Hydrogen and Helium pressure at the dewar. Interesting features are:

- The decreasing parts of the blue plot are the liquefaction period: the Hydrogen pressure drops because of the phase change
- During liquefaction, some spikes can be seen: these are instances in which the system became unstable and liquefaction stopped
- The speed of cooling and liquefaction is always the same because the result of hardware choices;

Overall, CEX data could be collected when the target was considered ‘full enough’: below AAA bar, meaning 0 %. In the two weeks, this translates to efficiency of $\epsilon_{2021} \approx 0$. The efficiency for 2021 was lower than expected and the necessary statistic was not reached for every patch.



Fig. 8.3: Measured hydrogen pressure in the target and helium pressure in the dewar used for cooling during 2021 CEX data taking. Beam was ON when the target was considered ‘full enough’: below AAA bar, meaning 0 %. This translates to a time efficiency of $\varepsilon_{2021} \approx 0$. Unfortunately, the low efficiency prevented the collection of the necessary statistics for every patch of the XEC.

8.4.2 Data analysis

8.5 2022

8.5.1 Upgrades

He circuit

Cup

Shielding

8.5.2 Data taking

8.5.3 Data analysis

8.6 2023

Although the 2022 CEX campaign was much more successful than the previous one, the limitations of this design and the second iteration dictated a hectic schedule during data taking. The (somewhat risky) modification of the liquid hydrogen cup turned out to be a good improvement but there was still room for refinement. For this reason, we went back to the drawing board.

8.6.1 Upgrades

He circuit

Cup

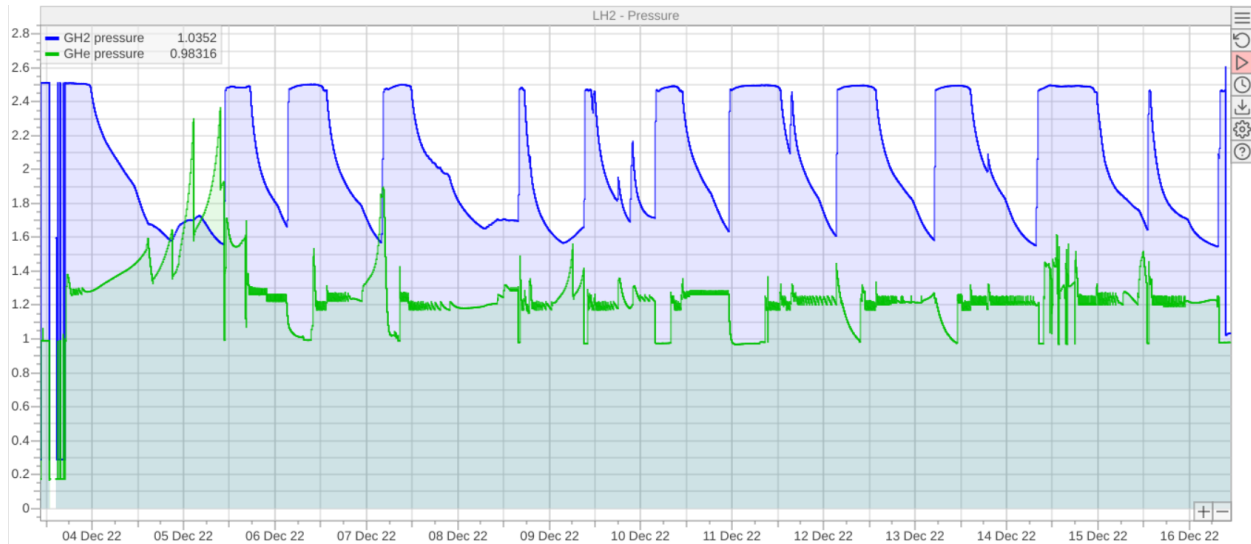


Fig. 8.4: Measured hydrogen pressure in the target and helium pressure in the dewar used for cooling during 2022 CEX data taking. Beam was ON when the target was considered ‘full enough’: below AAA bar, meaning 0 %. This translates to a time efficiency of $\varepsilon_{2022} \approx 0$ (against $\varepsilon_{2021} \approx 0$). The improvement in efficiency allowed us to collect the necessary statistics for every patch of the XEC.

Shielding

8.6.2 Data taking

8.6.3 Data analysis

8.7 Conclusions

Bibliography on LH₂

- [1] B. Vitali et al. "A liquid hydrogen target to fully characterize the new MEG II liquid xenon calorimeter". In: *Nucl. Instrum. Meth. A* 1049 (2023), p. 168020. DOI: 10.1016/j.nima.2023.168020.

Chapter 9

Search for X17

After the recent publications from the ATOMKI collaboration, the so-called X17 anomaly piqued the interest of the community. The flexibility of the MEG II apparatus allows for a variety of exotic searches and the collaboration deemed of interest searching for this anomaly in an uncorrelated way. The chapter starts with a recap of the previous searches and then moves to the description of this search in MEG II: setup used, simulations developed, data acquisition and data analysis.

9.1 ATOMKI and the X17 ‘anomaly’

The story of the Hungarian group and their result

9.2 X17 in MEG II

After reading with great interest the papers from ATOMKI, the MEG collaboration started evaluating if repeating this measurement was achievable with the MEG II apparatus. In 2022 the first data collection was performed but the time constraints, required to keep the main focus of the experiment on the $\mu \rightarrow \gamma e$ process, meant not all the necessary preparatory studies could be performed. The details of this first data-taking will be skipped and we will move directly to the second campaign, performed in 2023.

9.2.1 MC simulations

9.2.2 Magnetic field choice

The first step is to identify the magnetic field required. The geometry of the MEG II detector, in junction with the magnetic field, defines the acceptance of the produced particles. Given the nature of the COBRA magnet, the parameter here is the scaling of the magnetic field. Thorough simulations were run to optimize the scaling factor, finding the best compromise between the efficiency for signal and background reconstruction to be $B_{X17} = 0.15 \times B_{MEG}$. This value can be roughly estimated considering that a scale factor of 1 is optimized for positrons of 53 MeV while the pair produced by the X17 decay should be roughly at 8 MeV ($8/53 \approx 0.15$).

9.2.3 Target

The setup for the target is quite straightforward: a carbon fiber vacuum chamber is mounted at the tip of the insertion system of the CW bellows system; a mounting system holds different types of targets. The bellows system is the one used for XEC weekly calibrations and will be not discussed.

Vacuum and mechanical structure The thickness and dimensions of the carbon fiber vacuum chamber have been optimized via dedicated simulations for both integral structure and particle interaction. After receiving the carbon fiber the chamber was glued and tested for vacuum.

Lithium target The interesting process requires Lithium atoms but Lithium targets tend to be unstable. Among the options studied LiF and $\text{Li}_{3.6}\text{PO}_{3.4}\text{N}_{0.6}$ were the most promising. Looking back we now know that the spattering process behind the production of our targets resulted in a poorly characterized end-product. LiF targets were produced by INFN Legnaro while $\text{Li}_{3.6}\text{PO}_{3.4}\text{N}_{0.6}$ targets were produced at PSI.

9.3 Data acquisition

9.3.1 Beam tuning

The beam tuning was performed by substituting the end cap of the proton beam line with a transparent cap with a AAA crystal. The proton beam produces visible photons hitting the crystal so the beam position can be observed. Normally this operation would be done while the upstream side of COBRA is not closed, allowing the installation of a webcam that gives instant feedback on the beam position. This was not the case so we were forced to use the camera installed inside COBRA for MEG II target monitoring. This camera has some settings for *gain* and *aperture* but is controlled using a script in *ssh* and to view the picture first is necessary to move them locally, making the whole procedure somewhat cumbersome. Key aspects of the beam to be tuned were:

- Energy: This parameter is controlled by the *Terminal Voltage* of the CW.
- Focus: This parameter is controlled by the *Extraction Voltage* of the CW. Fig. 9.2 shows how the beam spot changes as a function of this parameter.
- Position: This parameter is controlled by the three dipoles of the CW beamline. The change of the position for different values of the dipoles at 500 keV is shown in Fig. 9.1.

After a careful scan of the three parameters, working points at different energies were chosen: the most relevant are the ones for 500 keV and 1080 keV. It is of interest to notice that 1080 keV is the balance between what was previously discussed and the limitations of the CW machine: a higher (~ 1100 keV) energy would be a better choice but the nominal upper limit of the machine is actually 1 MeV, meaning having it running stably at 1080 keV is already an achievement. To the best of our knowledge, the beam at COBRA center during the data-taking was Gaussian $(x, y) = 2, -2 \text{ mm}; (\sigma_x, \sigma_y) = 2, 2 \text{ mm}$.

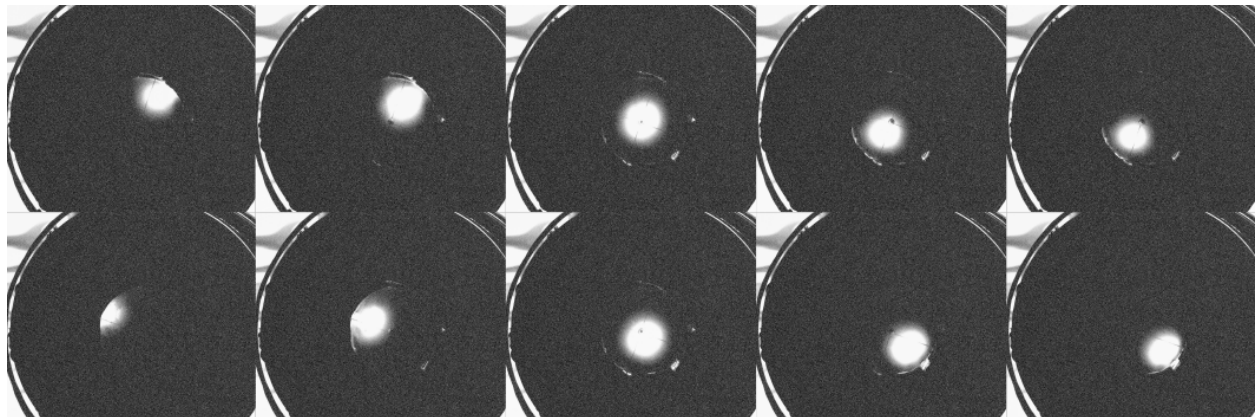


Fig. 9.1: Position of the proton beam at 500 keV when changing the current in the dipoles (the vertical dipole V and only one of the two horizontal dipoles H). In the first row, H is changing and the beam moves diagonally. In the second row, V moves the beam on the perpendicular diagonal.

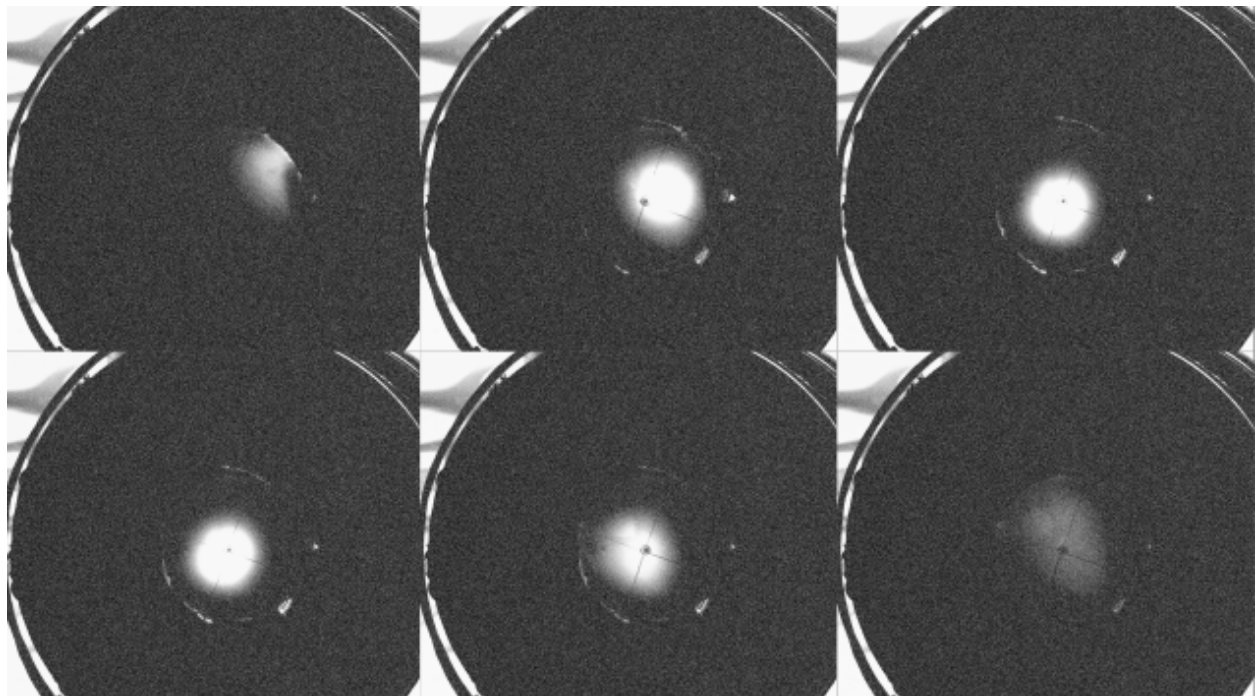


Fig. 9.2: Focus of the proton beam at 500 keV when changing the of the CW: values in the range 6 ÷ 15 keV. Is clearly visible for extreme values the beam barely reaches the crystal.

9.3.2 Asymmetry

9.3.3 Normalization

9.4 Data analysis

9.4.1 Pair reconstruction

B inversion

VerteXing

9.4.2 Asymmetry

BGO

XEC

9.4.3 Feldman-Cousin

Although the Feldman-Cousin approach is well-established in particle physics research, this was our first hands-on experience. After studying the relevant papers ([1][2]) and the internal notes of the collaboration we decided to develop a mock-up experiment to understand the framework necessary for a Feldman Cousin approach to data analysis. Given a measured sample and the probability density functions (PDFs) the framework we developed allows us to perform the analysis and obtain the confidence intervals. The full-blown X17 analysis was actually performed with the code already written for the MEG II analysis. This code was developed and improved upon over many years and was both more robust and flexible. Although it was an ‘academic exercise’, this effort made understanding the existing code and the underlying theory/structure an easier task. I contributed actively to this effort until we managed to have a running structure. Although I followed the whole procedure, the finalization of the mockup¹ and the transition to the MEG II code were done by Giovanni Dal Maso.

Likelihood This is an exercise to build confidence level belts based on Feldman-Cousins ranking using binned data. The data is synthetic and composed of an exponential background with a fixed slope and a Breit-Wigner with unknown mass and width. The data is binned. For such analysis, the likelihood can be written as:

$$\mathcal{L}(\mathbf{x}|\hat{\mathcal{N}}_S, \hat{\mathcal{N}}_{BK}, \hat{m}, \hat{\Gamma}) = \frac{\hat{\mathcal{N}}^{\hat{\mathcal{N}}} e^{-\hat{\mathcal{N}}}}{\hat{\mathcal{N}}!} \prod_{i=1}^m \left(\frac{\hat{N}_S}{\hat{\mathcal{N}}} \hat{\pi}_{S,i} + \frac{\hat{N}_{BK}}{\hat{\mathcal{N}}} \hat{\pi}_{BK,i} \right)^{\hat{\mathcal{N}}_i}, \quad \hat{\mathcal{N}} = \hat{\mathcal{N}}_S + \hat{\mathcal{N}}_{BK}, \quad \mathcal{N} = \mathcal{N}_S + \mathcal{N}_{BK}$$
(9.1)

Where \mathcal{N} is the number of measured events, $\hat{\mathcal{N}}$ is the center of the Poisson distribution and $\hat{\mathcal{N}}_i$ is the number of events in the i -th bin. The $\hat{\pi}_i$ variables are uniquely determined by the signal and background PDFs, and are the expected values of the fraction of events in the i -th bin.

¹The full description of the code will be here skipped but it can be found in the following git repository [🔗](#)

PDFs The signal PDF is defined as a Breit-Wigner:

$$\mathcal{S}(m|\hat{m}, \hat{\Gamma}) = \frac{k}{(m^2 - \hat{m}^2)^2 + \hat{m}^2 \hat{\Gamma}^2} \quad (9.2)$$

with:

$$k = \frac{2\sqrt{2}\hat{m}\hat{\Gamma}\gamma}{\pi\sqrt{\hat{m}^2 + \gamma}}, \quad \gamma = \sqrt{\hat{m}^2(\hat{m}^2 + \hat{\Gamma}^2)} \quad (9.3)$$

Given $\mathcal{S}(m|\hat{m}, \hat{\Gamma})$, it is possible to evaluate the $\hat{\pi}_{S,i}$:

$$\hat{\pi}_{S,i}(m_i) = \int_{m_i - \Delta m}^{m_i + \Delta m} \mathcal{S}(m'|\hat{m}, \hat{\Gamma}) dm' \quad (9.4)$$

with Δm being the bin width. The background PDF is defined as an exponential tail:

$$\mathcal{B}(m) = \lambda e^{-\lambda m} \quad (9.5)$$

with λ fixed. Given $\mathcal{B}(m)$, it is possible to evaluate the $\hat{\pi}_{BK,i}$:

$$\hat{\pi}_{BK,i}(m_i) = \int_{m_i - \Delta m}^{m_i + \Delta m} \mathcal{B}(m') dm' \quad (9.6)$$

with Δm being the bin width.

Toy MC framework

9.5 Results and conclusions

[3] [4] [5] [6] [7] [8] [9] [10] [11]

Bibliography on X17

- [1] Gary J. Feldman and Robert D. Cousins. "Unified approach to the classical statistical analysis of small signals". In: *Physical Review D* 57.7 (Apr. 1998), pp. 3873–3889. DOI: 10.1103/physrevd.57.3873. URL: <https://doi.org/10.1103%2Fphysrevd.57.3873>.
- [2] Till Moritz Karbach. *Feldman-Cousins Confidence Levels - Toy MC Method*. 2011. arXiv: 1109.0714 [physics.data-an].
- [3] F. W. N. de Boer et al. "A deviation in internal pair conversion". In: *Phys. Lett. B* 388 (1996), pp. 235–240. DOI: 10.1016/S0370-2693(96)01311-1.
- [4] D.R. Tilley et al. "Energy levels of light nuclei A=8,9,10". In: *Nuclear Physics A* 745.3 (2004), pp. 155–362. ISSN: 0375-9474. DOI: <https://doi.org/10.1016/j.nuclphysa.2004.09.059>. URL: <https://www.sciencedirect.com/science/article/pii/S0375947404010267>.
- [5] A. J. Krasznahorkay et al. "Observation of Anomalous Internal Pair Creation in ${}^8\text{Be}$ ". In: *Acta Phys. Polon. Supp.* 8.3 (2015). Ed. by Marek Gozdz, p. 597. DOI: 10.5506/APhysPolBSupp.8.597.
- [6] Ulrich Ellwanger and Stefano Moretti. "Possible Explanation of the Electron Positron Anomaly at 17 MeV in ${}^8\text{Be}$ Transitions Through a Light Pseudoscalar". In: *JHEP* 11 (2016), p. 039. DOI: 10.1007/JHEP11(2016)039. arXiv: 1609.01669 [hep-ph].
- [7] Jonathan L. Feng et al. "Particle physics models for the 17 MeV anomaly in beryllium nuclear decays". In: *Phys. Rev. D* 95.3 (2017), p. 035017. DOI: 10.1103/PhysRevD.95.035017. arXiv: 1608.03591 [hep-ph].
- [8] Jonathan Kozaczuk. "Dark Photons from Nuclear Transitions". In: *Phys. Rev. D* 97.1 (2018), p. 015014. DOI: 10.1103/PhysRevD.97.015014. arXiv: 1708.06349 [hep-ph].
- [9] A. J. Krasznahorkay et al. "New experimental results for the 17 MeV particle created in ${}^8\text{Be}$ ". In: *EPJ Web Conf.* 137 (2017). Ed. by Y. Foka, N. Brambilla, and V. Kovalenko, p. 08010. DOI: 10.1051/epjconf/201713708010.
- [10] A. J. Krasznahorkay et al. "On the X(17) Light-particle Candidate Observed in Nuclear Transitions". In: *Acta Phys. Polon. B* 50.3 (2019), p. 675. DOI: 10.5506/APhysPolB.50.675.
- [11] Johannes Backens and Marc Vanderhaeghen. "X17 discovery potential in the $\gamma N \rightarrow e^+e^-N$ process at electron scattering facilities". In: (Oct. 2021). arXiv: 2110.06055 [hep-ph].

Appendix A

Fibers with G4TessellatedSolid

This appendix is to illustrate the core of the code necessary to create the fibers in GEANT4 for the muEDM simulations.

```
/*
 * Main function to create the helix.
 */
// Create a triangulated helix using G4TessellatedSolid
G4TessellatedSolid* HelixMaker::CreateHelix(G4String name, TVector3 center, double size, double runningangle, double length, int
    steps, double extrusion)
{
    // Create a new G4TessellatedSolid
    G4TessellatedSolid* helix = new G4TessellatedSolid(name);

    // Calculate number of turns
    double turns = AngleToTurns(runningangle, length, center.x());

    // Create base starting from 'center' and 'size'; triangulate it and add it to the helix
    std::vector<TVector3> base = CreateBase(center, size);
    // Tilt to match the running angle
    base = Tilt(base, center, runningangle);

    // If no extrusion just cap it, otherwise use the AddExtrusion function
    if(extrusion == 0) {
        std::vector<std::tuple<TVector3, TVector3, TVector3>> triang_base = TriangulateBase(base);
        MyADD(helix, triang_base);
    }
    else {
        std::vector<std::tuple<TVector3, TVector3, TVector3>> triang_base_extrusion = AddExtrusion(base, extrusion);
        MyADD(helix, triang_base_extrusion);
    }

    std::vector<TVector3> first=base;
    std::vector<TVector3> second;

    // Create the side: duplicate and move the base; triangulate the side; add to helix and repeat.
    for(int i=0; i<steps; i++){
        second=Transform(first, turns, steps, center, length);
        std::vector<std::tuple<TVector3, TVector3, TVector3>> triang_side = TriangulateSide(first,second);
        MyADD(helix, triang_side);
        first = second;
    }

    // The last vertex loop is used to cap the helix (NB it needs to be flipped)
    std::vector<TVector3> cap = first;
    cap = FlipLoop(cap);

    // If no extrusion just cap it, otherwise use the AddExtrusion function
    if(extrusion==0){
        std::vector<std::tuple<TVector3, TVector3, TVector3>> triang_cap = TriangulateBase(cap);
        MyADD(helix, triang_cap);
    }
    else{
        std::vector<std::tuple<TVector3, TVector3, TVector3>> triang_cap_extrusion = AddExtrusion(cap, extrusion);
        MyADD(helix, triang_cap_extrusion);
    }

    // Close the solid to ensure correct surface normals
    helix->SetSolidClosed(true);
}
```

```

    return helix;
}

/*
   Auxiliary functions to create the helix shape
*/

// From the angle to the number of turns
double HelixMaker::AngleToTurns(double angle, double length, double R){
    double turns = tan(angle)*length/(2*M_PI*R);
    return turns;
}

// Given the center and the size of the fiber creates a squared base
// Change this to move from *squared* helix to other shape.
std::vector<TVector3> HelixMaker::CreateBase(TVector3 center, double size){
    std::vector<TVector3> base = {
        center + TVector3(-size*0.5, -size*0.5, 0),
        center + TVector3(size*0.5, -size*0.5, 0),
        center + TVector3(size*0.5, size*0.5, 0),
        center + TVector3(-size*0.5, size*0.5, 0),};
    return base;
}

// Evaluate the path using the length t.
// Change this to move from *helix* to *other extrusion shapes*
TVector3 HelixMaker::Path(double t, double turns, TVector3 center, double length){
    double R = center.x();
    double x,y,z;
    x = R * cos(t/length* 2*M_PI *turns);
    y = R * sin(t/length* 2*M_PI *turns);
    z = t;
    TVector3 offset = TVector3(x,y,z);
    return offset;
}

// Function to flip the closing cap (to fix normals)
std::vector<TVector3> HelixMaker::FlipLoop(std::vector<TVector3> cap){
    std::vector<TVector3> fliploop;
    fliploop.push_back(cap[1]);
    fliploop.push_back(cap[0]);
    fliploop.push_back(cap[3]);
    fliploop.push_back(cap[2]);
    return fliploop;
}

// Function to create the triangulation for the endcaps
std::vector<std::tuple<TVector3, TVector3, TVector3>> HelixMaker::TriangulateBase(std::vector<TVector3> v){
    std::vector<std::tuple<TVector3, TVector3, TVector3>> faces;
    faces.push_back(std::make_tuple(v[3],v[1],v[0]));
    faces.push_back(std::make_tuple(v[3],v[2],v[1]));
    return faces;
}

// Function to create the triangulation given two vertices loops to be bridged
std::vector<std::tuple<TVector3, TVector3, TVector3>> HelixMaker::TriangulateSide(std::vector<TVector3> v, std::vector<TVector3> u){
    std::vector<std::tuple<TVector3, TVector3, TVector3>> faces;
    for(int i = 0; i<v.size()-1;i++){
        faces.push_back(std::make_tuple(v[i],v[i+1],u[i]));
        faces.push_back(std::make_tuple(v[i+1],u[i+1],u[i]));
    }
    // To close the loop
    faces.push_back(std::make_tuple(v[v.size()-1],v[0],u[v.size()-1]));
    faces.push_back(std::make_tuple(v[0],u[0],u[v.size()-1]));
    return faces;
}

// The square needs to be aligned to the angle of the fiber
std::vector<TVector3> HelixMaker::Tilt(std::vector<TVector3> v, TVector3 center, double angle){
    double x,y,z;
    std::vector<TVector3> u;

    for(int i = 0; i<v.size();i++){
        x = v[i].x();
        y = v[i].y()*cos(angle)+v[i].z()*sin(angle);
        z = -v[i].y()*sin(angle)+v[i].z()*cos(angle);

        u.push_back(TVector3(x,y,z));
    }
    return u;
}

// Function to add a triangulation to a G4TessellatedSolid.

```

```

void HelixMaker::MyADD(G4TessellatedSolid* helix , std :: vector<std :: tuple<TVector3 , TVector3 , TVector3>> triang){
    TVector3 a,b,c;
    for(auto i : triang){
        a = std :: get<0>(i);
        b = std :: get<1>(i);
        c = std :: get<2>(i);
        G4ThreeVector va(a.x(), a.y(), a.z());
        G4ThreeVector vb(b.x(), b.y(), b.z());
        G4ThreeVector vc(c.x(), c.y(), c.z());
        helix->AddFacet(new G4TriangularFacet(va, vb, vc, ABSOLUTE));
    }
}

// Given a lopp create a second loop along the path. These two are going to be bridged with triangulation
std :: vector<TVector3> HelixMaker::Transform(std :: vector<TVector3>v, double turns, int steps, TVector3 center, double length){
    std :: vector<TVector3> u;
    double angle_step = turns/steps*2*M_PI;
    double length_step = length/steps;
    for(int i = 0; i<v.size();i++){
        v[i].RotateZ(angle_step);
        u.push_back(v[i]+length_step*TVector3(0,0,1));
    }
    return u;
}

// Function to flip the closing cap (to fix normals)
std :: vector<std :: tuple<TVector3 , TVector3 , TVector3>> HelixMaker::AddExtrusion(std :: vector<TVector3> base, double extrusion){
    std :: vector<std :: tuple<TVector3 , TVector3 , TVector3>> faces;
    std :: vector<TVector3> extrusion_loop;
    TVector3 direction =((base[2]-base[0])).Cross(base[1]-base[0]);
    for(int i = 0; i<base.size();i++){
        extrusion_loop.push_back(base[i] + extrusion * direction.Unit());
    }

    std :: vector<std :: tuple<TVector3 , TVector3 , TVector3>> cap = TriangulateBase(extrusion_loop);

    base = FlipLoop(base);
    extrusion_loop = FlipLoop(extrusion_loop);
    faces = TriangulateSide(base, extrusion_loop);

    faces.insert(faces.end(), cap.begin(), cap.end());
    return faces;
}

```

Appendix B

Kalman filter

This Appendix is to illustrate the working principle of a Kalman filter, showing a simple linear problem in 2D. This is taken, with minor adjustments, from my Master Thesis: *In situ monitoring of the stopped muon flux at Mu2e*

B.1 The problem

Once the pattern recognition algorithms have been executed, a preliminary but rough estimate of the track parameters $\vec{\eta}$ is available. At this point, there are still numerous effects that should be accounted for when trying to optimize track reconstruction. Some of these effects are obvious, like, for example, the non-uniformity of the magnetic field, while others are less so. An example of the latter is the fact that a hit might have an intrinsic symmetry in a specific detector.

Mathematically, a track can be parameterized using a running variable and a vector of parameters. Quite often in particle physics, the particles move in magnetic fields, following a helicoidal trajectory. In this case the vector $\vec{\eta}$ with the helix parameters and the position along the beam axis z can be used: $F(\vec{\eta}; z)$. The fitting procedure then determines the best estimate of the vector $\vec{\eta}$ and the corresponding covariance matrix V . The task gets substantially more complicated if the parameters vector depends on the running variable $\vec{\eta}(z)$. This is the case when the traveling particle can lose energy, interact with some material along its path, or when the magnetic field is not uniform. These are common conditions and the effect in terms of variation of the track parameters values can be substantial. Fig. B.1 shows one possible simple example [1]. Now the procedure of finding the ‘optimal’ track parameters suddenly implies also that we need to define the position where we want to determine those parameters. It is often the case we are interested in determining the value of $\vec{\eta}$ at the target because this is where the physical process takes place.

B.2 The solution

The Kalman filter is a well-established algorithm in the standard formalism employed for track fitting developed to account for mechanisms like interactions with the detector material and magnetic field distortions that can affect the particle trajectory [2][3]. Most of today’s implementations are based on the BaBar filter and adaptations of [4][3]. In the typical track fitting procedure, the

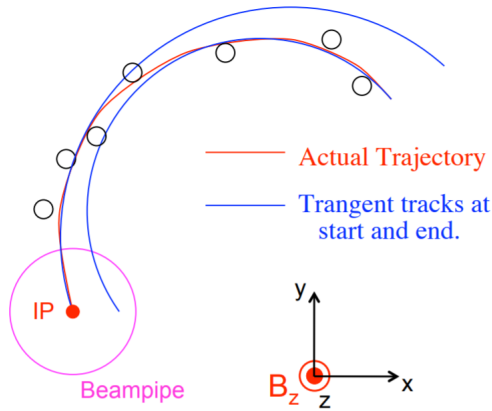


Fig. B.1: Pictorial view of the trajectory of a particle traveling along a circular path which has variable parameters [1]. The two blue circles represent the tangent circles at the beginning and at the end of the track segment: both circles are separately valid approximations of the particle trajectory in specific regions but they are not the best estimates of the entire trajectory.

pattern recognition algorithms employed to find a first estimate of the helix are followed by a simplified Kalman filter. This version does not account for all the effects yet, like the interaction with the detector material, but improves the accuracy of track parameters reconstruction. If more effects need to be accounted for, a second and more complete Kalman filter can be executed to introduce the missing residual effects. There are two important general aspects of this iterative algorithm we should briefly mention:

- With N points and n parameters the algorithm does not require to compute the inverse of $N \times N$ matrices¹ and simply uses multiplications of $n \times n$ matrices (easy to program and fast to run). If the problem is linearized the algorithm does not even require the inverse of the $n \times n$ matrix;
- Executing the algorithm in both directions of the trajectory once, storing the values of $\vec{\eta}$ and V after considering each point, allows us to determine the estimates with optimal uncertainties in any position.

The full implementation is extremely complicated and its thorough description is beyond the scope of this Thesis. Nonetheless, it is still useful to describe the basic principle through the discussion of a simplified problem, as a 2D linear fit. This will be done in Sec. B.4.

B.3 Implementation

The Kalman filter equations, linearized in η , are reported in Eq.B.1 with no proof, which is available in [5]. In these equations, η (dropping the vector symbol to avoid a too-heavy notation) and V are the current estimates of the vector and the covariance matrix, while the primed versions are the new estimates after a new hit is added. The measurement is indicated as d_m , with uncertainties σ , and $d(\eta)$ is the measurement as predicted by the track parameters. Finally, D_i represents the derivatives with respect to one of the track parameters. To iterate, the key feature to be noticed is that no matrix inversion of the order of $N \times N$ is needed in this calculation, which reduces the load

¹This is the case when introducing multiple scattering in a general fitting procedure: the position of a hit changes because of the interaction in another position creating a correlation between hits, summarized in a $N \times N$ matrix.

in terms of required computational resources.

$$\begin{aligned} D_i &= \frac{\partial d_m}{\partial \eta_i} \\ V' &= V - \frac{V D D^T V}{\sigma^2 + D^T V D} \\ \eta' &= \eta + V' D \frac{d_m - d(\eta)}{\sigma^2} \end{aligned} \quad (\text{B.1})$$

B.4 Example: a 2D linear fit

Track fitting and Kalman filtering are complex procedures and we have reported the description of the simpler 2D linear problem (Fig. B.2) in the following to better explain them. More detailed documentation is available in [1] [5]. In the following, we can assume to have a particle moving along a straight line and a number of tracking stations positioned at the relative distance L among them which measure the vertical coordinate. The tracking stations measure the y_i positions, all with the same uncertainty σ , and our goal is to estimate the parameters of the line at a point IP placed externally to the volume occupied by the detectors. The equation of the trajectory is reported in eq. B.2, the vector of parameters and the covariance matrix are reported in eq. B.3

$$y = mx + b \quad (\text{B.2})$$

$$\eta = \begin{bmatrix} m \\ b \end{bmatrix}, \quad V = \begin{bmatrix} V_{mm} & V_{mb} \\ V_{bm} & V_{bb} \end{bmatrix} \quad (\text{B.3})$$

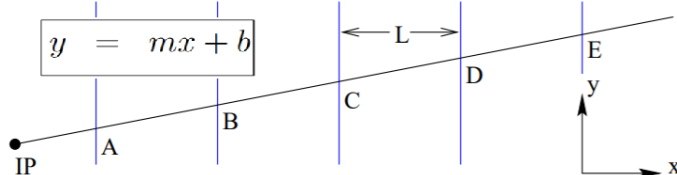


Fig. B.2: Pictorial view of a 2D trajectory of a particle moving along a straight line and interacting with a number of equally spaced tracking stations [1]. The stations measure the y positions and the goal is to determine the track parameters at some Initial Point (IP). The x origin is positioned on the last station while the y origin is not relevant for this exercise.

Initialization The first step is to provide a *seed* for the procedure. This is normally done with a pattern recognition algorithm which determines an initial estimate of the parameters, while V is assumed diagonal and with large values.

$$\eta = \begin{bmatrix} m_0 \\ b_0 \end{bmatrix}, \quad V = \begin{bmatrix} V_{mm,0} & 0 \\ 0 & V_{bb,0} \end{bmatrix}$$

First hit The procedure continues by adding point E and is simply necessary to apply the equations B.1, (the explicit calculation can be found in [1]):

$$V^{(1)} \approx \begin{bmatrix} V_{mm,0} & 0 \\ 0 & \sigma^2 \end{bmatrix}$$

$$\eta^{(1)} = \begin{bmatrix} m_0 \\ b_0 \end{bmatrix} + \begin{bmatrix} V_{mm,0} & 0 \\ 0 & \sigma^2 \end{bmatrix} \begin{bmatrix} 0 \\ 1 \end{bmatrix} \frac{y_E - b_0}{\sigma^2} = \begin{bmatrix} m_0 \\ y_E \end{bmatrix}$$

It is pretty straightforward to understand that employing just one hit provides information only on the track impact parameter, while there is no information on the trajectory slope.

Transport At this point the track is transported from E to D and, to do this, it is helpful to define a new coordinate system located on the second measurement plane. In this system the trajectory is $y' = m'x' + b'$ with $y = y'$, $x' = x + L$, $m' = m$ and $b' = b - mL$. By defining $A_{i,j} = \frac{\partial \eta'_i}{\partial \eta_j}$, the same track can be represented in a new base:

$$\eta^{(1')} = \begin{bmatrix} m_0 \\ y_E - m_0L \end{bmatrix}$$

$$V^{(1')} = AV^{(1)}A^T = \begin{bmatrix} V_{mm,0} & -LV_{mm,0} \\ -LV_{mm,0} & \sigma^2 + L^2V_{mm,0} \end{bmatrix}$$

As expected, the uncertainty on the slope remains unchanged by this transport, while the error on the impact parameter is now increased since the extrapolation used a slope with large uncertainty.

Second hit Since the track is now defined in the coordinate system of the second plane, adding the point D and applying again the Kalman equations B.1 is straightforward. The derivatives take the simple form: $D = \begin{bmatrix} 0 \\ 1 \end{bmatrix}$. we can skip the calculations and simply report the new estimators:

$$V^{(2)} \approx \begin{bmatrix} \frac{2\sigma^2}{L^2} & -\frac{\sigma^2}{L} \\ -\frac{\sigma^2}{L} & \sigma^2 \end{bmatrix}$$

$$\eta^{(2)} = \begin{bmatrix} m_0 \\ y_E - m_0L \end{bmatrix} + V^{(2)} \begin{bmatrix} 0 \\ 1 \end{bmatrix} \frac{y_D - (y_E - m_0L)}{\sigma^2} \approx \begin{bmatrix} \frac{y_E - y_D}{L} \\ y_D \end{bmatrix} \quad (\text{B.4})$$

The interesting feature is that all the assumed starting values have no impact on the estimates: m_0 , b_0 , $V_{mm,0}$ and $V_{bb,0}$. The uncertainty on the impact parameter is function of solely the local information (σ), while V_{mm} depends on both σ and L .

Transport and third hit In order to add a third measurement, the same two steps are needed: express the same track in the new base and then add the hit. The calculations are again detailed in [5] and we will only report the result:

$$V^{(3)} \approx \begin{bmatrix} \frac{\sigma^2}{2L^2} & -\frac{\sigma^2}{2L} \\ -\frac{\sigma^2}{2L} & \frac{5}{6}\sigma^2 \end{bmatrix}$$

$$\eta^{(3)} \approx \begin{bmatrix} \frac{y_E - y_C}{2L} \\ \frac{2y_D - y_E + 5y_C}{6} \end{bmatrix}$$

It is interesting to notice that once the third point has been added, the diagonal elements of the covariance matrix are reduced with respect to the case with only two points.

Finishing Once the procedure has been iterated to reach point A, the estimators of the trajectory use all the available information and are valid in a neighborhood region of A. To extrapolate to the track IP, the procedure is the same as before, describing the trajectory in the coordinate system set in the IP.

B.4.1 Adding multiple scattering

How does the problem of track fitting change if the detectors are not ideal planes but consist of a thin scattering volume? The initialization and the inclusion of the first hit do not change. The uncertainty due to multiple scattering on the first hit is negligible because of the starting covariance matrix. In this simple model, the scattering is *local* and contributes only to the slope error and not the off-diagonal terms and the intercept, but as the track is extrapolated away from the surface it contributes to these terms as well.

If the surface introduces a factor δ in the error of the slope, the matrix in eq B.4 the vector remains the same while the matrix becomes

$$V^{(2)} \approx \begin{bmatrix} \frac{2\sigma^2}{L^2} + \delta^2 & -\frac{\sigma^2}{L} \\ -\frac{\sigma^2}{L} & \sigma^2 \end{bmatrix}$$

From this point on the presence of δ can change substantially the results because at the next iteration, it will enter in both V' and η' . In [5] the calculations are extensively developed up to the third point (point C) with the specific example $\delta^2 L^2 = \sigma^2$ to keep the passages easy to follow.

Bibliography on Kalman filter

- [1] Robert K. Kutschke. "Kalman Filters: As Told by a Physicist to Physicists". In: *Mu2e-doc-557-v2* (June 2009).
- [2] Pierre Billoir. "Track fitting with multiple scattering: A new method". In: *Nuclear Instruments and Methods in Physics Research* 225.2 (1984), pp. 352–366. ISSN: 0167-5087. DOI: [https://doi.org/10.1016/0167-5087\(84\)90274-6](https://doi.org/10.1016/0167-5087(84)90274-6). URL: <http://www.sciencedirect.com/science/article/pii/0167508784902746>.
- [3] R. Fruhwirth. "Application of Kalman filtering to track and vertex fitting". In: *Nucl. Instrum. Meth. A* 262 (1987), pp. 444–450. DOI: 10.1016/0168-9002(87)90887-4.
- [4] D. N. Brown , E. A. Charles , D. A. Roberts. "The BaBar Track Fitting Algorithm". In: () .
- [5] Robert K. Kutschke. "Example of a Kalman filter n a straight line". In: (Mar. 1998). URL: %7Bhttps://home.fnal.gov/~kutschke/Tracking/kalman_simple.pdf%7D.

Acknowledgements

There have been three types of relations helping me reaching this point in my life: relatives have been a steady pillar from which I could reach out to the unknown; mentors showed me a path, leaving me the leisure of choosing to take it; friends shared with me tears and laughter along the road. None of you reading these few lines has been fixed in one of these roles and I am grateful *to you* from the bottom of my heart. I do not wish to make this page a list of names. You know your own name and I look forward to thank you in person. I feel nonetheless compelled to thank here the one I am no longer able to meet: Nonni Carlo e Vittorio, Zio Papele.

Bastiano Vitali, Rome, xx/xx/202x

